

## ABSTRACT

### The Effect of Defects and Imperfections on the Structural Integrity of Adhesively Bonded Laminated Composites

Akash P. Pisharody, Ph.D.

Mentor: Douglas E. Smith, Ph.D.

The increased demand for long range, fuel efficient and high performance, high fuel economy automobiles has resulted in the growth of use of composites in aerospace and automotive sectors . Adhesive bonding is the preferred method to join composites as it does not require extra machining such as drilling of holes and avoids stress concentrations. As in other manufacturing processes, defects and imperfections may occur in bonded joints which can reduce the load carrying capacity of the joint. Non-destructive test methods such as ultrasonic scanning is used to determine the shape, size and position of defects and imperfections, and the reduction in strength due to defects has been predicted using both analytical and numerical methods. Previous studies on defects have primarily focused on defects within the adhesive bond such as voids and inclusions. Other bond imperfections such as improper adhesive distribution and thickness variations, occur in the bonded joints as well, which often result from improper fabrication techniques. The aim of the current study is to determine the effect of selected defects and imperfections on bonded joint integrity, which have not been previously

addressed, and develop a suitable methodology for analyzing the strength of single lap bonded joints that have been compromised by the defects and imperfections. The primary focus here is to understand the effects of adhesive joint imperfections such as improper adhesive distribution and bond line thickness variations, and adherent defects in the form of inclusions, on the strength of adhesive bonded unidirectional carbon fiber reinforced polymer composite joints. Results show that a linear variation in bond line thickness decreases the failure strength of single lap bonded joints when compared with joints of uniform bond line thickness. The investigation with improper adhesive distribution across the overlap shows that the failure strength of bonded joints depends on the shape and size of the adhesive distribution. For the bonded joints with inter-ply inclusion defects, the location of the defect and the ply orientation of the adherend influences the failure strength of bonded joints. The study on the effect of increase in bond line thickness of single strap joints reveals a decrease in bond strength with an increase in bond line thickness. The failure strengths of bonded joints with uniform and varying bond line thickness along with that of single strap joints with uniform bond line thickness is predicted using the Critical Zone method. An insight into the change in stress states due to the presence of imperfections and defects studied, is established.

The Effect of Defects and Imperfections on the Structural Integrity of Adhesively Bonded  
Laminated Composites

by

Akash P. Pisharody, B.Tech, M.Tech

A Dissertation

Approved by the Department of Mechanical Engineering

---

Paul I. Ro, Ph.D., Chairperson

Submitted to the Graduate Faculty of  
Baylor University in Partial Fulfillment of the  
Requirements for the Degree  
of  
Doctor of Philosophy

Approved by the Enter Dissertation or Thesis Committee

---

Douglas E. Smith, Ph.D., Chairperson

---

David A. Jack, Ph.D.

---

Abhendra Singh, Ph.D.

---

Trevor Fleck, PhD

---

Steve Bradley, PhD

Accepted by the Graduate School

May 2021

---

J. Larry Lyon, Ph.D., Dean

Copyright © 2021 by Akash P. Pisharody

All rights reserved

## TABLE OF CONTENTS

LIST OF FIGURES .....	vii
LIST OF TABLES .....	xiv
ACKNOWLEDGMENTS .....	xvi
DEDICATION .....	xvii
CHAPTER ONE .....	1
Introduction.....	1
1.1 Research Background and Motivation.....	1
1.2 Order of Dissertation.....	5
CHAPTER TWO .....	8
Literature Review .....	8
2.1 Mechanical Testing .....	8
2.3 Parameters Affecting Strength of Bonded Joints.....	10
2.2 Defects and Imperfections .....	14
2.3 Strength Prediction Techniques .....	18
CHAPTER THREE .....	33
Methodology.....	33
3.1 Experimental Work.....	33
3.2 Numerical Modeling.....	45
CHAPTER FOUR.....	52
Effect of Adhesive Thickness Variations .....	52
4.1 Study on a Constant Bond Line Thickness .....	54
4.2 Study on Linearly Varying Bond Line Thickness Due to Adherend Misalignment .....	64
CHAPTER FIVE .....	76
Effect of Adhesive Distribution.....	76
5.1 Incomplete Adhesive Coverage: Woven Composites.....	77
5.2 Incomplete Adhesive Coverage: Unidirectional Composites .....	85
CHAPTER SIX.....	101
Effect of Adherend Inclusions and Ply Orientations .....	101
6.1 Adherend Inclusions in a Unidirectional Composite .....	102
6.2 Study on the Effect of Adherend Inclusions with Various Ply Orientations ....	112

CHAPTER SEVEN .....	131
Effect of Adhesive Thickness Variations in Strap Joints .....	131
7.1 Study on Constant Bond Line Thickness .....	131
7.2 Study on Variable Bond Line Thickness .....	140
CHAPTER EIGHT .....	147
Conclusions and Future Work .....	147
8.1 Conclusions .....	147
8.2 Future Scope .....	154
APPENDIX A .....	157
Characterization of Carbon Fiber Adherends and Adhesive .....	157
APPENDIX B .....	163
ABAQUS UMAT FORTRAN Code for Strength Prediction Using Critical Zone Method .....	163
APPENDIX C .....	167
Three-dimensional Adaptation of the Generalized Form of Hoffman`s Criterion for Strength Prediction .....	167
BIBLIOGRAPHY .....	169

## LIST OF FIGURES

Figure 1.1. Various adhesive joint configurations .....	2
Figure 1.2. Common defects in adhesive bonded joints .....	3
Figure 2.1. Deformation and stress states in a Single Lap Joint .....	8
Figure 2.2. Various modes of failure .....	9
Figure 2.3. Schematic of a) Double cantilever beam test b) End Notched Flexural test .....	10
Figure 2.4. Critical distance and critical longitudinal strain for measuring failure load using critical longitudinal strain method.....	22
Figure 2.5. Regions of stress concentration in a Single lap joint.....	23
Figure 2.6. Damage zone in a composite adherend .....	24
Figure 2.7. Schematic of the single lap bonded joint with the coordinate axes.....	25
Figure 2.8. Finite Fracture mechanics principle .....	27
Figure 2.9. Traction-separation law for Cohesive Zone modeling .....	29
Figure 2.10. a) Cohesive elements in a local approach and b) Continuum approach.....	29
Figure 3.1. Layout of wet layup process for fabrication of carbon fiber adherends.....	34
Figure 3.2. Single lap joint test coupon fabrication fixture .....	35
Figure 3.3. Measurement of bond line thickness from cross-section of a single lap joint using Keyence microscope. ....	36
Figure 3.4. Dimensions of tensile test bars for 0° and 90° orientations .....	37
Figure 3.5. a) Test setup for characterization of carbon fiber adherends b) Strain gauges mounted on carbon fiber test samples.....	38
Figure 3.6. Geometry of Compressive test specimen .....	40
Figure 3.7. a) Test setup for compression testing b) Compression test fixture mounted on platens attached to the universal testing machine .....	41

Figure 3.8. a) Test setup for short beam test. b) Short beam test fixture .....	42
Figure 3.9. Mold used for casting adhesive tensile test bars. ....	44
Figure 3.10. a) Test setup for characterization of Hysol 9309 NA adhesive. b) Cured test bars .....	45
Figure 3.11. Simulation model dimensions for single lap joint with boundary conditions.....	46
Figure 3.12. Mesh details for a 2D single lap joint model.....	47
Figure 3.13. Schematic of load and boundary conditions and path for stress analysis.....	48
Figure 3.14. Comparison of Von-Mises stress for various mesh sizes for a 2D model....	48
Figure 3.15. Comparison of Von-Mises stress for various mesh sizes for a 3D model....	49
Figure 3.16. Geometry of test specimen used for FE model verification. ....	50
Figure 3.17. Comparison of Load-displacement curves obtained experimentally and using FE analysis.....	51
Figure 4.1 a) A fuselage of a typical large aircraft composed of joined sections. b) Magnified view of one of the joined sections (A) with and without misalignment.....	53
Figure 4.2. Bond line thickness measurement using a Keyence microscope. ....	54
Figure 4.3. Failed surface of a bond with uniform thickness.....	55
Figure 4.4. Failure loads for various bond line thickness. ....	56
Figure 4.5. a) Contour plot of the solution dependent variable corresponding to Hoffman`s criteria b) Volume of critical zone measured in ABAQUS CAE.....	57
Figure 4.6. Reaction force as a function of displacement plotted in ABAQUS CAE for a bond line thickness of 0.25 mm.....	58
Figure 4.7. Mesh details of the single lap joint model used for stress analysis.....	61
Figure 4.8. Path prescribed along the mid-thickness of the first ply for stress measurements.....	61
Figure 4.9. a) Peel stress distribution along middle of first ply closest to the bond line.....	62
Figure 4.10. a) Shear stress distribution along middle of first ply closest to the bond line.....	62

Figure 4.11. Comparison of maximum shear and peel stress for different bond line thickness.....	63
Figure 4.12. Bond line thickness measurement using a Keyence microscope. ....	64
Figure 4.13. Dimensions of single lap joint with varying bond line thickness.....	66
Figure 4.14. Plots of failure load v/s difference between the lower and maximum thickness of a single lap joint having varying bond line thickness with a nominal initial thickness of a) 0.33 mm b) 0.37 mm c) 0.42 mm and d) 0.47 mm. ....	68
Figure 4.15. Mesh details for a joint with varying bond line thickness.....	69
Figure 4.16. Boundary conditions and path for stress analysis for a joint with linear variation in thickness .....	71
Figure 4.17. a) Plot of peel stress distribution along the middle of first ply closest to the bond line for a joint having average minimum thickness of 0.33mm with various thickness variations b) Magnified view of detail ‘A’ .....	72
Figure 4.18. a) Plot of shear stress distribution along the middle of first ply closest to the bond line for a joint having a minimum thickness of 0.33mm with various thickness variations b) Magnified view of detail ‘A’.....	72
Figure 4.19. Comparison of maximum values of shear and peel stresses for joints with minimum thickness of 0.33 mm and increasing difference between minimum and maximum thickness. ....	73
Figure 5.1. a) Adhesive applied along a straight-line b) shape attained after pressure application using the second adherend (Major axis: 25 mm, Minor axis: 21 mm).....	77
Figure 5.2. PTFE cutouts for fabricating the required adhesive shapes. ....	79
Figure 5.3. Custom immersion scan system .....	80
Figure 5.4. Ultrasonic scan path and direction .....	80
Figure 5.5. a) Failed surface as observed in joints having complete adhesive coverage. b) Magnified image of failed adhesive surface from the region highlighted in a, showing adherent failure.....	81
Figure 5.6. a) A-scan at X = 2 mm, Y = 2 mm, and b) B-Scan at X = 2 mm of an un-bonded Carbon fiber laminate plate.....	83
Figure 5.7. Comparison of A-scans at overlap region of the adhesive overlap in the a) PTFE film region and the b) Adhesive region.....	84

Figure 5.8. B-Scans along a) $X = 2$ mm and 2) $X = 12$ mm.....	84
Figure 5.9. C-Scan images at the bond line and comparison with their corresponding broken surfaces of the configurations a) C1, b) E2-2 (The Black outlines on the left images are the adhesive outlines traced from the optical images on the right.).....	85
Figure 5.10. 3D model used for FE analysis.....	87
Figure 5.11. Mesh assembly details for a circular shaped adhesive (C2 configuration).....	88
Figure 5.12. Paths used to extract stress values.....	89
Figure 5.13. Von Mises stress for a) E2-1 and b) E1-1 configurations .....	90
Figure 5.14. Comparison of a) Peel stress and b) Shear stress along the middle of first ply for elliptical adhesive shape of orientation 1 .....	91
Figure 5.15. Comparison of a) Peel stress and b) Shear stress along the middle of first ply for elliptical adhesive shape of orientation 2 .....	91
Figure 5.16. Comparison of a) Peel stress and b) Shear stress along the middle of first ply for circular adhesive shape.....	92
Figure 5.17. Comparison of a) Peel stress and b) Shear stress for elliptical orientations E1-3 and E2-3 .....	93
Figure 5.18. Comparison of a) Peel stress and b) Shear stress for elliptical orientations E1-2 and E2-2 .....	93
Figure 5.19. Comparison of a) Peel stress and b) Shear stress for elliptical orientations E1-1 and E2-1 .....	94
Figure 5.20. Experimental and 3D FE prediction of failure loads for various bond line thickness with complete coverage of adhesive using Hoffman`s criteria.....	96
Figure 5.21. a) Contour showing distribution of solution variable and b) 3D view of the reference volume (Section A) used for calculating the failure loads using the Critical Zone method applying Hoffman`s criterion.....	97
Figure 5.22. Comparison of Von-Mises stresses at the center of the bond line for various configurations.....	98
Figure 6.1. Regions of stress concertation in a Single lap joint.....	101
Figure 6.2. Insertion of PTFE strips to simulate inclusion defect during wet laying process between the first and the second layer of the laminate composite.....	103

Figure 6.3. Location of PTFE inclusion in the joint assembly along with the position of the coordinate axes used for measurement of inclusion position. ....	103
Figure 6.4. Image showing the failed surface exhibiting light fiber tear failure, for a non-defective joint. ....	104
Figure 6.5. Mesh details of the model used for stress analysis. ....	106
Figure 6.6. Schematic of Finite Element model .....	106
Figure 6.7. Path through middle of the first ply used to plot the stresses in the FE model. ....	107
Figure 6.8. a) Peel stress distributions in the middle of first ply for various configurations b) magnified view of detail A .....	107
Figure 6.9. a) Shear stress distributions in the middle of first ply for various configurations b) magnified view of detail A .....	108
Figure 6.10. Vertical displacements of the first ply for various configurations .....	109
Figure 6.11. Vertical displacement ( $U_y$ ) contours for a) Defect position $x = -6.35$ b) Non-defective joint .....	109
Figure 6.12. Comparison of shear stresses for various widths of inclusion at a position of the inclusion at $x = 0$ .....	110
Figure 6.13. a) Schematic diagram showing stacking sequence in the adherend with layup along the out of plane Z axis b) Location of PTFE inclusion in the joint assembly .....	113
Figure 6.14. Ply position in a laminated composite.....	114
Figure 6.15. Failed surfaces for various layup configurations with and without defects. ....	120
Figure 6.16. FE model used for stress analysis.....	121
Figure 6.17. Paths used to plot the stresses in the FE model. ....	122
Figure 6.18. a) Shear stress distributions along the middle of the first ply adjacent to the bond line for the non-defective configurations b) magnified view of detail A .....	123
Figure 6.19. a) Peel stress distributions along the middle of the first ply adjacent to the bond line for the non-defective configurations b) magnified view of detail A .....	123

Figure 6.20. a) Shear stress distributions along the middle of the first ply adjacent to the bond line for the configurations with inclusion defect b) magnified view of detail A .....	124
Figure 6.21. a) Peel stress distributions along the middle of the first ply adjacent to the bond line for the configurations with inclusion defect b) magnified view of detail A .....	125
Figure 6.22. a) Peel and b) Shear stress comparison for $[0/90]_3$ adherend stacking.....	125
Figure 6.23. a) Peel and b) Shear stress comparison for $[45/0/-45]_s$ adherend stacking.....	126
Figure 6.24. a) Peel and b) Shear stress comparison for $[45/90/0]_s$ adherend stacking.....	126
Figure 6.25. a) Peel and b) Shear stress comparison for $[90/45/0]_s$ adherend stacking.....	127
Figure 6.26. a) Peel and b) Shear stress distributions at the center of the bond line across the overlap length for defective joints .....	128
Figure 7.1. Schematic of a single strap joint used for the study. ....	132
Figure 7.2. Fabrication of single strap joint in the fabrication fixture .....	132
Figure 7.3. Bond line thickness measurement using a Keyence microscope. ....	133
Figure 7.4. Experimental and FE predictions of failure loads for a single strap joint with varying constant thickness.....	134
Figure 7.5. Failed surface of a single strap joint.....	134
Figure 7.6. Mesh details of a single strap joint model .....	135
Figure 7.7. Peel stress contour in the bonded region .....	135
Figure 7.8. Shear stress contour in the bonded region.....	136
Figure 7.9. Path defined in the model for plotting of shear and peel stress.....	136
Figure 7.10. a) Peel stress distribution along middle of first ply closest to the bond line.....	137
Figure 7.11. a) Shear stress distribution along middle of first ply closest to the bond line.....	137

Figure 7.12. Schematic of a single strap joint with varying bond line thickness .....	140
Figure 7.13. Cross-sectional image of single strap joint with varying bond line thickness.....	141
Figure 7.14. Mesh details for the study of varying bond line thickness in strap joints.....	143
Figure 7.15. Path defined in the model for plotting of shear and peel stress.....	144
Figure 7.16. a) Shear stress distribution along middle of first ply closest to the bond line.....	144
Figure 7.17. a) Peel stress distribution along middle of first ply closest to the bond line.....	145
Figure A.1. Stress-strain curves of unidirectional carbon fiber adherends of 0° orientation.....	159
Figure A.2. Stress-strain curves of unidirectional carbon fiber adherends of 90° orientation .....	159
Figure A.3. Stress-strain curves of Hysol 9309 NA adhesive .....	162
Figure C.1. Coordinate system on a 3D plate. ....	167

## LIST OF TABLES

Table 3.1. Measured Elastic properties of carbon fiber adherends.....	43
Table 3.2. Measured strengths of carbon fiber adherends. ....	43
Table 3.3. Measured stiffness and strength of Hysol 9309 NA adhesive .....	45
Table 4. 1. Experimental plan for studying thickness variations.....	55
Table 4.2. Volume of critical zone using various failure criteria. ....	58
Table 4.3. Comparison of predicted failure loads with experimental trend curve fit (Equation 4.1) .....	60
Table 4.4. Experimental plan for study of varying thickness .....	65
Table 4.5. Experimentally recorded thickness and failure load.....	66
Table 4.6. Comparison of experimental and FE predicted failure loads for joints with varying minimum thickness.....	70
Table 5. 1. Experimental plan for study of effect of incomplete adhesive coverage in single lap joints. (Specimen identifiers are shown in brackets), (All dimensions in mm) .....	78
Table 5. 2 Comparison of failure loads across various configurations.....	81
Table 5.3. Comparison of failure loads across various configurations.....	86
Table 6.1. Experimental Plan and results (Position w.r.t origin as shown in Figure 6.3).....	104
Table 6.2. Experimental and Finite element failure load comparison .....	111
Table 6.3. Comparison of experimental failure load and bending stiffness. ....	115
Table 6.4. Percentage increase in shear and peel stress with different adherend stacking sequences due to presence of inclusion defect.....	127
Table 7.1. Comparison of stresses and failure loads.....	138
Table 7.2. Comparison of failure strength of Single lap and Single strap joints .....	138
Table 7.3. Reference values of volumes used for strength prediction. ....	139

Table 7.4. Measured bond line thickness and failure loads for various specimens. ....	142
Table 7.5. FE predicted values for failure load for bond line thickness variations. ....	143
Table A.1. Tensile test results of unidirectional carbon fiber adherends of 0° orientation .....	158
Table A.2 Tensile test results of unidirectional carbon fiber adherends of 90° orientation .....	158
Table A.3. Compression test results of unidirectional carbon fiber adherends of 0° orientation .....	160
Table A.4. Compression test results of unidirectional carbon fiber adherends of 90° orientation .....	160
Table A.5. Short beam test results .....	161
Table A.6. Tensile test results of Hysol 9309 NA adhesive .....	161

## ACKNOWLEDGMENTS

I would like to thank Dr. Douglas E. Smith for his continued support and guidance. I would also like to thank Dr. David. A. Jack for his support and motivation. I would like to thank Dr. Abhendra Singh for his support in materials testing. I would also like to thank Mr. Timothy Russel, Dr. Ben Blandford and Mr. Nate Blackman for their support and help in experimentation and ultrasonic scanning. I would like to thank L3 Harris Technologies for sponsoring and supporting my research work. I would like to thank the committee for their feedbacks which helped me improve my dissertation work. Lastly, I would like to thank my wife for her support, motivation and love which helped me complete my work despite us being far apart for a long time. I would also like to thank my parents and parents in law for their support and motivation.

## DEDICATION

*To my lovely wife who is the light of my life.*

## CHAPTER ONE

### Introduction

#### *1.1 Research Background and Motivation*

Composite materials offer advantages over other methods of joining like riveting or bolting, such as weight reduction and corrosion reduction [1]. The use of composite materials have been increasing in the aerospace sector with the new models of aircraft such as the Boeing 787 and the Airbus A350 consisting of almost 52% of Carbon Fiber Reinforced Polymer (CFRP) by weight [2]. Implementation of CFRP in aerospace has led to reduction in weight and part counts translating to higher fuel efficiencies and longer ranges of commercial aircraft [3]. A similar trend is being observed in the automotive sectors especially with the introduction of electric vehicles and the need of reducing fuel consumption in conventional gas powered vehicles [3]. Adhesive bonding is a cost effective and light weight alternative to join composite materials [4]. Conventional joining methods such as bolting and riveting require drilling of holes in the substrates to be joined. Drilling holes causes stress concentrations and the possibility of delamination in CFRP substrates, which can be eliminated by joining CFRP substrates using adhesive bonding [4].

Adhesive bonding involves joining metallic, polymer or composite adherends using an epoxy based, acrylic or polyurethane based adhesive. The adherends can be bonded in various configurations as shown in Figure 1.1. Single lap joints are commonly used for testing and characterization of adhesives since it is simple and efficient. Single

lap joints also produce a mixed loading condition in the joint [5] which help characterize the shear and peel behavior of the adhesives in a single test. The mixed behavior can be attributed to the eccentric load path which produces a bending moment at the ends of the single lap joint [6]. Peel stresses can be minimized by adopting a double lap, scarf, or butt joint configuration. While using Fiber Reinforced Polymer (FRP) Composites as adherends, the choice of joint configuration is of importance since FRP composites have lower strengths in the out of plane direction [1]. The failure mechanism becomes complicated due to this reduction in strength in bonded joints having FRP composite adherends [7].

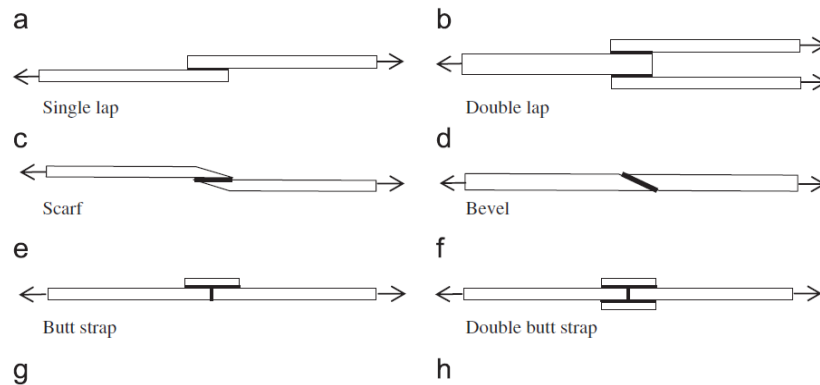


Figure 1.1. Various adhesive joint configurations [8]

A “flaw” or “imperfection” can be defined as any deviation from the ideal. [9]. In terms of adhesive bonded joints, an imperfection would mean a deviation from the point of design, for instance, variations in thickness of the adherend or the adhesive, improper distribution of the adhesive and inaccurate overlap lengths. Imperfections would not necessarily lead to a rejection of the during inspection [9]. Defects on the other hand can be considered more critical. Defects could result in a reduction in bond strength by

reducing the overall capacity of the joint to carry loads, hence causing a premature failure [10]. The possibility of rejection depends on the nature and extent of the defect, applied load and joint configuration [11]. Common defects in bonded joints include voids, inclusions, lack of adhesion (kissing bonds) and cracks [12], and are illustrated in Figure 1.2. Defects can be broadly classified into three types namely, gross, cohesive and adhesive defects [13]. Cracks, voids and porosities fall under gross defects, which can be detected using non-destructive techniques such as ultrasonic scanning [13]. Cohesive defects are those which are produced due to insufficient cure of the adhesive [14]. These can be detected using ultrasonic methods by measuring the difference in the velocity of sound through the adhesive [15] or by analyzing holographic interferometry patterns [16].

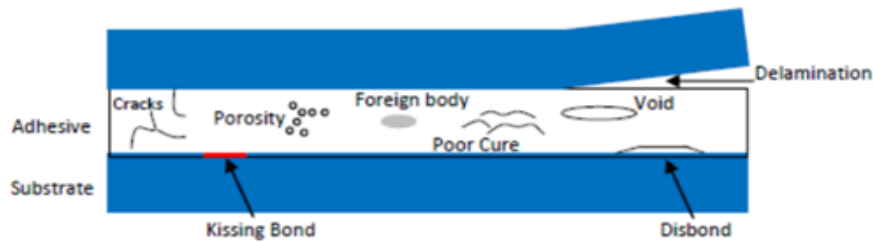


Figure 1.2. Common defects in adhesive bonded joints [14]

Recent advancements in non-destructive testing has made it possible to detect defects including their shape and size [17,18] . Blackman, et al. [19] were able to detect inclusions (foreign objects) as small as 1.9 mm in CFRP composites. Bond-line thickness variations also play an important role in determining the strength of bonded joints. An increase in bond line thickness results in a decrease in the strength of bonded joints. The exact nature of variation of bond strength depends on the nature of the adhesive. In case of brittle adhesives a decrease in bond strength is observed with increase in bond type

thickness [20]. For ductile adhesives the bond strength increases initially, till it reaches an optimum thickness and then decreases further [21].

A review of the current literature reveals gaps in the study of bond line imperfections such as incomplete distribution of adhesives across the bond interface, variation of bond line thickness and defects like inclusions in the adherend, on the strength of bonded joints. Incomplete distribution of adhesives and bond line thickness variations may be caused by improper fixturing of the parts being bonded. Variations in bond line thickness can cause an increase in the stresses at the lower thickness end of the lap joints, which may cause a change in failure loads [22]. Inclusion may cause delamination if they occur between the plies of the laminated composite material, which would lead to a degradation of material stiffness and strength [23]. In single lap joints, higher stresses are generated at the ends of the overlap, near the bond line, in both the adhesive and the adherend [24]. Delamination in the region close to the bond line can cause a spike in the stresses leading to a deterioration of bond strength, when laminated composite adherends are used. With the aid of non-destructive methods like ultrasonic testing and use of finite element analysis, it would be possible to detect these imperfections and defects and assess their effect on strength of bonded joints. Early detection of such flaws and imperfections can help prevent catastrophic failures and unnecessary repairs as well as down-times.

The objective of the current research work is to establish a basic understanding of the effects of imperfections and defects on adhesive bonded joints, specifically considering incomplete coverage of adhesive, bond-line thickness variations and

inclusions in the adherend. The tasks for realizing this objective employs a single lap joint as the test vehicle and includes:

1. Determination of bond joint degradation due to adhesive imperfections such as bond line thickness variations and incomplete adhesive distributions.
2. Determination of the effect of underlying polymer composite inclusion defects in the adherend, on joint integrity.
3. Modeling and Simulation of Bond Joint Structural Integrity and investigating the applicability of the critical zone method to predict the failure strength for the various bond line imperfections and defects.
4. Demonstration of applicability of the critical zone method on a single strap bond joint, which is sufficiently different than the single lap joint, to predict failure.

### *1.2 Order of Dissertation*

The dissertation has been split into eight chapters. The literature review has been covered in Chapter Two, including the current state of art on studies in materials testing, defects and imperfections in bonded joints and strength prediction techniques of bonded joints, including finite element methods. Chapter Three discusses the methodology of performing the experiments including the materials characterization and finite element analysis. Chapter Four covers the investigations of bond line thickness variations on the failure strength of unidirectional composite bonded joints. The first part of the study investigates the effect of increasing the uniform bond line thickness on the strength and the subsequent part covers the study of linearly varying bond line thickness on the strength of bonded joints. Failure prediction is performed using the Critical Zone method

and stress analysis is performed to quantify the changes in stresses due to thickness variations. Chapter Five covers the study of incomplete distribution of the adhesive across the bond overlap, on the strength of bonded joints. Both woven and unidirectional fiber composite laminates are used for this study. The first part of this study with woven composites, published in the “Applied Adhesion Science” journal, covers the experimental testing and ultrasonic detection of incomplete adhesive distribution with woven fabric composite adherends. The second part of this chapter investigates the effect of incomplete adhesive distribution on the strength of bonded joints with unidirectional fiber composite adherends. A finite element stress analysis is also performed to investigate the changes in the stress states due to incomplete adhesive distribution.

Chapter Six discusses the study on the effect of inter-layer inclusions, embedded between the first and second ply of one of the adherends adjacent to the bond line. The first part of the study investigates the effect of position of the inclusion in unidirectional laminated composite adherend. The second part investigates the inclusion defect placed at the location corresponding to the greatest reduction in strength, observed from the studies on unidirectional composites observed in the first part, and its effect on bond strength of bonded joints having adherends with various ply orientations. A Finite Element analysis reveals the change in stress states due to the presence of the inclusions and change in ply orientations in the adherend. Chapter Seven discusses the effect of bond line thickness variations in single strap joints. The first part investigates the effect of variation in bond line thickness in uniform bond line joints. Failure prediction and stress analysis are performed. The second part discusses the effect of linear variation in bond line thickness on the strength of single strap bonded joints. Finite Element analysis is also performed

for strength predications and stress analysis. Chapter Eight summarizes the results and presents the conclusions of the studies presented in this dissertation and lists the future scopes of work.

## CHAPTER TWO

### Literature Review

#### *2.1 Mechanical Testing*

Material testing of the adherends and adhesive is important to determine the constitutive mechanical properties, which in turn are required for finite element analysis of bonded joints. One of the basic characterization tests performed on adhesives is the lap shear test. ASTM D1002 [25] prescribes the methodology for characterizing adhesives using a single lap joint. The single lap joint is one of the simplest test configurations, which can be easily fabricated and tested on a conventional tensile testing machine. The joint captures both shear and peel stresses as shown in Figure 2.1 which makes it an excellent test vehicle for characterizing adhesives.

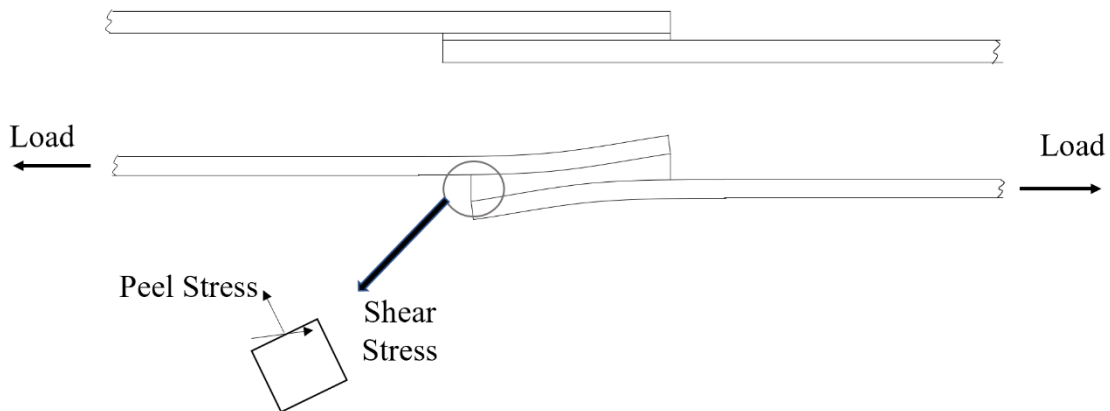


Figure 2.1. Deformation and stress states in a Single Lap Joint

Mechanical characterization of adherends and adhesives is required for extracting the material stiffness and strength parameters. Metallic adherends can be characterized by the standards such as ASTM E8 [26] while composites are characterized in accordance with ASTM D3039 for tensile properties. SRM IR-94 [27] and ASTM D2344 [28] provide guidelines for compression and inter-laminar shear strengths of composites.

Fracture characterization of adhesives and laminated adherends are performed using Double Cantilever Beam (DCB) test and End Notched Flexural (ENF) test. These tests measure the fracture energies in mode I and mode II, respectively. The various fracture modes seen in materials are shown in Figure 2.2. Mode I is a pure tensile mode while Mode II is a pure shear mode of loading. The DCB and ENF tests measure the critical fracture energies ( $G_c$ ). Failure in form of crack initiation begins when fracture energy  $G$  equals or exceeds a critical value ( $G_c$ ) [29]. Depending on the mode of loading, fracture energy can have three modes namely  $G_{1c}$ ,  $G_{2c}$  and  $G_{3c}$  each for mode 1, 2 and mixed mode of loading. The DCB and ENF tests as shown in Figure 2.3 generate the parameters for the traction separation law which can be used to predict failure using methods such as Cohesive Zone Modeling.

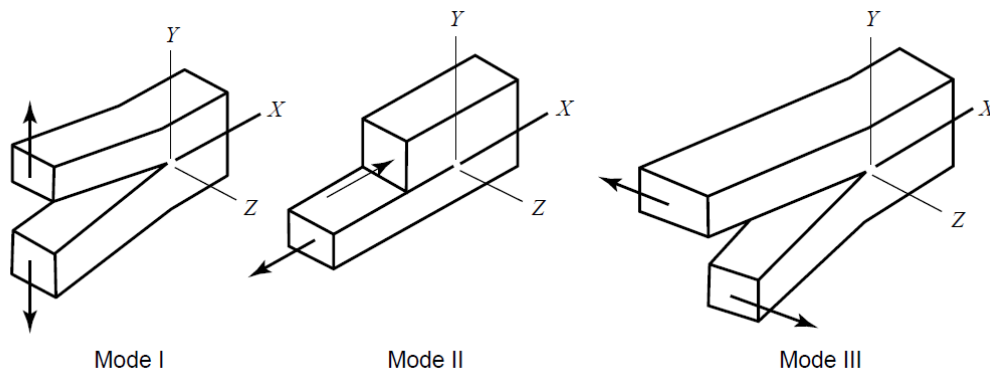


Figure 2.2. Various modes of failure [29]

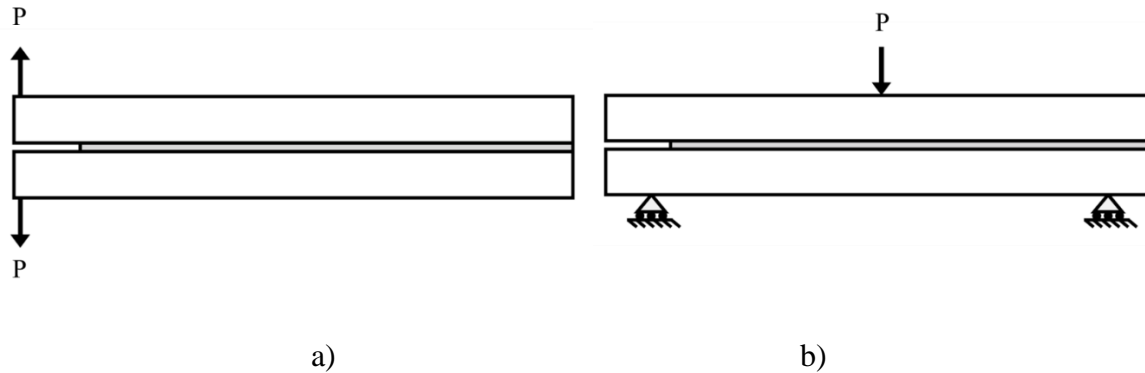


Figure 2.3. Schematic of a) Double cantilever beam test b) End Notched Flexural test [17].

### *2.3 Parameters Affecting Strength of Bonded Joints.*

Manufacturing processes, surface preparation, geometric, material and environmental parameters affect the bond strength of adhesive bonded joints [30]. A summary of the effect of bond line thickness, bonded area, adherend thickness and ply orientations in the case of composite adherends have been summarized in this section.

#### *2.1.1 Effect of Adhesive Bond Line Thickness*

Bond line thickness is one of the major parameters in determining the strength of bonded joints. A bond line thickness in the range of 0.05 to 0.5 mm has been found to yield optimum bond strength [31]. The exact nature of variation in failure load depends on the type of loading and nature of the adhesive [21]. In the bonded joints with metallic adherends and strong composite adherends, strain energy release rate or fracture energy ( $G$ ) plays a significant role in the load sustainability of such bonded joints. Gardon et.al [32] studied the behavior of ductile acrylic polymer adhesives using a mode 1 peel test and found that the strain energy release rate was proportional to the thickness of the adhesive which could be the result of distribution of the load on a larger area [33].

Bascom [34] and Loch [35], using a ductile rubberized adhesive and the Tapered Double cantilever beam test (TDCB), found that the fracture energy peaked when the plastic zone diameter, ahead of a crack face equaled to the bond line thickness. Lee, et al.[20] studied the effect of adhesive ductility and the crack path and concluded that the fracture energy increases, peaks and then drops with an increase in bond line thickness. Single lap joints also exhibit a similar trend of reduction of strength with an increase in bond line thickness with the exception of elastomeric adhesives. The reasons for this behavior have been investigated by various researchers. Adams, et al. [36] attributed the reduction in strength to a higher probability of micro-cracks and voids. Such voids would act as stress concentrators and reduce strength, more severely in case of bonds with brittle adhesives. Banea, et al. [37] studied the effect of thickness variations with a ductile polyurethane adhesive and concluded that the reduction in failure loads was not as severe as the case of a brittle adhesive. Gleich, et al. [31] compared the stresses near the ends of the overlap of a single lap joint using a stress analysis at the 3<sup>rd</sup> node from the corner of the joint using finite element analysis. They found that the stresses near the interface increase as the adhesive thickness increases. Banea, et al.[37] also observed a shift in failure mode from the middle of the adhesive to the interfaces with an increase in thickness, validating this theory. Crocombe [38] explained the reduction of failure loads using the global yield criterion which suggests that the entire bulk of the adhesive reaches yielding close to failure. For thicker bond lines, the “elastic reserve” for sustaining further increase in stresses does not exist because of a more uniform distribution of stresses along the overlap as compared to thinner bond lines. Similar results are observed in composite bonded joints. Rahman, et al. [39] studied the effect of thickness variations on composite

bonded joints and observed a reduction in strength with an increase in bond line thickness.

### *2.1.2 Effect of Bonded Area*

An increase in overlap length would result in an increase in the bond strength. The amount of increase in strength with overlap length depends upon the adherend and adhesive material along with the type of loading [30]. Neto, et al. [40] investigated the effect of increase in overlap length for a composite bonded joint with a ductile and a brittle adhesive. The strength increased linearly with an increase in overlap length for the ductile adhesive while the failure load for the brittle adhesive increased linearly initially up to 20 mm of overlap length and then then exhibited a non-linear increase in strength. The failure mode was found to depend on the overlap length with cohesive failure being observed in joints up to an overlap length of 20 mm while an adherend failure being observed on overlap lengths beyond 20 mm. A similar behavior was observed by Li, et al. [41] who observed a nonlinear increase in failure strength with an increase in overlap length for a CFRP adherend and a brittle adhesive. Gultekin, et al. [42] observed a linear increase in failure load with an increase in overlap length using aluminum adherends but the increase in joint width had a higher influence on the increase in strength for the same bonded area. Park, et al. [43] observed similar results with a thick shear adhesive test using aluminum adherends.

### *2.1.3 Effect of Adherend Thickness*

Increasing the adherend thickness would increase the eccentricity in single lap joints resulting in more peel stresses in the joint [44]. With the increase in adherend

thickness, the bending stiffness of the adherends will also increase which would result in lower joint rotations in case of a single lap joint. Aydin, et al.[45] compared the lap shear strengths for a bonded joint with an aluminum adherend and a ductile adhesive, with various adherend thickness and overlap lengths. For overlap lengths up to 50 mm, they found no significant increase in the failure loads with an increase in adherend thickness. The failure loads differed significantly for a 100 mm overlap length. Li, et al. [41] found that the lap shear strength increased by only 42% for double lap joints when the adherend thickness was doubled.

#### *2.1.4 Effect of Ply Orientations*

Ply orientation and stacking sequence play a significant role in determining the joint strengths of adhesively bonded composite joints [46]. The in plane bending stiffness depends on the position and the orientation of the plies with certain stacking sequences producing higher bending stiffnesses [1]. A higher bending stiffness would reduce the longitudinal out of plane bending curvature thereby reducing the peel stresses in the adherend and preventing adherend failure [47]. Hart-Smith [47] found that the position of the 0° plies at the outer edges of the laminated adherend in contrast with their position close to the neutral axis is associated with higher joint efficiency. Renton, et al. [48] studied the stresses in the adhesive for different ply orientations and found that the adherends with higher bending stiffness produced lower shear and peel stresses at the ends of the overlap. Ozel, et al. [49] showed that, depending on the stacking sequence, the composite adherends can have almost a difference of 123% in failure loads. Khan, et al. [50] studied double lap joints with composite adherends and found that when 90° plies are placed in contact with the bond line, the failure strength was lowest and an interply

failure was observed. Purimpat, et al. [51] concluded differently that when higher ply angles w.r.t the longitudinal direction are placed adjacent to the bond line, the joint strength improved by almost 30% due to complex crack paths in the adherends. Similarly, Meneghetti, et al. [52,53] in their studies on fatigue behavior of bonded composites concluded that plies at 45° angle w.r.t the loading direction, yielded higher strengths. The contradiction of results related to the position of the ply angle in contact with the bond line on the joint strength was addressed by Kupski, et al. [46]. They concluded that the increase in the bond strength depended on the ply angle in contact with the bond line as well as the overall longitudinal bending stiffness of the adherends.

## *2.2 Defects and Imperfections*

Bonded joints are prone to defects and imperfections. Common defects in bonded joints are voids and inclusions. One of the initial works on the effect of bond line inclusions was carried out by Schonhorn, et al.[54] and Wang, et al. [55]. PTFE films were inserted in a joint bonded with ductile and brittle adhesives respectively. The defects were placed at various positions along the overlap length and across the width of a single lap joint in each case. There was a reduction of failure strength when the defects were introduced. The average shear strength at failure was found to be not significantly affected in the case of a ductile adhesive in comparison with the brittle adhesive. This was attributed to the presence of edge effects in brittle adhesives which causes higher stresses at the ends of the joint which leads to a rapid propagation of cracks. These higher stresses raise the average shear stress while in case of ductile adhesives, failure occurs due to global yielding. Olia, et al. [56] presented a 2D theoretical solution for single lap bonded joints with voids placed at various positions and sizes. They found that when

voids are placed sufficiently close to the ends of the bond length, the stresses at the ends of the joint could increase by almost 25%. Lang and Mallick [57] found experimentally that a deliberate gap introduced by recessing the bond along with a spew fillet at the ends of a single lap joint did not cause a significant effect on the strength of bonded joints. Heslehurst [16] reviewed the effects of defects on strength of bonded joints. He specifically focused on weak bonds and voids. The elastic-plastic shear stress/strain approach developed by Hart-Smith [58] was used and it was found that any weakness in the bond line would cause a change in the peak stresses during load transfer. It was also found that the peel strength of the joint would reduce owing to a reduction in peel stiffness on account of weak bond lines. This would cause an increase in the peel and shear stresses at the ends of the overlap, reducing the load bearing capacity of the joint. Berry, et al. [59] studied the effect of circular shaped defects in the middle of the bonded area of a single lap joint. They used a Polytetrafluoroethylene (PTFE) film commonly known as Teflon, to simulate the effect, which was found to be good for its non-adherence to the adhesive. They concluded that the presence of the circular defect in the middle of the bonded joint reduced the overall stiffness which resulted in a reduction of load bearing capacity of the joint. Pareira, et al. [60] studied epoxy and acrylic bonded stainless steel joints. Thick adherend lap shear tests performed showed that the epoxy adhesives exhibited a reduction in failure loads when defects were placed at the either ends of the overlap. Moura, et al.[61] investigated the effects of embedded and through thickness strip defects in the bond line of a composite bonded joint. It was observed that the joint strength reduces as the defect position was moved closer to the ends of the overlap which was explained by an increase in the stresses at the ends of the overlap.

Furthermore, embedded and through thickness defects exhibited similar failure loads. You, et al. [62] investigated the effects of gaps in aluminum double lap joints. Experimental results indicated that the gaps in the middle of the adhesive were not found to have a significant effect on the strength of the bonded joint irrespective of its length along the overlap. Finite element modeling revealed that there was an increase in the stresses at the ends of the overlap similar to that discovered by previous researchers with single lap joints [59–61]. Engerer, et al. [63] studied the effects of gaps in bonded joints by comparing acrylic tape and an epoxy based adhesive. They found that the decline in failure strength in the ductile adhesives was higher than that with brittle adhesives. Furthermore, when the adherends were machined with a  $10^\circ$  taper at the ends of the overlap, there was an increase in the failure strength. This was attributed to the reduction of peel stresses due to the introduction of the adherend taper. Xu, et al. [64] studied the effect of local debonding, weak bonding and voids, varying their size and position along the overlap, in a metallic single lap bonded joint. They applied cohesive zone models to consider the effects of defect size and also used the modified Gurson model [65] to simulate the effect of defect locations. Karachalios, et al.[10] carried out a parametric study with two different types of adhesives, three different types of steel adherends based on their ductility, and with rectangular and circular defects located at the center of the bonded joint. They observed that for a ductile adhesive and a high strength steel adherend, there is a linear decrease in bond strength when size of the defect increases. For a medium and mild carbon steel adherend with a ductile adhesive, the decrease in failure load was non-linear with the load plateauing for smaller defect sizes. When high strength steel adherends are used with a brittle adhesive, the reduction in failure load

becomes non-linear with increasing defect size, while a similar behavior is observed for low and mild carbon steels. This led them to conclude that the ductility of the adherends, nature of the adhesive and the size of the defects if any, would influence the failure loads. A numerical study on how crack growth in a bonded joint is influenced by the presence of voids was performed by Sengab, et al. [66]. The growth of a crack in presence of a void was studied in a single lap joint having a pre-existing crack. It was found that when the void was present near the crack tip, the crack would get deflected further away from the interface resulting in higher failure loads. A flat shaped void, produced by applying consolidation pressure on rounded cracks, also contributed to kinking of the crack away from the interface. Ribeiro, et al. [67] studied the effect of void size on bonded composite adherends with a ductile and a brittle adhesive, for two different overlap lengths. They found similar results as the study carried out by Karachalios, et al.[10] where the ductile adhesive was significantly affected by the presence of voids. They were able to use the cohesive zone modeling successfully in their analysis since the failure mode of the joint was cohesive. The effect of kissing bonds was studied by Jeenjitkaew, et al. [68] by using a 3D finite element model to measure strains near the region where kissing bonds occurred. A unique strain 'signature' was found to be associated with the presence of kissing bonds which could be used to determine the presence of kissing bonds using digital image correlation techniques. Heidarpour, et al. [69] investigated the effects of 2D (laminar) and 3D (through thickness) defects, of square, triangular and circular shapes, embedded in a single lap joint bonding aluminum adherends. They found that the through thickness defects had a greater impact on the failure load as compared to the laminar ones. A similar study, but with a dissimilar adherend combination i.e. high strength steel

and CFRP , embedded with through thickness defects of elliptical and circular shapes, was performed by Chu, et al. [70]. They found that the shape of the defect did not have an impact on the failure load of the bonded joint. They also found that when the defect moved from the center to the ends, the failure occurs in the CFRP side due to higher stresses generated in the CFRP adherend.

### *2.3 Strength Prediction Techniques*

Static strength prediction of bonded joints can be performed using many methods. The prominent approaches and the various methods under each are discussed in this section.

#### *2.3.1 Analytical Methods*

Analytical methods utilize closed or open form solutions for stress distributions in a bonded joint to determine their strength. The simplest method would be to compare the analytically calculated stresses to their critical values to estimate the failure load of the joint [17].

The simplest of the techniques for predicting the failure load would be to measure the shear stress in the bond line using

$$\tau = \frac{P}{b * l} \quad (2.1)$$

where:  $P$  = Applied load  
 $b$  = Width of the joint  
 $l$  = Overlap length

The failure load can be calculated by substituting the maximum shear stress that the adhesive can sustain, measured experimentally, in Equation 2.1. This method is very

simple and easy to use but does not represent the actual stress distribution in the joint. Hence it is limited to quantify the strength of adhesives in ASTM and ISO standards [71]. One of the initial models to estimate the stress states in a bonded joint was proposed by Volkersen [72] who developed a shear lag model in which the adhesive deforms only in shear while the adherends could deform in tension. The adhesive shear stress as per the Volkersen's model is given by

$$\tau = \frac{Pw \cosh(wX)}{2bl \sinh(w/2)} + \frac{(\psi - 1) \sinh(wX)}{2(\psi + 1) \cosh(w/2)} \quad (2.2)$$

where:  $P$  = Applied load

$$w^2 = tt/t_b$$

$$\phi = \frac{G_a l^2}{E t_t t_a}$$

$$X = \frac{x}{l}$$

$x$  = Length along the overlap

$l$  = Overlap length

$t_t, t_b$  = Top and bottom adherend thickness

$G_a$  = Adhesive shear modulus

The drawback of Volkersen's model was that it did not account for bending of adherends which would result in an under-prediction of shear stresses. This was overcome by Goland and Reissner's model [6]. Volkersen's and Goland and Reissner's analysis are considered as classical theories in adhesive bonding as they laid foundations for the analysis of bonded joints. The classical analyses have their drawbacks, namely the non-consideration of stress variation across bond line thickness, ignorance of the stress free condition at the ends of the overlap and ignorance of the through thickness shear and normal deformations in the adherends [71]. Ojalvo and Eidinoff built upon Goland and Reissner's work by incorporating the effect of adhesive thickness. The Ojalvo and

Eidinoff's theory improved the stress predictions at the ends of the overlap as compared to the classical theories. Despite these merits, the Ojalvo and Eidinoff's model fails to account for the stress-free condition at the ends of the overlap. This was taken into account using higher order theories proposed by Allman [74] and Chen and Cheng [75]. The position of the peak adhesive stress was found to depend upon the relative flexibility of the adherend and the adhesive in Allman's theory. The peak stresses were found to be at a distance of 20% of adherend thickness, from the ends of the overlap by Chen and Cheng. Tsai, et al. [76] improved the Goland and Reissner's model by incorporating the out of plane shear deformations of in the adherends. The shear stresses were assumed to vary linearly across the thickness of the adherends. It was found that the improved solution closely matched the experimental results than the classical theories especially when composite adherends are considered. Hart-Smith [47,58] proposed an elastic plastic model by assuming the outer end of the bond line to be a plastic region while the inner region as an elastic region for the sake of analysis. Large deformations of the joint were also considered in the analysis. Sousa, et al. [77] compared the various analytical models for predicting strength of bonded joints. The Hart-Smith model was found to correctly estimate the failure loads of joints bonded with brittle adhesives. Crocombe's global yielding criteria [38] was found to predict the failure load of ductile adhesives effectively.

The advantages of using analytical methods include the ease of use and a faster output of results when compared with the other methods of strength estimation which makes them ideal for an initial assessment of strength of bonded joints during the design phase [17]. The drawbacks of analytical methods are the simplification of assumptions in the elasticity of the adherends and adhesives, and a neglect of through thickness

variations of the adhesive [71,78] which makes it unsuitable for predicting the actual strength of bonded joints. This has resulted in a limited use of analytical methods for strength prediction [17].

### *2.3.2 Continuum Based Methods*

Continuum based methods use the stress results from finite element analysis and a comparison of the stresses to a failure criterion to determine the strength of bonded joints [79]. Ribeiro, et al. [80] used the Tsai-Wu criteria in the adhesive to predict the onset of failure in single lap joints by measuring the parameters at corners of defects introduced in the joint. Tsouvalis, et al. [81] used the Von Mises failure criteria to a composite to metal butt joint. This was based on an assumption that the composite adherend is perfectly bonded to the steel adherend and that cohesive failure occurs in the joint. Ayatollahi, et al. [82] used a criteria based on longitudinal strains and the theory of critical distances [83] to predict failure in lap joints. The method relies on two experimental data points joints with two overlap lengths for strength prediction. The longitudinal strains along the length of the overlap for two joints of different overlap lengths are plotted. The point of intersection of the strains is identified and the position of intersection and the corresponding strain forms the criterion for strength prediction. The failure load for a joint in investigation is found by finding the force corresponding to the critical value of longitudinal strain measured at the critical location. An example of this is shown in Figure 2.4. This method is mesh independent and uses a linear elastic approach for determining the strength and predicts failure loads effectively when a cohesive failure is observed [82]. A modification of this method, named as the critical normal strain method

was introduced by Razavi, et al. [84]. This method is able to predict failure loads of a hybrid composite to metal double strap joint.

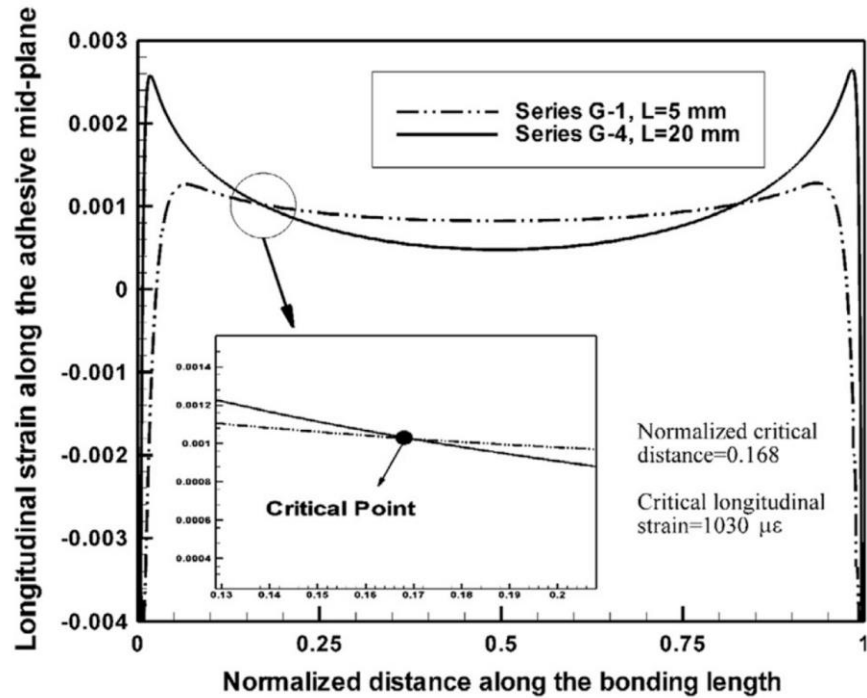


Figure 2.4. Critical distance and critical longitudinal strain for measuring failure load using critical longitudinal strain method[82].

Another method to predict the failure of bonded composites, especially when a fiber tear failure is involved, is the Critical Zone method. One of the obvious approaches to estimate the failure loads is to find the force on the model which causes the stress or strain at a particular point to exceed the failure criterion. Using this approach in an FE model results in inaccuracies due to stress singularities. Stress singularity is produced in bonded joint configurations at the adhesive adherend interface and the corners in case of lap joints as shown in Figure 2.5. Singularities are an artifact of numerical analysis and do not exist in nature as stress values are always finite and sharp rectangular corners do not exist [85]. These singularities would cause the stresses at such locations to increase

continually with a decreasing mesh size. The problems with singularity have been overcome by considering stresses at a certain distance from the point singularity [31,86].

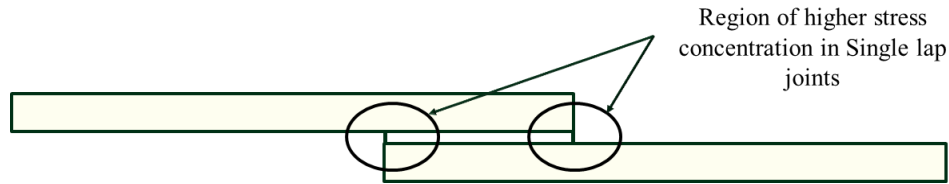


Figure 2.5. Regions of stress concentration in a Single lap joint

McClintock [87] found that the fracture would occur in a material when a critical shear strain is attained over a critical volume of a material. Based on this principle, Sheppard, et al. [85] proposed the damage zone model for prediction of strength of bonded joints. The model is based on the growth of micro-cracks and voids in the material till it coalesces into a crack as shown in Figure 2.6. The process involves testing of a sample for strength, analyzing an FE model of the joint at the failure load and identifying the critical volume and using this critical volume to calculate the failure load in a model being investigated. The Critical zone method is also mesh independent like the Critical longitudinal strain method. The advantage of Critical Zone method over the other approaches such as Critical longitudinal strain method is that it requires only one experimental data point in contrast with two required for the Critical longitudinal strain method. This method was further advanced by Rahman, et al. [39] who applied composite failure criteria for prediction of fiber tear failure in composites. Various failure criteria including the maximum stress/strain criterion, Yamada-sun criterion, Azzi-Tsai criteria, Hoffman`s criterion and Tsai-Wu criterion were investigated for composite bonded joints with varying adhesive thickness and overlap lengths.

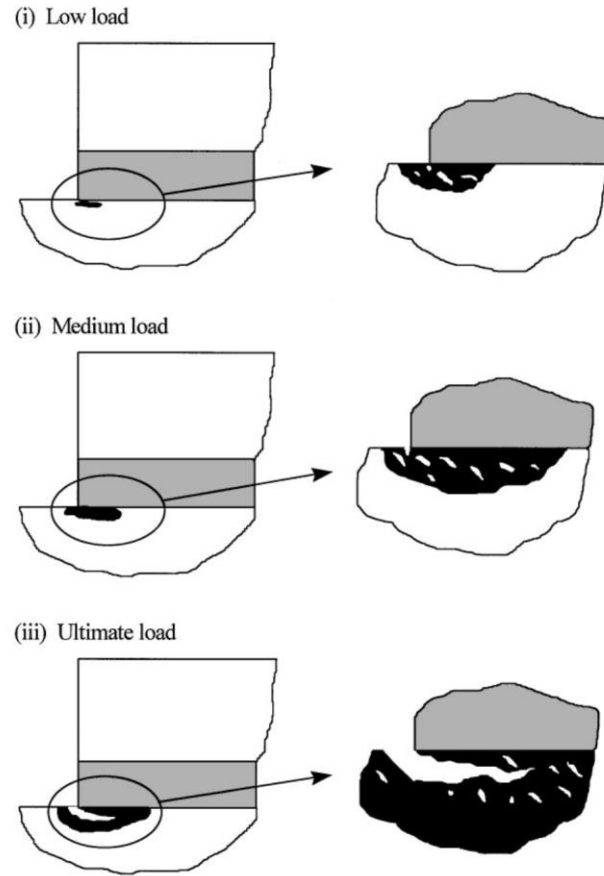


Figure 2.6. Damage zone in a composite adherend[85]

The equations of the various criteria used are:

1) Maximum stress criterion

$$\begin{aligned}
 -X_c &\geq \sigma_x \geq X_t \\
 -Z_c &\geq \sigma_z \geq Z_t \\
 \sigma_{xz} &\geq S_{xz}
 \end{aligned}
 \tag{2.3}$$

2) Yamada Sun criterion [88]

$$\frac{\sigma_z^2}{Z_t^2} + \frac{\tau_{xz}^2}{S_{xz}^2} \geq 1
 \tag{2.4}$$

3) Azzi-Tsai Norris criterion [89]

$$\frac{\sigma_z^2 - \sigma_x \sigma_z}{X_c X_t} + \frac{\sigma_z^2}{Z_t^2} + \frac{\tau_{xz}^2}{S_{xz}^2} \geq 1
 \tag{2.5}$$

4) Hoffman`s criterion [90]

$$\frac{\sigma_z^2 - \sigma_x \sigma_z}{X_c X_t} + \frac{\sigma_z^2}{Z_t Z_c} + \frac{X_c - X_t}{X_c X_t} \sigma_x + \frac{Z_c - Z_t}{Z_c Z_t} \sigma_z + \frac{\tau_{xz}^2}{S_{xz}^2} \geq 1 \quad (2.5)$$

4) Tsai- Hill criterion [91]

$$\frac{\sigma_x^2}{X_t^2} + \frac{\sigma_z^2}{Z_t^2} - \frac{\sigma_x \sigma_z}{X_t^2} + \frac{\tau_{xz}^2}{S_{xz}^2} \geq 1 \quad (2.6)$$

where:  $X_t, X_c$  are the longitudinal failure strengths of the composite in tension and compression  
 $Z_t, Z_c$  are the transverse failure strengths of the composite in tension and compression  
 $S_{13}$  is the interlaminar shear strength of the composite  
 $\sigma_x, \sigma_y, \sigma_z, \tau_{xz}$  are the stress components in 1, 2 and 3 directions as shown in Figure 2.7

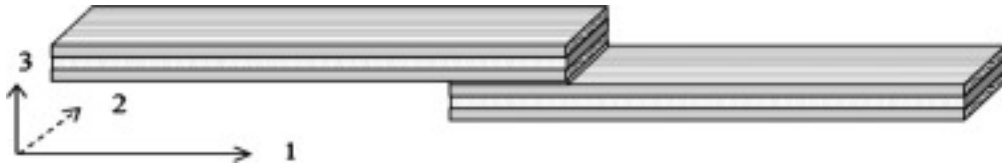


Figure 2.7. Schematic of the single lap bonded joint with the coordinate axes [39]

Rahman, et al. [39] found the Azzi-Tsai criteria to be effective in determining the bond strength for a light fiber tear failure observed in their specimens. The continuum-based approaches provide a simple and easy to implement method for bonded joint analysis. The major drawback of this method is when used in its simplest form, it is subject to the presence of singularities. Continuum based methods also fare poorly when ductile adhesives are involved [17]. The effect of singularities can be overcome using methods like the Critical longitudinal strain method and Critical Zone method. Furthermore, in joints exhibiting fiber tear failure, the Critical Zone method is very effective in predicting the failure loads [39], given the fact that the energy based failure

methods such as Cohesive Zone modeling and Extended Finite Element Modeling (XFEM) would fail to do so [17]. In conclusion, continuum-based methods should be used carefully, depending on the materials used and the failure mode exhibited, while using it to predict the failure loads.

### *2.3.3 Fracture Mechanics-Based Methods*

Fracture energy methods uses material characteristics such as Strain Energy Release Rates (SERR), J-Integral or Stress Intensity factors to estimate the onset of crack formation and propagation in materials [17,92]. In contrast with continuum mechanics, fracture mechanics can handle stress singularities [93]. The SERR can be determined experimentally using the Double cantilever beam tests and End Notched flexural tests for modes I and II respectively. The SERR determined experimentally can be implemented in a commercial FE software such as ABAQUS using the J-Integral [94] approach or the Virtual Crack Closure Technique method (VCCT) [95]. The viability of the VCCT technique was studied by Goh, et al. [96], who compared the VCCT technique with Linear Elastic Fracture Mechanics (LEFM) for scarf joints and found that it was able to predict the failure strengths for large defects while underpredicted the strength for smaller ones. Cameselle-Molares, et al. [97] used VCCT to predict failure strength of double lap joints with composite adherends with brittle adhesives. Another method used is the Finite Fracture Method (FFM) approach which was developed by Leguillon [98]. FFM uses a coupled stress and energy approach to predict the onset of failure in materials. According to FFM , the energy and the stress criteria should be fulfilled for the crack to initiate as shown in Figure 2.8. The stress increases while the SERR decreases with an increase in crack area as shown in Figure 2.8 both of which when coupled give an upper and a lower

bound respectively for crack initiation. The drawback of FFM is that it is only applicable for brittle adhesives [17].

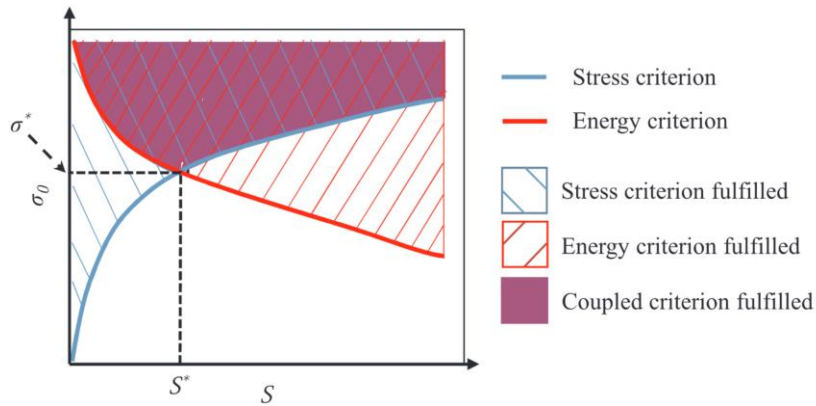


Figure 2.8. Finite Fracture mechanics principle [99].

#### 2.3.4 Damage Mechanics-Based Methods

Damage mechanics utilizes a progressive degradation of material stiffness upon an increase in the applied load, which makes it capable of determining arbitrary crack paths unlike cohesive elements [17]. Continuum damage model (CDM) uses an elastic-plastic behavior of materials, clubbed along with other criteria such as Drucker-Prager criteria, to model behavior of materials. CDM was used by Garcia, et al. [100] to predict the path of crack propagation through a ductile adhesive. Another approach is to use a traction-separation law to model the behavior of the material as demonstrated by Chousal, et al. [101] who used a triangular traction separation law to model the adhesive. Key advantage of the damage mechanics-based approaches is its versatility in being able to predict different damage mechanisms. An accurate prediction of strength is also possible using damage mechanics. A major drawback of using damage mechanics is in

material characterization, wherein calibration of material properties and their interpretation can be complicated [17].

### *2.3.5 Cohesive Zone Modeling*

Cohesive zone modeling combines the fracture mechanics and damage mechanics approaches to predict the failure of materials. Cohesive Zone Modeling (CZM) is one of the widely used methods in literature [17]. The origin of CZM is from the works of Barenblatt [102] and Dugdale [103]. CZM relies on the use of a traction -separation law along with the fracture parameters to determine failure as shown in Figure 2.9. The behavior of the material can be tailored into the model by changing the shape of the traction-separation law. Ductile adhesives were found to be accurately modeled using a trapezoidal law while a triangular law was found suitable for brittle adhesives [104]. The material parameters pertaining to the traction-separation laws are measured using Double Cantilever Beam and End Notched Flexural tests. The material parameters can be input into a commercial Finite Element Analysis software such as ABAQUS, which have built in solvers for implementing CZM [105]. CZM can be used either using the local approach or continuum approach. In local approach, CZM elements can be defined on the surfaces separating the adherend and the adhesive as shown in Figure 2.10. The local approach helps in determining de-laminations or interfacial failures. Continuum approach defines CZM elements as 2D or 3D elements. Adhesives can be modelled using this approach as being one element thick. Despite the wide use, CZM methods have the limitation of having to prescribe a failure path prior to analysis. If the failure is localized in the adhesive or between plies, this approach can be applied. In real life applications,

other forms of failure including tearing of adherend fibers for instance, cannot be predicted using CZM.

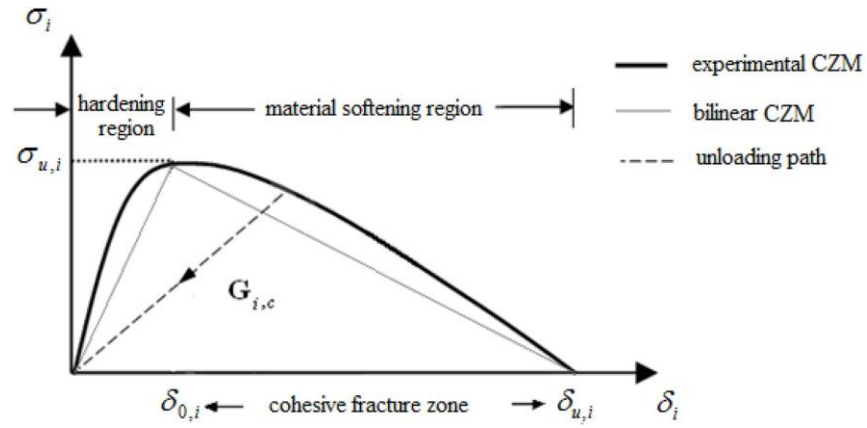


Figure 2.9. Traction-separation law for Cohesive Zone modeling [17]

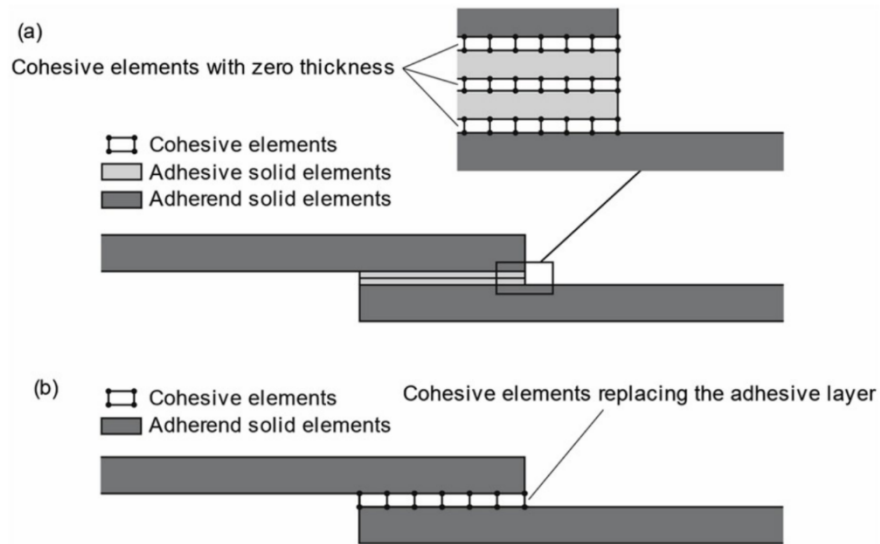


Figure 2.10. a) Cohesive elements in a local approach and b) Continuum approach [17]

Adhesive bonded joints have been widely studied in the literature. Major parameters affecting the strength of bonded joints are bond line thickness and bonded area. An increase in the bond line thickness results in a reduction of bond strength in case of brittle and ductile adhesive. The reduction in bond strength has been attributed to an increase in the stresses near the ends of the overlap for a single lap joint and to the high likelihood of presence of defects such as micro-voids and cracks in the adhesive. Failure strength of bonded joints also increases with an increase in the bonded area. Studies on the effect of overlap length found that failure strength increases linearly with increase in overlap length for ductile adhesives while the increase plateaus for a brittle adhesive. An increase in bond joint width also increases the strength of bonded joints more than an increase in the overlap length for the same bonded area. Studies also showed that adherend thickness variations had no significant effect on the bond joint strength. In case of Fiber reinforced polymer composite adherends, the ply orientations influence the strength of bonded joints. The orientation of the ply adjacent to the bond line and the overall stiffness of the adherends influence the bond joint strength.

Defects and imperfection reduce the load carrying capacity of bonded joints. Previous researchers have focused on the effect of defects such as voids and inclusions in the bond line. Bond line defects such as voids reduce the failure strength of bonded joints by reducing the load transfer area and increasing the average stresses in the bond. The increase in stresses and reduction in failure strength depend on the nature of the adhesive and adherends and the size and position of the void.

Various methods have been proposed for predicting the bond joint strength such as Analytical methods and numerical methods such as Continuum based method, Fracture

energy-based method, Damage mechanics-based methods and Cohesive Zone modeling. Each method has its own advantages and disadvantages with applicability of each method depending on the complexity of the bond configuration and the nature of the adherent and adhesive. Cohesive Zone model has been found to be the most effective method to assess the failure strength of bonded joints. Extensive characterization requirements and limited applicability to cases exhibiting adherend failures are the drawbacks of Cohesive Zone Modeling method. Fracture mechanics-based methods such as Finite Fracture methods and Virtual Crack Closure Technique though accurate in prediction of failure strength, require a known location of failure initiation and are accurate only in the case of brittle adhesives. Continuum-based methods using a maximum stress or strain-based failure criteria, are the simplest to implement while having the drawback of dealing with stress singularities which result in inaccurate predictions. Critical Zone method which overcomes the effects of singularities in the joints has been found to be effective in predicting the strength of bonded joints especially when light fiber tear adherend failure is observed in experimental specimens.

A survey of the literature reveals that the effects of defects such as inclusions in the adherend and imperfections such as bond line thickness variations and incomplete distribution of the adhesive across the bond area have not been sufficiently addressed. Imperfections such as bond line thickness variation and incomplete adhesive distribution may occur due to improper fabrication techniques. Contamination from foreign objects can result in inclusion defects in the adherends of bonded joints. The effect of such imperfections and defects on the integrity of bonded joints has not been fully understood. The current dissertation aims to investigate the effects of such imperfections and defects

on the strength of bonded joints. Critical Zone method is used to predict failure strength since light fiber tear failure is observed in the specimens tested. The applicability of the Critical Zone method as a tool for failure prediction is investigated for bonded joint configurations having each type of defect or imperfection. Furthermore, the capability of non-destructive testing to identify the shape and size of imperfections is established in the case of bonded joints with incomplete adhesive distribution.

## CHAPTER THREE

### Methodology

The bonded joints studied in the current dissertation were fabricated in a single lap joint configuration. A single strap joint configuration was used for the study of strap joints as described in Chapter Seven. The current chapter describes the procedure used for fabrication of the lap joints and carbon fiber adherends. Materials characterization and testing for the estimation of mechanical properties required for Finite Element modeling and analysis are also described.

### *3.1 Experimental Work*

#### *3.1.1 Carbon Fiber Adherend Fabrication*

Toray T700 unidirectional carbon fiber fabric (Soller Composites, Franklin, NH, USA) was cut to the required dimensions of 12" x 6" and laid up on an aluminum backing plate using a wet layup process. Each layer was impregnated with a two-part epoxy resin Proset INF 114-211 (Proset, Bay city, Michigan, USA), using a paint brush. The excess resin on the fabric was scraped off using a plastic scraper. The same process was repeated for each layer until 6 layers were laid up. The aluminum backing plate was bagged with the help of two side adhesive tapes, placed at the periphery of the plates. A single opening was provided for the excess resin to flow out of the bagged plate by means of a PVC hose fit with a stopper. The PVC hose was connected to a vacuum pump to draw out the air and excess resin from the bag. Figure 3.1 shows the complete setup including the aluminum plate with laid up carbon fiber fabric and vacuum bagging. The

vacuum bagged aluminum plates were cured at room temperature for 8 hours followed by a heat cycle involving a step-up and step-down temperature ramp of 1°C/min, for an hour each, with a hold at constant temperature of 82°C for 8 hours in between them. The test coupons were cut from the cured carbon fiber plates using a circular tile saw.

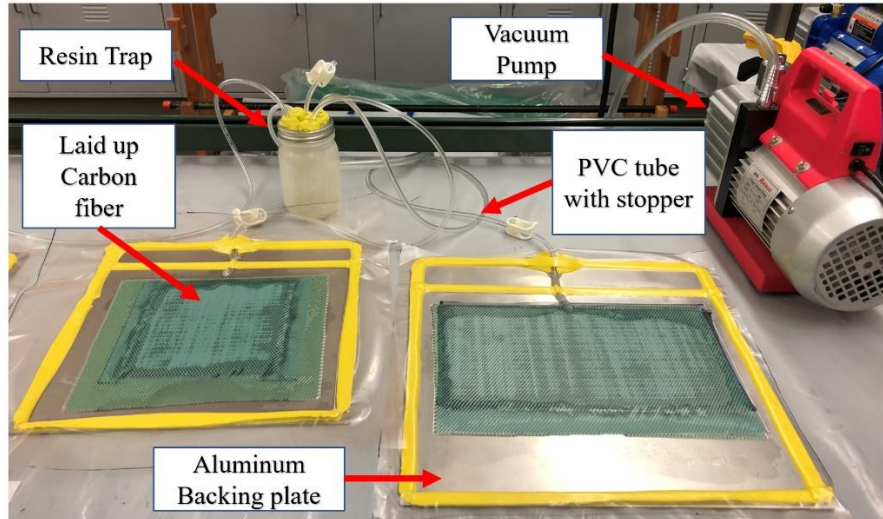


Figure 3.1. Layout of wet layup process for fabrication of carbon fiber adherends

### 3.1.2 Fabrication and Testing of Bonded Joints

The bonding surfaces of carbon fiber adherend test coupons were manually sanded with a 220-grit sandpaper. The bonding surfaces were then cleaned by an isopropyl alcohol wipe to remove any debris left over from sanding. The adherends were then placed in the bond fabrication fixture as shown in Figure 3.2. Spacers of the required thickness were placed at the ends of the overlap to maintain the required bond line thickness. Hysol 9309 NA (Henkel Corporation, Westlake, Ohio, USA), a two-part epoxy adhesive was used for bonding the adherends. The bonded test coupons were assembled in the fixture in the required joint configuration. The coupons were placed in the fixture for 24 hours followed by a cure in an oven at 82°C for an hour, for faster curing as per the

manufacturers recommendation [106]. The bonded specimens were tested for lap shear strength on an Instron 3382A (Instron, Massachusetts, USA) tensile testing machine, having a load cell of 100 KN, by loading at a rate of 0.05 mm/min. The bond line thickness, required for the bond line thickness variation study, was measured using a Keyence VR3100 3D microscope (Keyence corporation, Itasca, Illinois, USA). The specimens were placed with the cross section of the bonded coupons laid flat on the microscope bed, such that the opposite end faced the objective lens as shown in Figure 3.3. The thickness was measured using the image processing software provided by Keyence microscope.

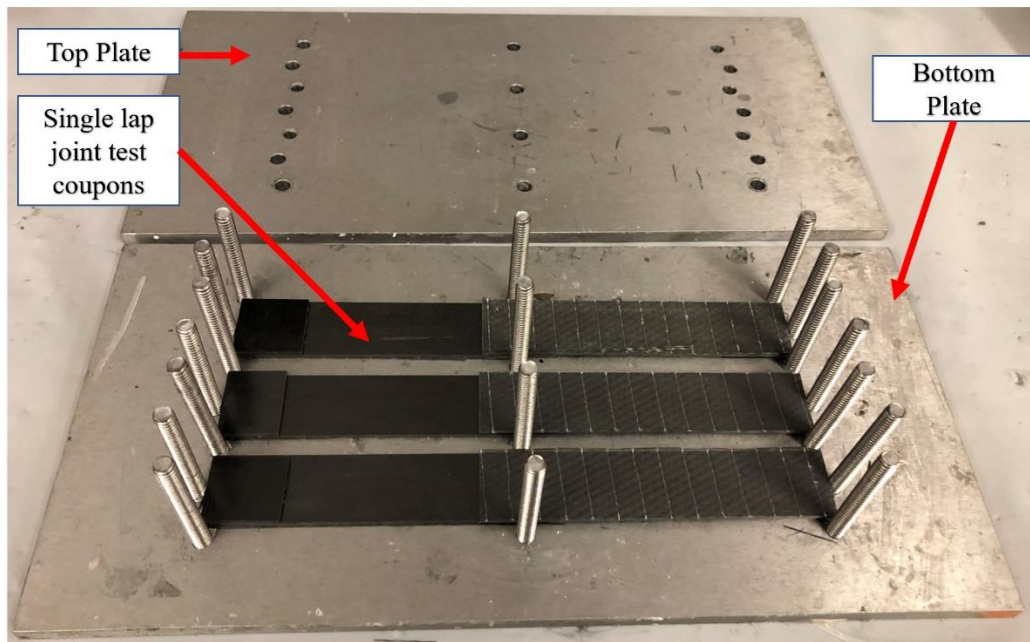


Figure 3.2. Single lap joint test coupon fabrication fixture

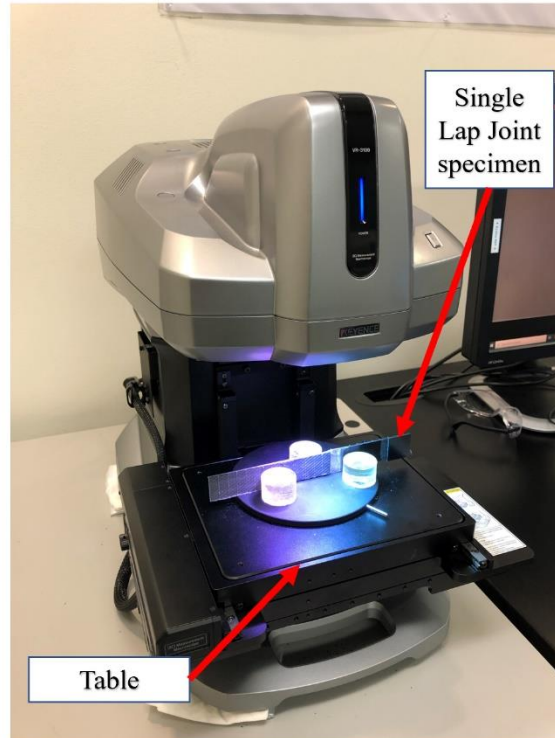


Figure 3.3. Measurement of bond line thickness from cross-section of a single lap joint using Keyence microscope.

### 3.1.3 Materials Characterization

Characterization of material properties namely the strength and stiffness, was performed for both the adherend and the adhesive materials for the purpose of building FE models, for stress calculations and strength predictions.

#### 3.1.3.1 Carbon Fiber Characterization

*3.1.3.1.1 Tensile Testing.* Unidirectional carbon fiber reinforced polymers can be considered as transversely isotropic [1] i.e. the transverse and out of plane elastic properties are assumed to be equal. Characterization of the elastic and tensile strength properties of laminated long carbon fiber composites was performed in accordance with ASTM D3039 standard [107]. The specimens were cut from the laminate plates having  $0^\circ$

and 90° orientations w.r.t to the loading axis, in accordance with ASTM D3039 standard, as shown in Figure 3.4.

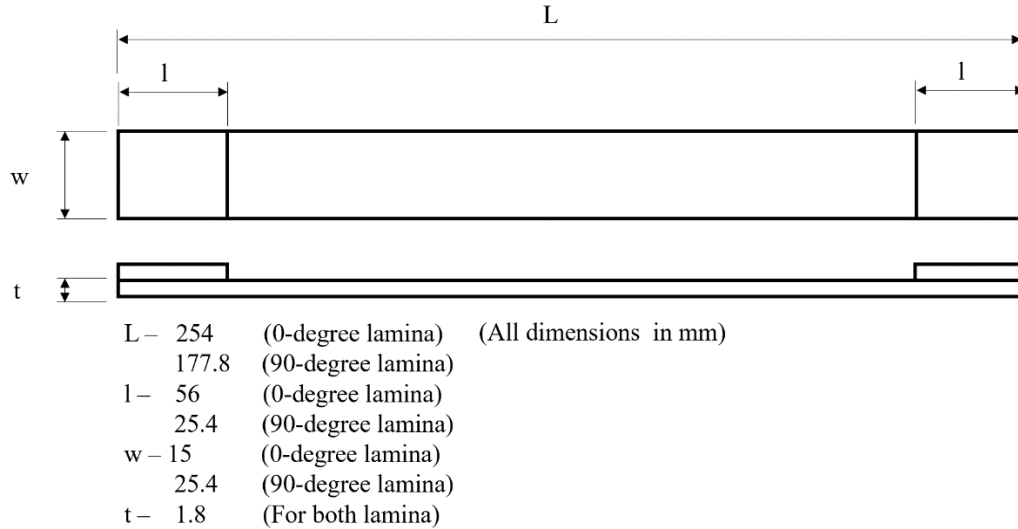


Figure 3.4. Dimensions of tensile test bars for 0° and 90° orientations [107]

Gripping tabs were bonded to the ends of each specimen. Tensile tests were performed using the Instron 3382A tensile testing machine, having a load cell rating of 100 KN, at displacement-controlled loading rate of 0.05 mm/min. Rosette type strain gauges, manufactured by Micro-Measurements (VPG group, Raleigh, NC, USA), having a resistance of 350  $\Omega$  and a gage factor of 2.06, were bonded to each of the specimens as shown in Figure 3.5b. The strains were measured using a Data Acquisition device (DAQ) NI 9236 (National Instruments, Austin, TX, USA) and were processed using a custom Lab-view code (National Instruments, Austin, TX, USA). Five specimens of each orientation were fabricated and tested. The strains in the longitudinal direction were validated using a laser extensometer as shown in the Figure 3.5a.

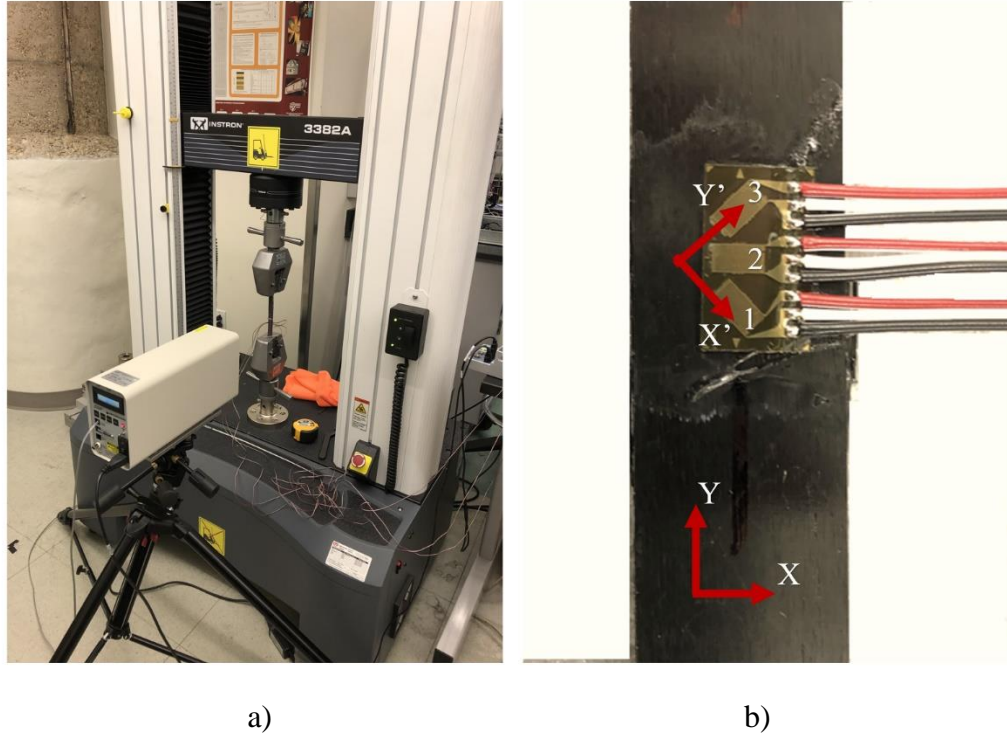


Figure 3.5. a) Test setup for characterization of carbon fiber adherends b) Strain gauges mounted on carbon fiber test samples

The machine load data, laser extensometer data and the data from the strain gauges were analyzed using a custom MATLAB code. The measured strains along the strain gauge axes  $X'-Y'$ , as shown in Figure 3.5 b, were calculated from the recorded measured strains. The strain along any direction ' $\theta$ ', on the  $X'-Y'$  plane was calculated using strain transformation equations as given in Equation 1 [1].

$$\varepsilon = \frac{1}{2}(\varepsilon_{X'} + \varepsilon_{Y'}) + \frac{1}{2}(\varepsilon_{X'} - \varepsilon_{Y'}) \cos(2\theta) + \varepsilon_{XY'} \sin(2\theta) \quad (3.1)$$

where:  $\varepsilon$  – Strain along a given angle  $\theta$

$\theta = 0^\circ$  for strain gauge 1

$45^\circ$  for strain gauge 2

$90^\circ$  for strain gauge 3

Substituting these values of  $\theta$  for strain gauges 1,2 and 3 respectively in Equation 3.1, we get a relationship between the strains along the  $X'Y'$  axes,  $\varepsilon_X, \varepsilon_Y, \varepsilon_{XY}$ , and the strains measured by the strain gauges,  $\varepsilon_a, \varepsilon_b, \varepsilon_c$  given as

$$\begin{aligned}\varepsilon_{X'} &= \varepsilon_a \\ \varepsilon_{Y'} &= \varepsilon_b \\ \varepsilon_{XY'} &= \varepsilon_b - \frac{\varepsilon_a + \varepsilon_c}{2}\end{aligned}\quad (3.2)$$

The strains along the loading axis X-Y were calculated by rotating by an angle  $\alpha = 45^\circ$ , the strains calculated along  $X'-Y'$  using Equation 3.2, to the X-Y coordinate axes as given in Equation 3.3 [1].

$$\begin{aligned}\varepsilon_X &= \varepsilon_{X'} \cos^2(\alpha) + \varepsilon_{Y'} \sin^2(\alpha) - 2\varepsilon_{XY'} \sin(\alpha) \cos(\alpha) \\ \varepsilon_Y &= \varepsilon_{X'} \sin^2(\alpha) + \varepsilon_{Y'} \cos^2(\alpha) + 2\varepsilon_{XY'} \sin(\alpha) \cos(\alpha) \\ \varepsilon_{XY} &= (\varepsilon_{X'} - \varepsilon_{Y'}) \sin(\alpha) \cos(\alpha) + \varepsilon_{XY'} (\cos^2(\alpha) - \sin^2(\alpha))\end{aligned}\quad (3.3)$$

The engineering stress was obtained by dividing the instantaneous load ( $F_t$ ) and the cross-sectional area of the bars ( $A$ ). The strain from the laser extensometer was calculated by dividing the extension measured by the extensometer with gauge length. The elastic moduli ( $E_1$  and  $E_2$ ) were calculated by measuring the slope the engineering stress-strain curve. The shear modulus was calculated by measuring the slope of the shear stress-strain curve. The shear stress was obtained by resolving the longitudinal stress along the  $45^\circ$  plane w.r.t to the loading axis coordinate system as shown in Equation 3.4. [108]

$$\tau_{XY} = \frac{F_t}{A} \cos(45) \sin(45) \quad (3.4)$$

where:  $F_t$  – Longitudinal tensile load (N)  
 $A$  – Cross- sectional area of the bar ( $\text{mm}^2$ )

The shear strain was calculated by rotating the loading axis coordinate system by 45° using Equation 3 for calculating the shear strain from the individual strain components. The Poisson's ratio  $\nu_{XY}$  was calculated by dividing the longitudinal strain by the transverse strain [108] as shown in Equation 3.5

$$\nu_{XY} = \frac{\varepsilon_Y}{\varepsilon_X} \quad (3.5)$$

*3.1.3.1.2 Compression Testing.* Compression tests were performed using a Test Resources tensile testing machine (Shakopee, MN, USA) on the 0° and 90° orientation specimens as per SRM IR-94 standard [27]. A compression test fixture conforming to SRM IR-94 standard was used. The specimens were prepared as per the specifications prescribed by the standards as shown in Figure 3.6.

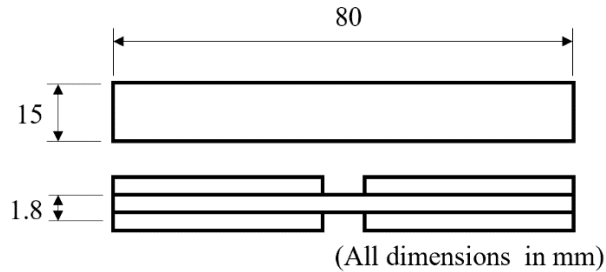


Figure 3.6. Geometry of Compressive test specimen [27]

The compression fixture was placed between the compression platens as shown in Figure 3.7.

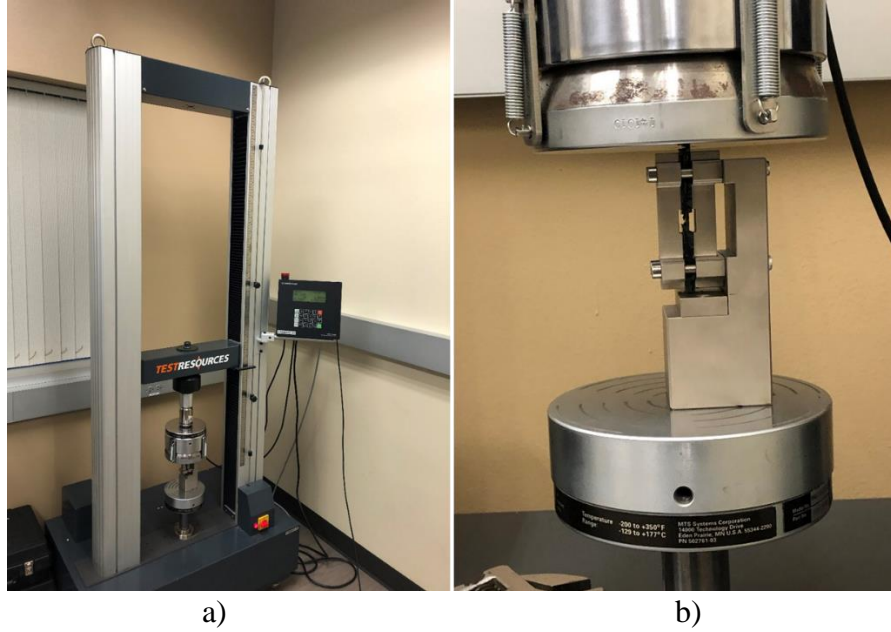


Figure 3.7. a) Test setup for compression testing b) Compression test fixture mounted on platens attached to the universal testing machine

The platens were attached to a Test Resources universal tensile testing machine, with a load cell rating of 50 KN. The compression test was performed at a displacement-controlled rate of 1mm/min. The load at failure  $F_c$  of the specimen was recorded and the compressive strength was calculated using Equation 3.6 [27].

$$X_c, Y_c = \frac{F_c}{A} \quad (3.6)$$

where:  $X_c, Y_c$  – Compressive strength in  $0^\circ$  and  $90^\circ$  configurations ( $\text{N}/\text{mm}^2$ )  
 $F_c$  – Failure Load (N)  
 $A$  – Cross-sectional area of the bar ( $\text{mm}^2$ )

*3.1.3.1.3 Short Beam Testing.* Short-beam test was performed to measure the inter-laminar shear strength of the composite adherends. Short beam tests were performed in accordance with ASTM D2344 standard [28]. Specimens were prepared as per the standard. The tests were performed on a Test Resources tensile testing machine having a

load cell of 4448.2 N, at a displacement-controlled loading rate of 1mm/min. A test fixture conforming to ASTM D2344 standards was used as shown in Figure 3.8. The interlaminar failure strength ( $S_{XZ}$ ) was calculated using Equation 3.7 [28].

$$S_{XZ} = 0.75 \frac{F_S}{bh} \quad (3.7)$$

where:  $F_S$  – Failure Load (N)  
 $b$  – Width of test specimen (mm)  
 $h$  – Thickness of test specimen (mm)

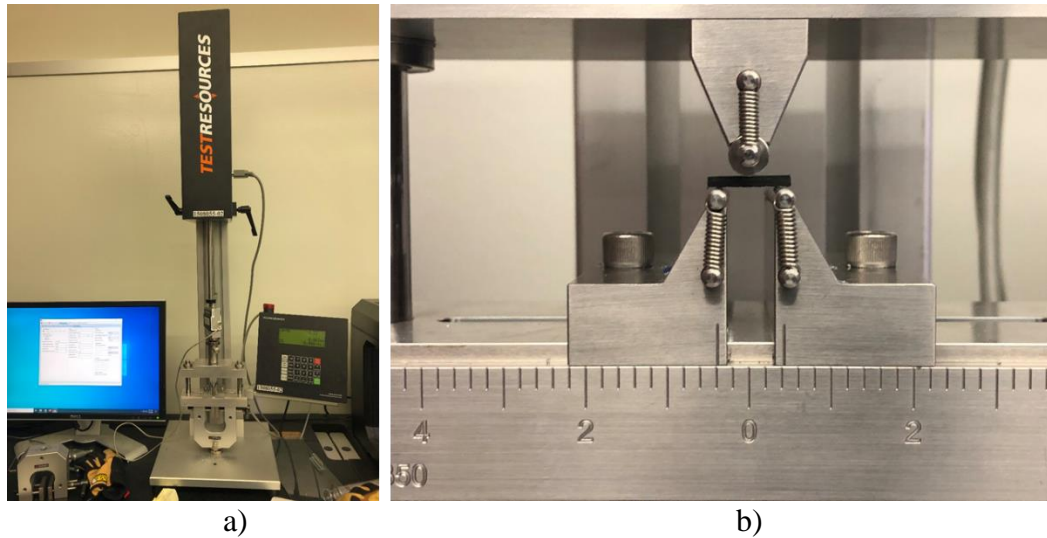


Figure 3.8. a) Test setup for short beam test. b) Short beam test fixture

The elastic properties for a unidirectional  $0^\circ$  laminate, calculated using the above methods have been tabulated in Table 3.1. Directions  $X$  and  $Y$  are the in-plane directions, while  $Z$  is the out of plane direction. Since unidirectional composites are considered transversely isotropic, the values of stiffness along  $Y$  and  $Z$  axes, Poisson's ratios in  $XY$  and  $XZ$  planes, and the shear moduli in the  $XY$  and  $XZ$  planes are considered identical.

Table 3.1. Measured Elastic properties of carbon fiber adherends.

$E_x$ (GPa)	$E_y = E_z$ (GPa)	$\nu_{xy} = \nu_{xz}$	$G_{xy} = G_{xz}$ (GPa)
$126.99 \pm 9.07$	$8.89 \pm 0.39$	$0.28 \pm 0.04$	$3.93 \pm 0.99$

The strengths of the carbon fiber adherends measured from the tests described in this section are summarized in Table 3.2. The respective tensile strengths in X, Y and Z directions are represented as  $X_t$ ,  $Y_t$  and  $Z_t$ . The respective compressive strengths in X, Y and Z directions are represented as  $X_c$ ,  $Y_c$  and  $Z_c$ . The interlaminar shear strength of the composite ply is represented as  $S_{xz}$ . The experimental strength and modulus data has been listed in detail in Appendix A.

Table 3.2. Measured strengths of carbon fiber adherends.

$X_t$ (MPa)	$Y_t = Z_t$ (MPa)	$X_c$ (MPa)	$Y_c = Z_c$ (MPa)	$S_{xz}$ (MPa)
$1368.75 \pm 0.21$	$17.96 \pm 1.51$	$311.26 \pm 57.61$	$70.27 \pm 11.18$	$57.81 \pm 4.75$

### 3.1.3.2 Hysol 9309 NA Adhesive Characterization

Hysol 9309 NA is a two-part epoxy adhesive [106]. The tensile stress-strain properties of Hysol 9309 NA were measured to incorporate the non-linear behavior of the adhesive in the finite element model. Tensile test bars in compliance with the ASTM D638 [109] were fabricated using a mold to cast the specimen as shown in Figure 3.9. A planetary centrifugal mixer, manufactured by Thinky (Thinky USA, Laguna Hills, CA), was used to mix and remove air bubbles from the adhesive. The adhesive was mixed in a cup which was rotated at 2000 rpm in a vacuum of 2.5 KPa. The mixed adhesive was poured into the molds and allowed to cure at room temperature for 24 hours and subsequently heat treated at 82°C for 1 hour, following the same procedure used in

fabricating the bonded joint specimen described in Section 3.1.2. The cured bars were machined on a vertical milling machine to remove flash and to obtain a flat surface for gripping on the tensile testing machine. Five adhesive test specimens were tested for strength using Instron 3382A tensile testing machine, having a load cell of 100 KN, by loading at a rate of 0.05 mm/min, as shown in Figure 3.10. The longitudinal extension was measured using a laser extensometer. The Elastic modulus was calculated by measuring the slope of the tensile stress-strain curve. The failure strength and the elastic modulus are summarized in Table 3.3. The experimental strength and modulus data has been listed in detail in Appendix A.

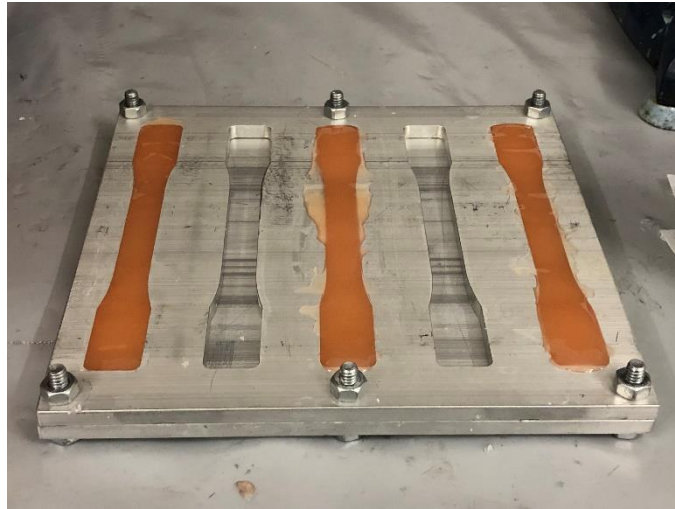


Figure 3.9. Mold used for casting adhesive tensile test bars.

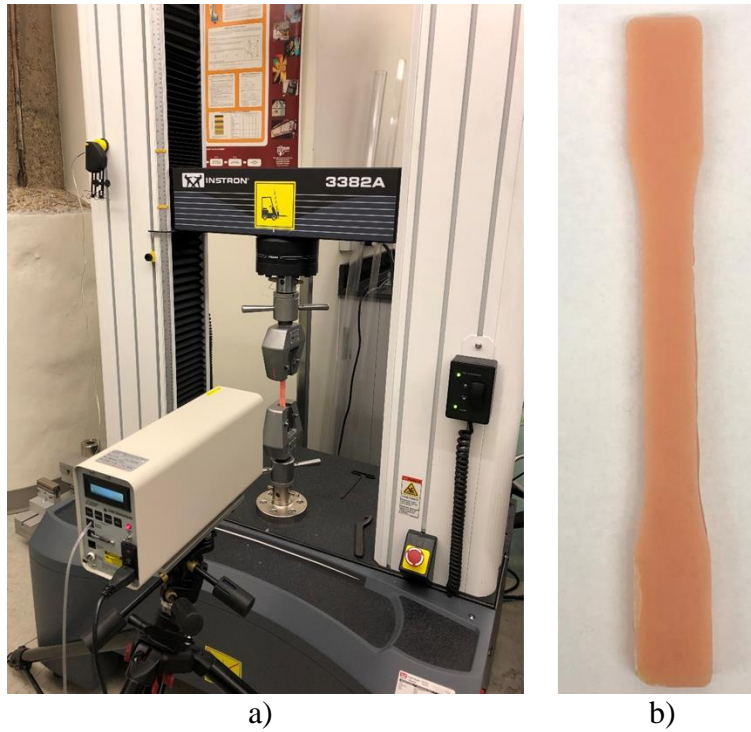


Figure 3.10. a) Test setup for characterization of Hysol 9309 NA adhesive. b) Cured test bars

Table 3.3. Measured stiffness and strength of Hysol 9309 NA adhesive

<b>E (MPa)</b>	<b><math>\sigma_{max}</math> (MPa)</b>
2109.75 ± 194.13	39.04 ± 0.65

### 3.2 Numerical Modeling

#### 3.2.1 Model Description

Finite Element analysis of single lap joints was performed using “ABAQUS CAE” (3DS Dassault systems, Massachusetts, USA) general purpose finite element software. Geometrical non-linearity was incorporated during analysis since the flexibility of joints causes large displacements and rotations in the joint, which influences the equilibrium conditions [24]. The dimensions and boundary conditions applied on the

single lap joint model are shown in Figure 3.11. The adhesive thickness is designated as  $t_a$  while  $u_x$  designated the applied displacement at the right end of the overlap.

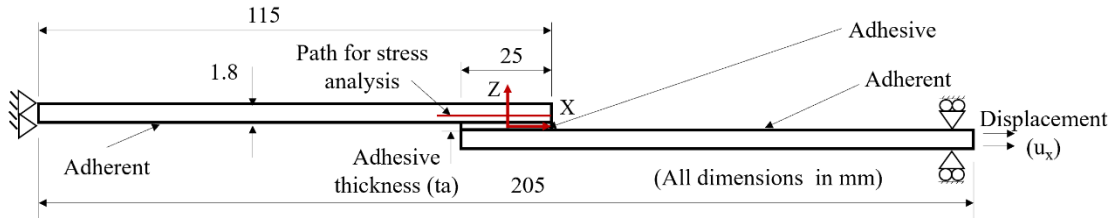


Figure 3.11. Simulation model dimensions for single lap joint with boundary conditions

The left end of the model was fixed with all degrees of freedom set to zero as shown in Figure 3.11, while the right end was constrained in the direction normal to the applied load. A static, displacement-controlled simulation was used for each analysis since all experiments performed were quasi-static and displacement controlled. ABAQUS uses a Newton's iterative numerical method for solving geometrically non-linear problems as it gives better convergence [105]. A total time of 1 unit was chosen for load application in the simulation, which was divided into 10-time iterations of 0.1 units each.

A user material subroutine (UMAT) was employed to calculate a solution variable for assessing the failure criteria of the composite. The mechanical properties of the adherend are passed to UMAT using the 'Materials' keyword in ABAQUS. Stiffness matrix parameters were calculated using the stiffness parameters measured during material characterization as summarized in Table 3.1. The FORTRAN code shown in Appendix. C, was used to calculate the stress and failure criteria at each Gauss point within the UMAT, using the FORTRAN statement in Equation 3.8 as

$$\text{STRESS}(I)=\text{STRESS}(I)+\text{DDSDDE}(I,J)*\text{DSTRAN}(J) \quad (3.8)$$

where:  $\text{STRESS}(I) = I^{\text{th}}$  Stress component for the next time increment  
 $\text{DSTRAN}(J) = J^{\text{th}}$  strain increment component from the beginning of the current time increment  
 $\text{DSDDE}(I,J) =$  Jacobian matrix of the element

Two dimensional (2D) simulations were performed using ABAQUS 2D rectangular plane strain element type, CPE4 for both the adherend and the adhesive. The plane strain element has been used by previous researchers since the thickness of the adherend and the adhesive are small in comparison with the width of the joint [36]. A graded meshing approach was used with a finer mesh having a size of 0.02mm in the region of overlap, increasing to 0.2 mm towards the ends of the joint, as shown in Figure 3.12.

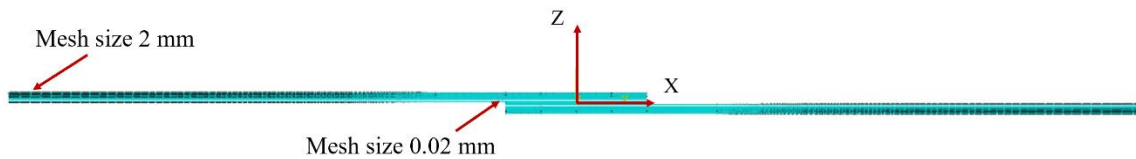


Figure 3.12. Mesh details for a 2D single lap joint model

A convergence study was performed with meshes having minimum element sizes of 0.02 mm, 0.01 mm and 0.005 mm in the finer mesh region at the bond overlap. The boundary conditions applied are shown in the Figure 3.13. Von Mises stresses were plotted along the path passing through the middle of the first ply as shown in Figure 3.13.

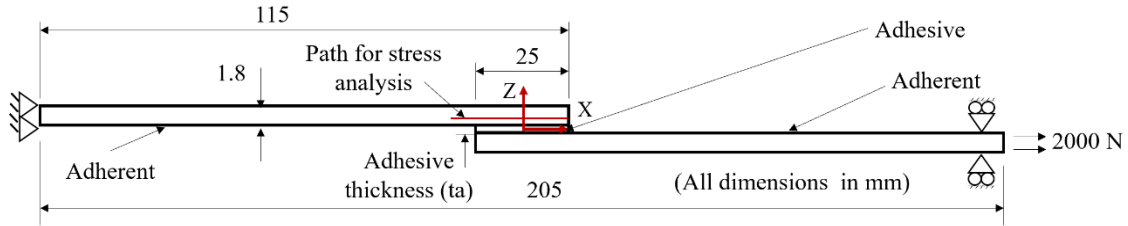


Figure 3.13. Schematic of load and boundary conditions and path for stress analysis

The plots of Von Mises stress for various mesh sizes appear in Figure 3.14. The stress curves overlap while the maximum Von-Mises stress increases by approximately 0.02% when the mesh size decreases from 0.02 mm to 0.005 mm. Hence the mesh size of 0.02 mm was chosen so as to reduce the computation time.

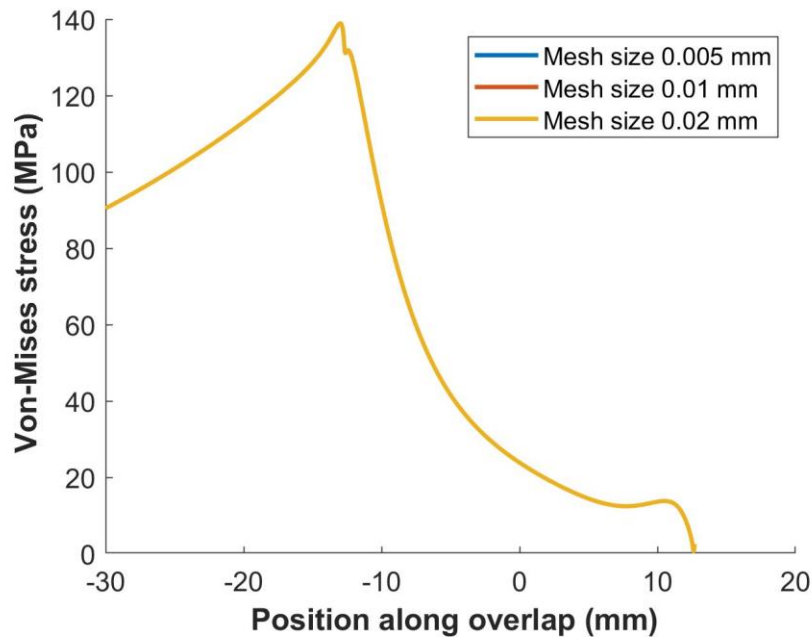


Figure 3.14. Comparison of Von-Mises stress for various mesh sizes for a 2D model

For 3D analysis used in Chapter Five, ABAQUS 3D continuum element type: C3D8 were used. A graded meshing approach was used with a finer mesh having size of 0.02mm in the region of overlap, increasing to 0.2 mm towards the ends of the joint. A

convergence study was also performed for the 3D FE model using models with different meshes having elements with minimum sizes of 0.05 mm, 0.03 mm and 0.01 mm, near the overlap. The Von Mises stresses were plotted along the path passing through the mid-plane of the first ply as shown in Figure 3.13. The plots of Von-Mises stresses for the various mesh sizes, shown in Figure 3.15, indicate no significant change in the maximum Von-Mises stresses. Von-Mises stresses increase by approximately 5% when the mesh size decreases from 0.05 to 0.01 mm. The mesh size of 0.05 mm was chosen to reduce the computation time.

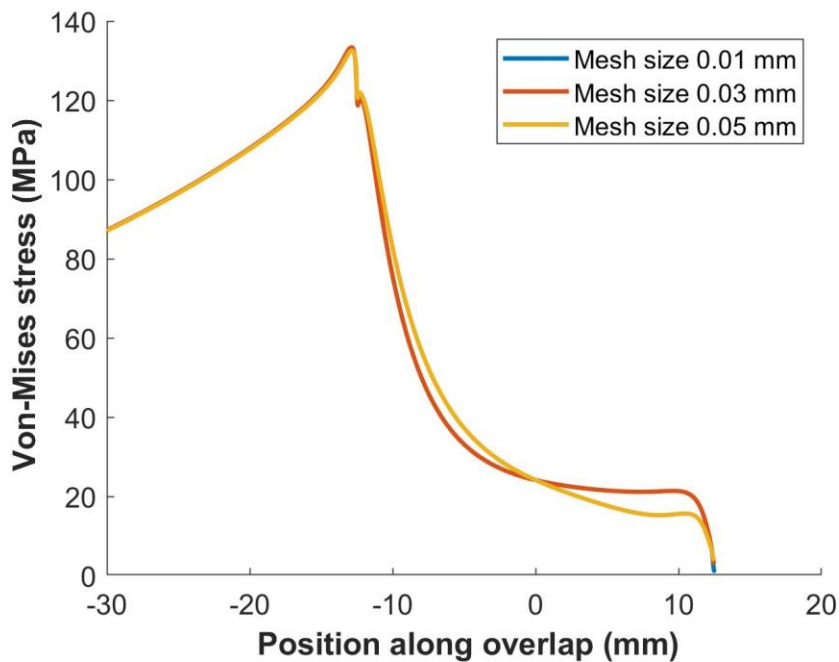


Figure 3.15. Comparison of Von-Mises stress for various mesh sizes for a 3D model

The failure loads for all of the finite element simulation presented below were calculated using the “Critical Zone method” as described in Section 4.1.3 applying the failure criteria described in Section 2.3.2.

### 3.2.2 Verification of Finite Element Model

The Finite Element model was verified by comparing computed outputs to a load displacement curve from an experimental test. A single lap joint having a uniform bond line thickness was tested for failure. The test was performed on Instron 3382A tensile testing machine, having a load cell of 100 KN, by loading at an extension rate of 0.05 mm/min. The displacement of the test specimen was measured using a laser extensometer. A tab made of the same material as the adherend was bonded to one of the adherends as shown in Figure 3.16. to ensure the reflective strips were positioned in the same vertical plane to prevent errors in measurement of displacement. The strips were placed such that they were 44mm on each side of the center of the joint, as shown in Figure 3.16.

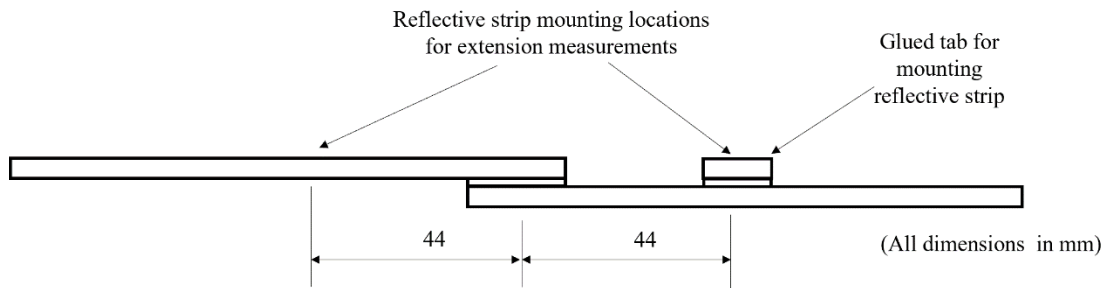


Figure 3.16. Geometry of test specimen used for FE model verification.

The load-displacement curves obtained from the experiments are shown in Figure 3.17.

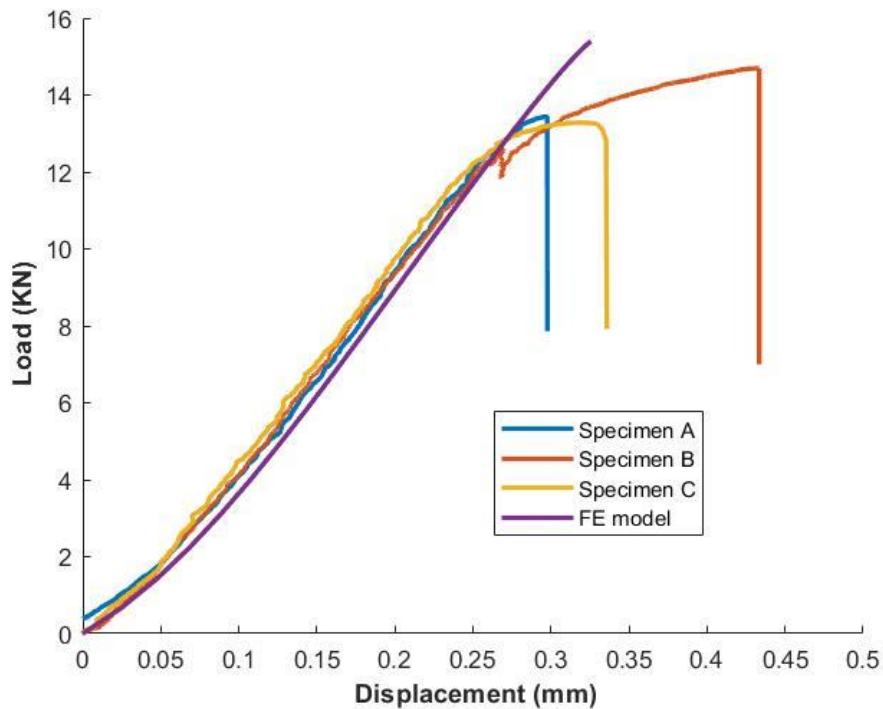


Figure 3.17. Comparison of Load-displacement curves obtained experimentally and using FE analysis.

The laser extensometer measured the relative displacement between the two reflective strips to calculate the overall displacement of the joint. The Finite Element model as described in Section 3.2.1 was analyzed and the load-displacement curve was plotted as shown in Figure 3.17. The displacement was measured at 44 mm each from the center of the joint, like the test specimen and the relative displacement was calculated. The experimental load-displacement curves matched closely with that of the FE model. The difference between the slopes of the load-displacement curves measured experimentally and calculated using the FE model was approximately 5%.

## CHAPTER FOUR

### Effect of Adhesive Thickness Variations

Adhesive bond line thickness has a significant effect on the strength of bonded joints. Maintaining a uniform bond line thickness has been a difficult problem in industrial applications, for instance on marine structures [110]. A value for bond line thickness for typical applications is around approximately 0.2 mm, which has been shown to give maximum bond strength compared with higher and lower bond thickness than 0.2 mm [31]. For example, when metallic adherends are used, the bond strength increases, reaches a maximum value and then decreases as thickness increases when a ductile adhesive is employed. Conversely, the failure load only decreases with increasing bond line thickness when brittle adhesives are used [21]. For composite adherends, the failure loads were found to decrease with increase in bond line thickness [39]. When the bond line has a non-uniform thickness, Kim [22] found that the stresses in the adhesive increased as the ratio of the minimum to the maximum thickness increased. However, the effect of a variation in thickness along the bond line, on bond joint failure strength, has not been addressed in the literature.

A variation in bond line thickness may occur due to an improper fabrication process, improper fixture design or irregular thickness of the adherends being joined. Fabrication errors may occur because of improper selection of thickness spacers. Improper fixture design can also produce a non-uniform pressure distribution across the bonded region. Airframe structures such as fuselages in large aircraft are composed of

curved sections joined in lap joint configuration [111]. Errors in fabrication of aircraft structures can cause a misalignment of the adherend structural members being joined causing a misalignment such that appearing in Figure 4.1. These misalignments may occur due to an eccentricity between the curved sections joined which can produce a variation in bond line thickness.

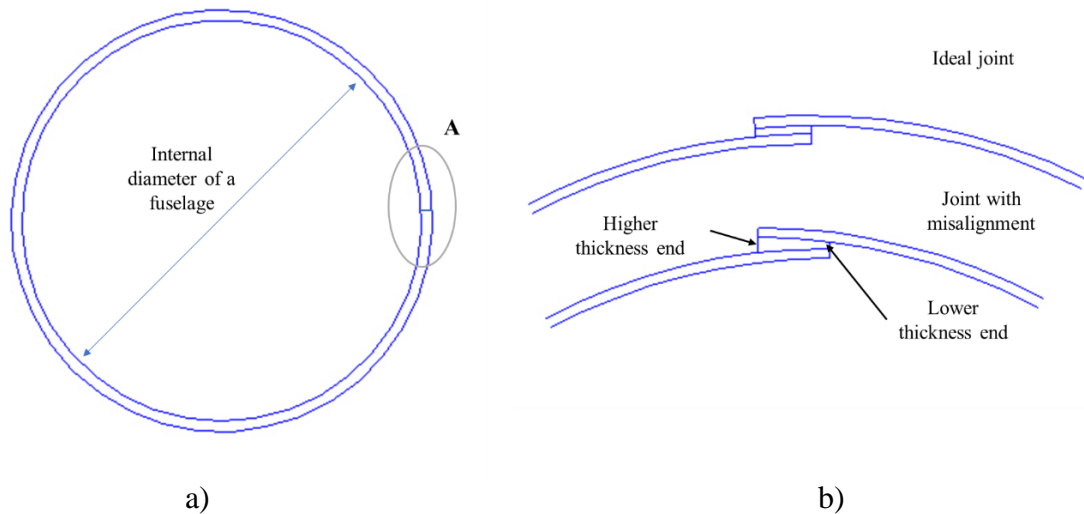


Figure 4.1 a) A fuselage of a typical large aircraft composed of joined sections.  
 b) Magnified view of one of the joined sections (A) with and without misalignment

The effect of bond line thickness variation due to misalignment of adherends on bond strength integrity is the focus in this chapter. Liu [112] showed that for bonded structures having a larger radii of curvature (greater than 2000 mm), such as those seen in commercial aircraft, the curvature can be neglected when considering the load bearing capacity and stress distribution, making the study of the single lap joint applicable to this more complex structure. The first part of this study deals with the case of a uniform bond line thickness joint and establishes a suitable failure criterion for predicting failure loads.

The method is then applied further to a single lap joint with linearly varying bond line thickness due to the misalignment of adherends.

#### *4.1 Study on a Constant Bond Line Thickness*

##### *4.1.1 Experimental Details*

Spacers made from metallic strips of four different thicknesses were used for achieving the target bond-line thickness. The target thickness for each experiment set has been listed in Table 4.1. The test coupons were bonded using the procedure described in Section 3.1.2. The bond-line thickness of the bonded specimens was measured using the Keyence VR3100 3D microscope (Keyence corporation, Itasca, Illinois, USA) as shown in Figure 3.3 in Section 3.1.2. Images of the bond line showed that there was a deviation in thickness from the target values in the specimens. The average bond line thickness was measured and recorded and was used for further analysis as shown in Figure 4.2. Lap shear tests were performed on all the test specimens on the Instron 3382A tensile testing machine (Instron, Massachusetts, USA), having a load cell rating of 100 KN, at displacement-controlled loading rate of 0.05 mm/min as described in Section 3.1.2.

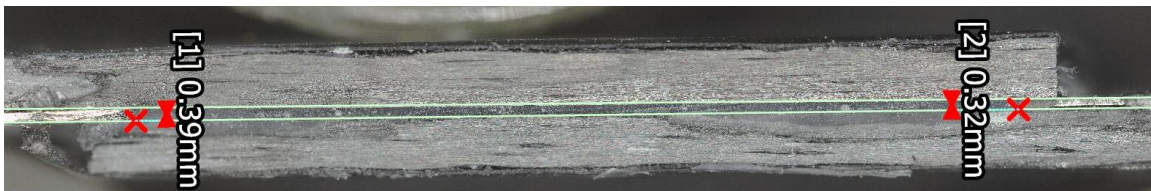


Figure 4.2. Bond line thickness measurement using a Keyence microscope.

Table 4. 1. Experimental plan for studying thickness variations.

<b>Trial</b>	<b>Minimum Thickness (mm)</b>	<b>Maximum Thickness (mm)</b>
<b>A</b>	0.25	0.25
<b>B</b>	0.5	0.5
<b>C</b>	0.75	0.75
<b>D</b>	1.0	1.0

All of the specimens exhibited a light fiber tear failure in the first ply closest to the bond line as shown in Figure 4.3.



Figure 4.3. Failed surface of a bond with uniform thickness

The failure load as a function of the average bond line thickness is shown in Figure 4.4. A second order polynomial appearing in Equation 4.1, was fit using MATLAB function “Polyfit” to obtain a correlation coefficient ( $R^2$ ) of 0.9582, which gave the best fit among linear and exponential fits. The correlation coefficient for linear and exponential fit are 0.9371 and 0.9501 respectively. Higher degree curves give higher values for the correlation coefficient but distorts the curve, which does not reflect a practical outcome.

The failure load decreases with an increasing bond line thickness which is similar to the results obtained by previous researchers [20,31,39]. The equation of the curve fit is

$$P = 6.26t^2 - 16.56t + 19.23 \quad (4.1)$$

where:  $P$  = Failure load (N)

$t$  = Bond line thickness

The failure strength decreases by approximately 46%, as per Equation 4.1, when the bond line thickness increases from 0.25 mm to 1.2 mm. A detailed discussion of the stress states and the failure prediction techniques used to predict the failure loads are presented in Section 4.1.2.

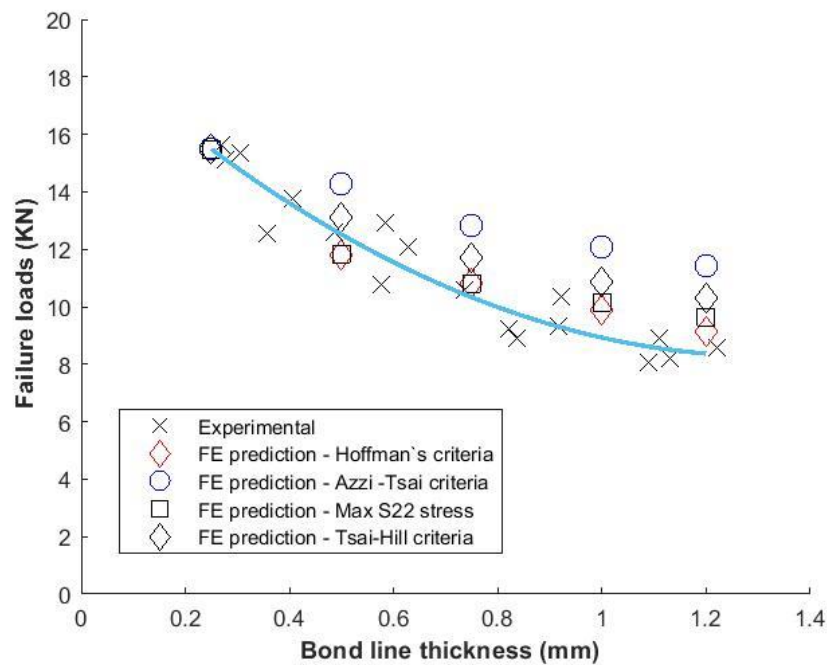


Figure 4.4. Failure loads for various bond line thickness.

#### 4.1.3 Numerical Analysis

The Finite Element model was developed as described in Chapter Three, Section 3.2.1. The Critical Zone Method, as described in Section 2.3.3, was used for prediction of strength. The failure criteria namely maximum stress, Yamada Sun, Azzi-Tsai Norris, Hoffman`s and Tsai Hill criteria, were evaluated in a ABAQUS CAE (3DS Dassault systems, Massachusetts, USA) UMAT code using the failure criterion equations as described in Section 2.3.3. A unique Solution Dependent Variable (SDV) was assigned to the output quantity of each criterion considered in this research. The contour graph of the Hoffman`s criterion solution variable appears in the display field as shown in Figure 4.5.

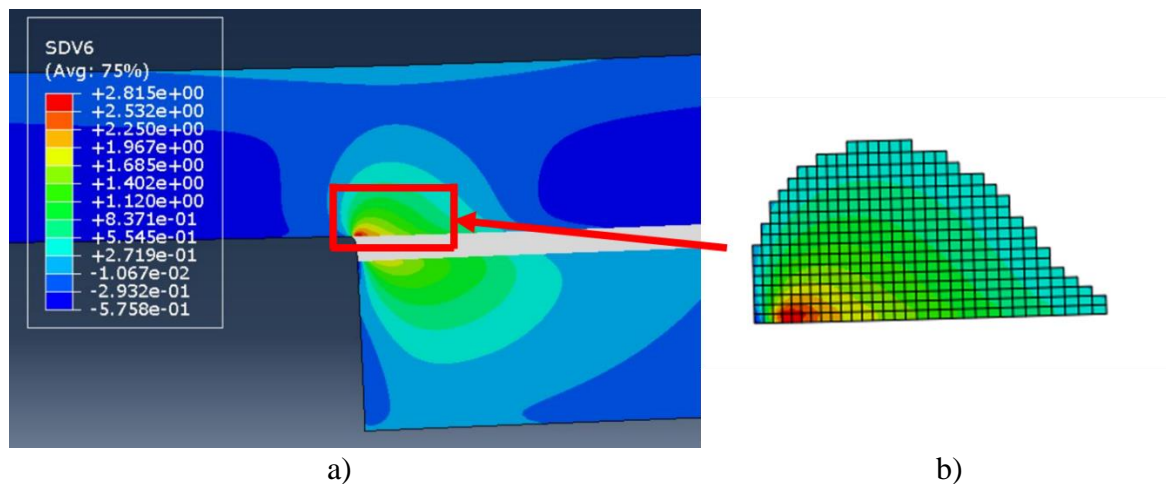


Figure 4.5. a) Contour plot of the solution dependent variable corresponding to Hoffman`s criteria b) Volume of critical zone measured in ABAQUS CAE

The critical zone volume was measured for a single lap joint configuration of 0.25 mm thickness, having a failure load of 15.48 KN, as determined from the curve fit in Figure 4.4. The reference volume is calculated to be 5.85 mm<sup>3</sup>. The elements which attained a SDV value equal to or greater than 1, appear in the display using the “Display group” option. The volume of the displayed elements was measured using the ABAQUS

CAE “Mass Properties” option under the “Tools” tab. The Reaction force at the fixed constraint end of the model was plotted as a function of model displacement. A representative figure showing the load-displacement curve plotted from the results of a model with 0.25 mm bond line thickness is shown in Figure 4.6.

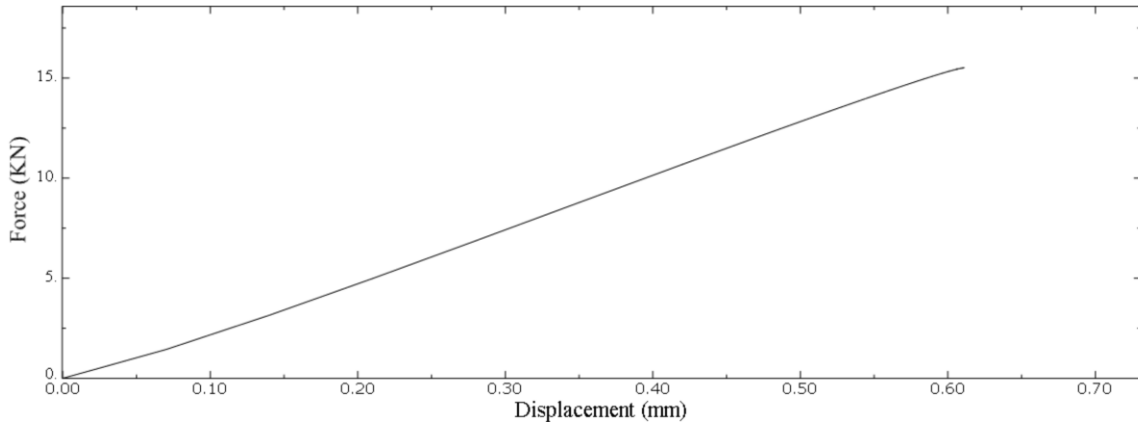


Figure 4.6. Reaction force as a function of displacement plotted in ABAQUS CAE for a bond line thickness of 0.25 mm.

The reference volumes calculated, applying the various criteria are listed in Table 4.2.

Table 4.2. Volume of critical zone using various failure criteria.

<b>Criteria Used</b>	<b>Reference volume (mm<sup>3</sup>)</b>
<b>Maximum Longitudinal Stress</b>	--
<b>Maximum Transverse Stress</b>	1.27e+01
<b>Maximum Shear Stress</b>	--
<b>Yamada – Sun criteria</b>	1.34e+01
<b>Azzi-Tsai criteria</b>	3.32e+01
<b>Hoffman`s criteria</b>	5.86e+00
<b>Tsai-Hill criteria</b>	1.67e+01

The SDVs for maximum longitudinal stress criteria and the maximum shear stress criteria did not attain the value of 1 during the analysis since the respective stresses never

reached the experimentally measured failure values of the composite, as listed in Section 3.1.3.1. Hence their respective reference volumes could not be found.

The failure loads for the bond line thicknesses of 0.5, 0.75, 1.0 and 1.2 mm were predicted by reversing the procedure for calculating the reference volume. The elements whose SDVs equaled or exceeded the value of 1, were displayed, and their volumes measured using the same procedure described above. The reaction force at the fixed constraint end of the model was plotted as function of displacement of the model at its free end, for each bond line thickness. The reaction force corresponding to the displacement at which the volume measured equaled the reference volume was noted as the failure load for each bond line thickness. The failure loads calculated using this method applying the various criteria is shown in Table 4.3.

The predicted loads using the Critical Zone method, applying the various criteria compared with failure loads as determined from the experimental trend given by Equation 4.2 are shown in Table 4.3. The model with the bond line thickness 0.25 mm was used as a reference.

The absolute percentage error was calculated for each bond line thickness listed in Table 4.3 by comparing the respective failure loads with values taken from the experimental trend curve fit in Equation 4.1. The average of all the percentage errors was calculated across the different bond line thickness for each of the criterion considered in Table 4.3. The average absolute percentage errors calculated are 9.95%, 10.9%, 27.5%, 7.74%, and 15.7% for Maximum Transverse stress, Yamada-Sun, Azzi-Tsai Norris, Hoffman`s and Tsai-Hill criteria respectively. Based on this result, the Hoffman`s criteria is better suited to predict the failure loads of the single lap bonded joints considered in

this study. The reason for this may be the fact that the composite adherend used in this study is significantly weak in the out of plane (Z) direction. The emphasis on the out of plane stresses correlates with the size of the critical zone as shown in Table 4.2. The Hoffman`s criterion has the least critical volume while the Azzi-Tsai criterion has the largest.

Table 4.3. Comparison of predicted failure loads with experimental trend curve fit (Equation 4.1)

<b>Criterion used</b>	<b>Bond line thickness 0.5 mm (KN)</b>	<b>Bond line thickness 0.75 mm (KN)</b>	<b>Bond line thickness 1.0 mm (KN)</b>	<b>Bond line thickness 1.2 mm (KN)</b>	<b>Average absolute percentage error  (%)</b>
Maximum Transverse Stress	11.84	10.82	10.17	9.65	9.95
Yamada-Sun	12.06	10.97	10.32	9.86	10.9
Azzi-Tsai Norris	14.27	12.84	12.07	11.41	27.5
Hoffman`s	11.79	10.84	9.87	9.15	7.74
Tsai-Hill	13.11	11.71	10.86	10.3	15.7
Experimental	12.52	10.32	8.92	8.36	--

Stresses in the first ply of the adherent adjacent to the bond line were evaluated to better understand the effect of bond line thickness on bond joint integrity. A FE model was created to evaluate the stresses with a fine mesh having elements of the size of 0.02 mm near the ends of the overlap, which was graded to a coarser mesh with 2 mm elements towards the ends, as shown in Figure 4.7.

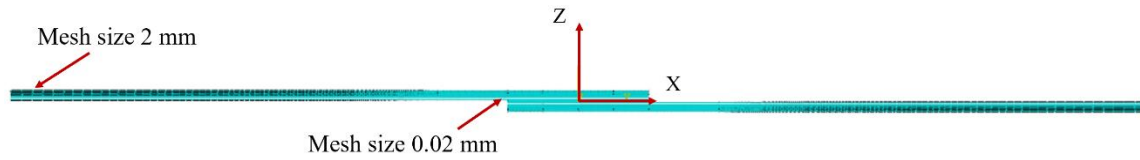


Figure 4.7. Mesh details of the single lap joint model used for stress analysis.

The FE model was loaded axially to 2000 N at the free end of the model as shown in Figure 4.8. The adhesive thickness is designated as  $t_a$ . The ‘Path’ option was used to define a path along the position corresponding to mid-thickness of the first ply adjacent to the bond line as shown in Figure 4.8. The ply adjacent to the bond line was chosen because failure in all test specimens were observed to be within the first ply closest to the bond line as shown in Figure 4.3. The position at the first laminate mid-plane was chosen to mitigate the effect of the finite element singularities which occur at the corners of single lap bonded joints [24].

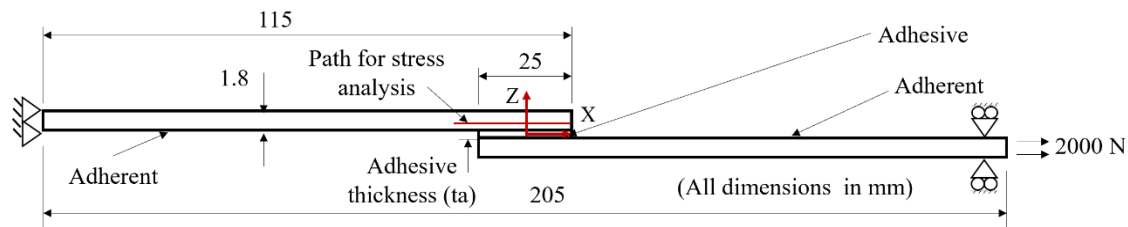


Figure 4.8. Path prescribed along the mid-thickness of the first ply for stress measurements.

The shear stress and peel stress plotted as a function of length along the bond line appear in Figure 4.9. and Figure 4.10. The geometric center of the single lap joint configuration located at the middle of the adhesive layer was selected as the origin as shown in Figure 4.8.

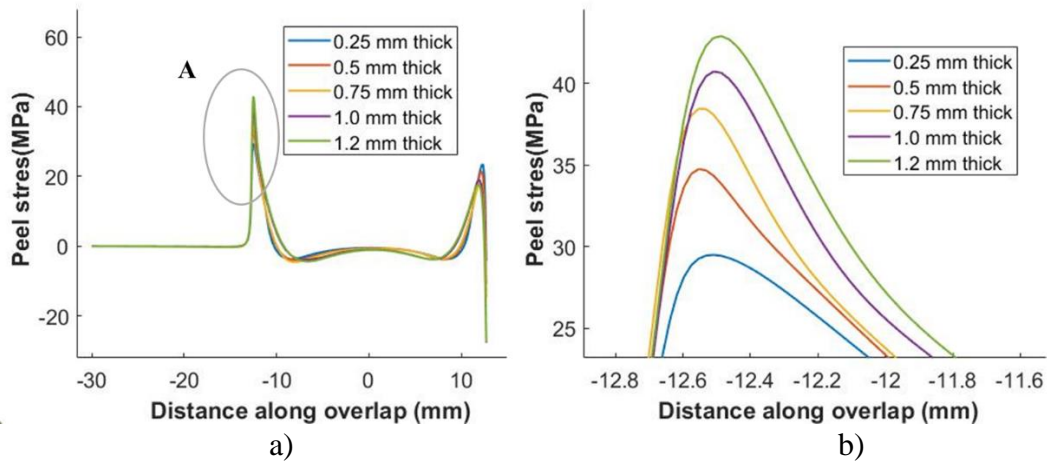


Figure 4.9. a) Peel stress distribution along middle of first ply closest to the bond line  
 b) Magnified view of detail 'A'

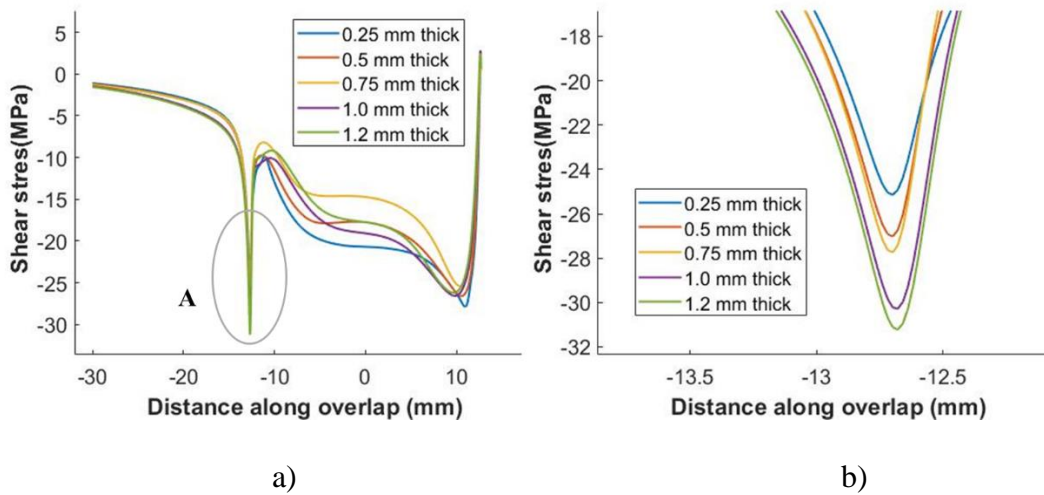


Figure 4.10. a) Shear stress distribution along middle of first ply closest to the bond line  
 b) Magnified view of detail 'A'

The comparison of maximum shear and peel stress values for various bond line thickness is plotted in Figure 4.11.

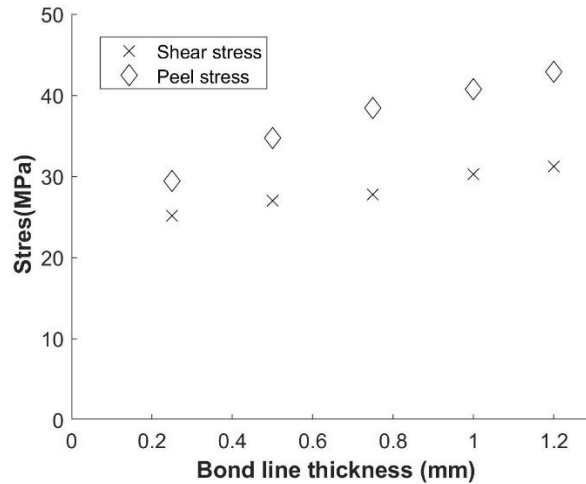


Figure 4.11. Comparison of maximum shear and peel stress for different bond line thickness

The peel and shear stresses were plotted along the path defined in Figure 4.8. The positions shown in the plots are with reference to the origin defined at the center of the joint as shown in Figure 4.8. The peel and the shear stresses peak at  $x = -12.5$  mm which is located at the end of the overlap. The stresses also peak at the opposite end of the overlap i.e., at  $x = 12.5$  mm, but the peak is smaller in comparison with the peak at  $x = -12.5$  mm. The peel stress and shear stress increase with bond line thickness as shown in Figure 4.9. and Figure 4.10. The peel stresses increase from 29.49 MPa to 42.89 MPa, by approximately 45% as the bond line thickness increases from 0.25 to 1.2 mm, while the shear stresses increase from 25.15 MPa to 31.22 MPa by approximately 24% over the same thickness range. Laminated composite adherends are typically significantly weaker in the out of plane and transverse direction in comparison with longitudinal direction [113]. The CFRP composite adherend used in the current study also exhibits such a characteristic as shown by the strength properties listed in Table 3.2 in Section 3.1.3. This increase in the peel and shear stresses combined with a lower out of plane strength,

explains the reduction of strength of the lap joint with an increase in bond line thickness. Higher stresses are produced at the edges of a single lap joint due to bending moments produced from the eccentricity in the load path [6]. Gleich, et.al [31] showed that the when the peel and shear stresses in the vicinity of the corner of the adhesive-adherend interface, increase with an increase in bond line thickness. These effects also propagate to the surrounding adherend material resulting in an increase in peel and shear stresses in the adherends [39].

#### 4.2 Study on Linearly Varying Bond Line Thickness Due to Adherend Misalignment

##### 4.2.1 Experimental Details

Test coupons with a linearly varying bond line thickness were fabricated by placing dissimilar thickness spacers at each end of the single lap joint to create a misalignment in the adherends. The same fabrication procedure as detailed in Section 3.1.2, was applied for fabricating the test coupons. The bond line thickness was measured using the Keyence VR3100 3D microscope (Keyence corporation, Itasca, Illinois, USA). Figure 4.12. shows an image processed in the Keyence software.

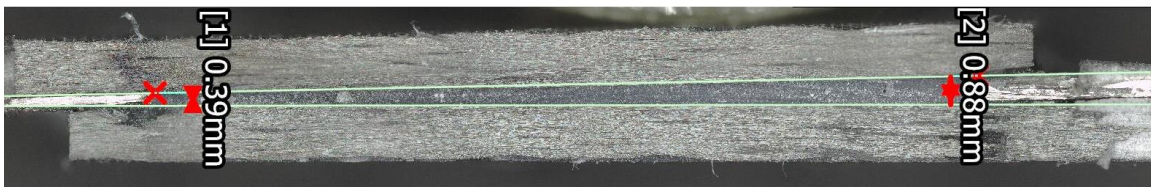


Figure 4.12. Bond line thickness measurement using a Keyence microscope.

Table 4.4. shows the target thickness values for the study of bond joints with varying thickness.

Table 4.4. Experimental plan for study of varying thickness

<b>Trial</b>	<b>Minimum thickness (mm)</b>	<b>Maximum thickness (mm)</b>
<b>A</b>	0.25	0.5
<b>B</b>	0.25	0.75
<b>C</b>	0.25	1.0

The schematic diagram of a typical single lap joint test specimen used for this study is shown in Figure 4.13. The applied displacement at the right end of the overlap by  $u_x$ . The bond line thicknesses measured were found to deviate from the target values. This could be due to improper fixturing, though best efforts were put to ensure the intended bond line thickness. The minimum and maximum thickness on both sides of each single lap joint test coupon was measured using the Keyence microscope. The minimum thickness deviated from its intended value of 0.25 mm and was found to vary between 0.31 mm and 0.49 mm on different specimens. A total of 28 test specimens were fabricated and tested. The test coupons were then grouped into various classes based on the increasing values of their minimum thickness. The minimum and maximum bond line thickness along with their corresponding failure loads are tabulated in Table 4.5. A class interval of 0.05 mm was chosen to group the data into 4 groups over the entire range of minimum bond line thickness recorded. The class interval of 0.05 mm was chosen since the difference in failure loads calculated using Equation 4.1, by substituting the upper and lower limit of each class, was within 5%. A nominal thickness value for each class was calculated by finding the mean of the minimum thickness of each class. The nominal values were used to plot the various resulting failure loads with the difference of the measured maximum thickness from the nominal value.

Table 4.5. Experimentally recorded thickness and failure load

Range	Mean minimum thickness (mm)	Minimum thickness (mm)	Maximum thickness (mm)	Thickness variation (mm)	Failure load (KN)
0.3 to 0.35	0.33	0.31	0.89	0.58	12.24
		0.33	1.16	0.82	9.75
		0.33	1.15	0.82	8.21
		0.32	1.08	0.77	10.78
		0.34	0.62	0.28	14.21
		0.34	0.57	0.23	13.68
0.35 to 0.4	0.37	0.38	1.03	0.65	10.40
		0.35	1.04	0.69	8.14
		0.39	0.88	0.48	12.82
		0.39	0.90	0.50	10.61
		0.40	0.83	0.43	11.95
		0.38	0.89	0.51	11.22
		0.36	0.82	0.46	12.54
		0.38	0.53	0.16	13.15
		0.37	0.64	0.26	13.80
0.4 to 0.45	0.42	0.37	0.60	0.23	13.02
		0.41	1.15	0.74	7.73
		0.42	1.18	0.76	8.62
		0.42	0.60	0.18	11.44
0.45 to 0.5	0.47	0.42	0.68	0.26	11.74
		0.49	1.12	0.63	9.19
		0.48	1.15	0.67	5.54
		0.46	1.16	0.70	7.73
		0.48	0.92	0.44	12.03
		0.45	0.77	0.32	10.16

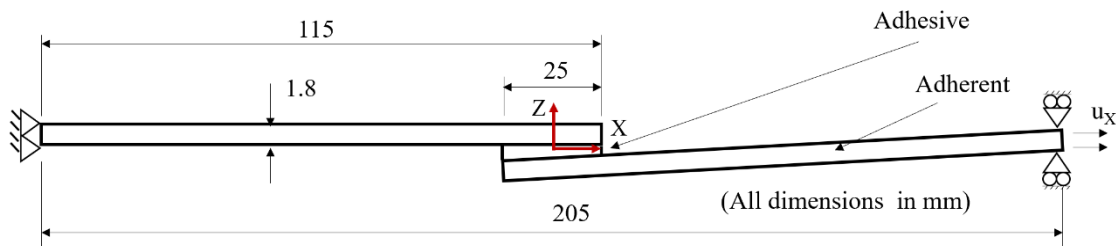


Figure 4.13. Dimensions of single lap joint with varying bond line thickness

All the tested specimens exhibited a light fiber tear failure in the misaligned adherend. The results from the lap shear tests indicate that the failure load decreases with an increase in the difference in minimum and maximum thickness of a single lap joint with linear thickness variations. This pattern was seen across all the thickness classes. The failure loads for joints having no thickness variation were obtained from the fit curve shown in Figure 4.3. in Section 4.1.1. The degree of fit used ( $n$ ) and the coefficient of determination ( $R^2$ ) have been shown in each of the graphs in Figure 4.14. The curve fit equations for each of the classes of minimum thickness are given as Equations 4.2 to 4.5.

Minimum thickness 0.33 mm

$$P = -6.7 \Delta t + 15.27 \quad (4.2)$$

Minimum thickness 0.37 mm

$$P = -7.02\Delta t + 14.75 \quad (4.3)$$

Minimum thickness 0.42 mm

$$P = -6.67\Delta t + 13.16 \quad (4.4)$$

Minimum thickness 0.47 mm

$$P = -8.21\Delta t + 13.35 \quad (4.5)$$

where:  $P$  = Failure load

$\Delta t$  = Difference in bond line thickness

The failure strength decreases by approximately 38%, 42%, 46% and 57% for each of the classes 0.33 mm, 0.37 mm, 0.42 mm and 0.47 mm of minimum thickness, when the maximum thickness measured at the opposite end of the overlap increases.

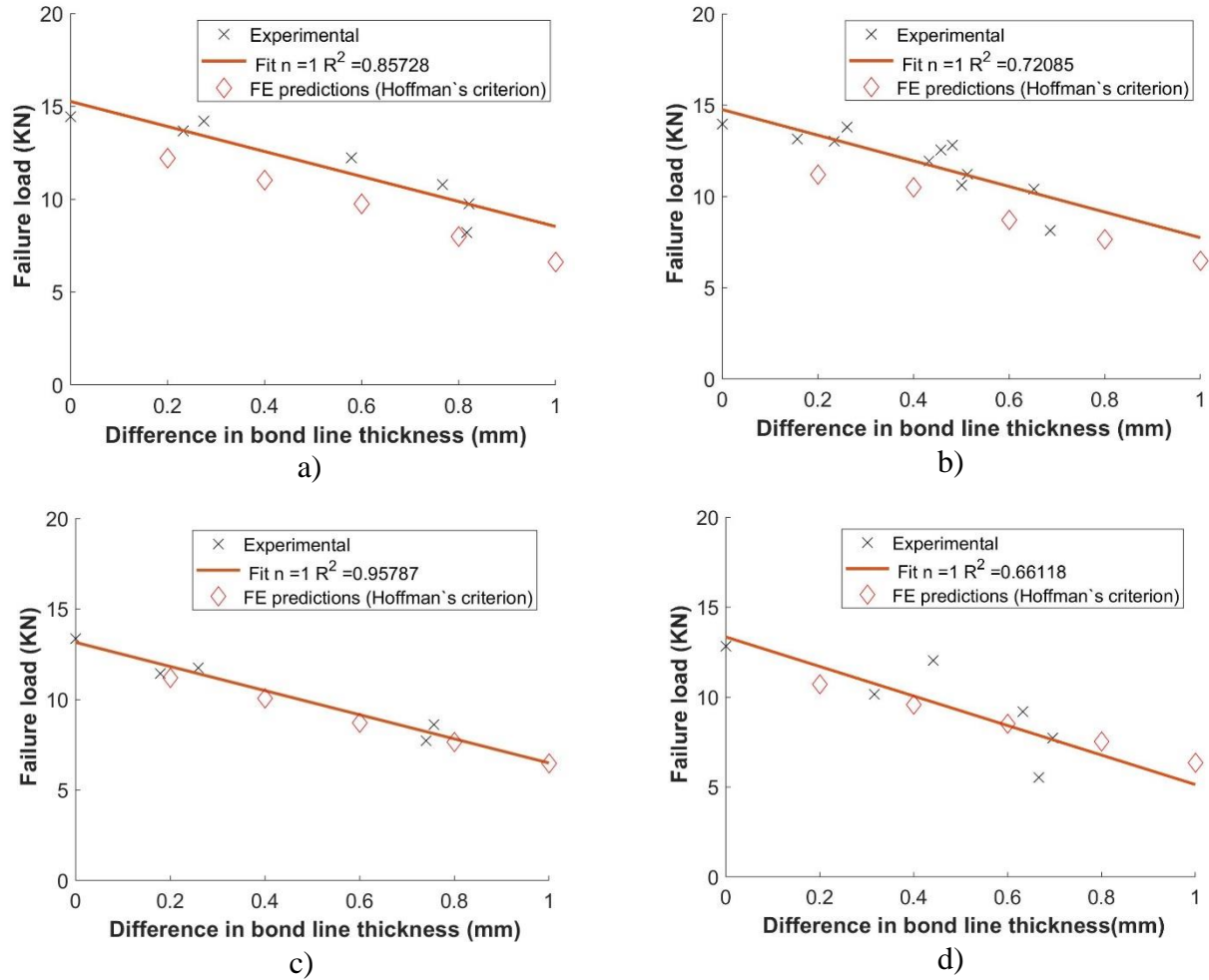


Figure 4.14. Plots of failure load v/s difference between the lower and maximum thickness of a single lap joint having varying bond line thickness with a nominal initial thickness of a) 0.33 mm b) 0.37 mm c) 0.42 mm and d) 0.47 mm. (n – degree of fit,  $R^2$  – correlation coefficient)

#### 4.2.2 Numerical Analysis

A FE model was prepared to predict the failure load and study the variations in stresses in the adherends. The FE model was meshed with a fine mesh of size 0.02 mm at the ends of the overlap, which was graded to a coarser mesh of size 2 mm towards the end of the joint model. The mesh details of the joint are shown in Figure 4.15.

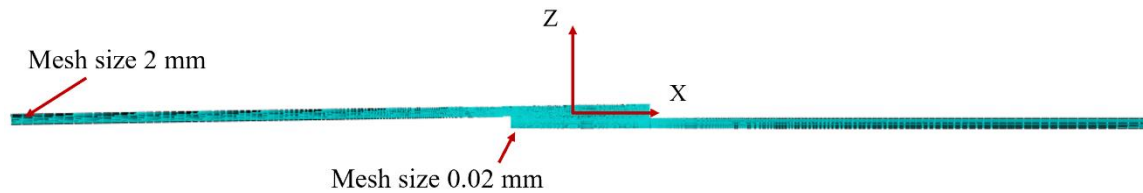


Figure 4.15. Mesh details for a joint with varying bond line thickness

Two-dimensional (2D) plane strain elements were used for the analysis. The critical zone method as described in Section 2.3.2 and Section 4.1.2 was used for predicting the strength of joints with varying bond line thickness. The nominal minimum thickness was chosen as the mean of the actual minimum thickness of each class, as shown in Table 4.6. The maximum thickness was calculated such that the difference between the maximum and the minimum thickness amounted to 0.2, 0.4, 0.6, 0.8 and 1.00 mm. The Hoffman's criteria, which was found to predict the failure loads accurately for constant bond line joints in Section 4.1.2, was used to predict the failure loads for each model. The reference volume for the Hoffman's criteria calculated in Table 4.2 was used to predict the strength of each model. The FE model shows a decreasing trend in failure loads with an increase in the difference between minimum and maximum thickness of the joints for each class of minimum thickness considered, as shown in Figure 4.14. The failure loads predicted using the critical zone method and calculated from the experimental fit using the equations 4.2 to 4.5 have been compared in Table 4.6.

Table 4.6. Comparison of experimental and FE predicted failure loads for joints with varying minimum thickness.

<b>Minimum thickness (mm)</b>	<b>Maximum thickness (mm)</b>	<b>Experimental fit (Equation 4.2 to 4.5) (KN)</b>	<b>FE predicted failure loads (KN)</b>	<b>Difference between FE predicted and experimental failure loads (%)</b>
0.33	0.53	13.92	12.2	12.35
	0.73	12.57	11.03	12.25
	0.93	11.23	9.75	13.18
	1.13	9.87	8	18.94
	1.33	8.54	6.63	22.42
0.37	0.57	13.35	11.75	16.14
	0.77	11.95	10.76	12.14
	0.97	10.54	8.96	17.46
	1.17	9.14	7.78	16.31
	1.37	7.74	6.54	16.54
0.42	0.63	11.82	11.2	5.25
	0.93	10.49	10.05	4.2
	1.13	9.2	8.7	5.43
	1.33	7.82	7.65	2.17
	1.53	6.5	6.46	0.62
0.47	0.67	11.71	10.7	8.63
	0.87	10.06	9.57	4.87
	1.07	8.43	8.51	0.95
	1.27	6.78	7.52	11.05
	1.47	5.14	6.34	23.33

The FE models predict a 46%, 44%, 43% and 40% reduction in failure strength for each of the classes 0.33 mm, 0.37 mm, 0.42 mm and 0.47 mm of minimum thickness, when the maximum thickness measured at the opposite end of the overlap increases. The absolute percentage error of the FE predicted loads when compared with the experimental fit values varies from 0.62% to 22%. This variation could be due to the methodology used for data analysis. The minimum thicknesses were grouped into four classes and the average of the minimum thicknesses was used to represent each class. The FE models used the average of the minimum bond thickness and varied the bond thickness at the

maximum bond thickness end. Another factor could be localized variations in bond line thickness across the entire overlap region. The bond line thickness was measured at each end of the lap joint configuration. Variations in thickness within the overlap region was not accounted for and would need further investigation with non-destructive testing like ultrasonic scanning.

A stress analysis was performed on the joint having a minimum thickness of 0.33mm. The minimum bond line thickness was kept constant at 0.33 mm while bond line thickness variations with a difference between the minimum and maximum thickness measuring 0.2, 0.4, 0.6, 0.8 and 1mm from the minimum thickness of 0.33 mm were studied in the FE model. A load of 2000 N was applied at the unconstrained end of the joint as shown in Figure 4.16. The shear and peel stresses were plotted along a path passing through the middle of the first layer closest to the bond line. The results of the joint having an average minimum thickness of 0.33 mm is plotted in Figure 4.17 and Figure 4.18.

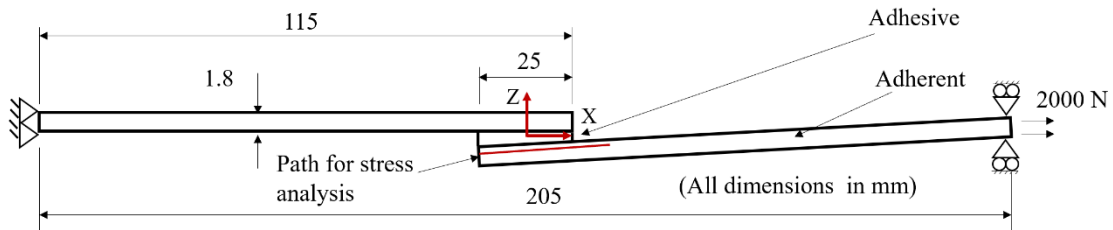


Figure 4.16. Boundary conditions and path for stress analysis for a joint with linear variation in thickness

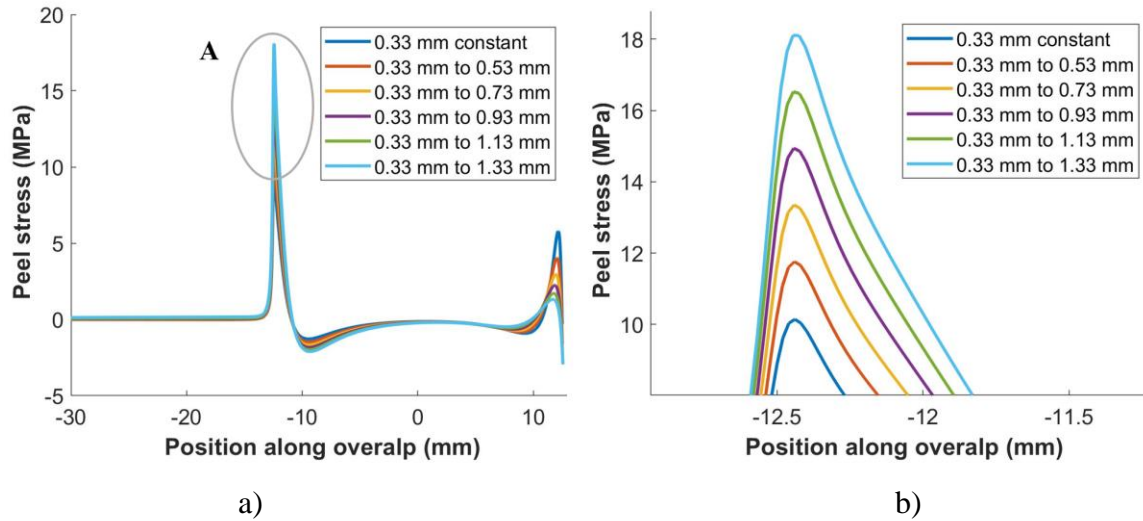


Figure 4.17. a) Plot of peel stress distribution along the middle of first ply closest to the bond line for a joint having average minimum thickness of 0.33mm with various thickness variations b) Magnified view of detail ‘A’

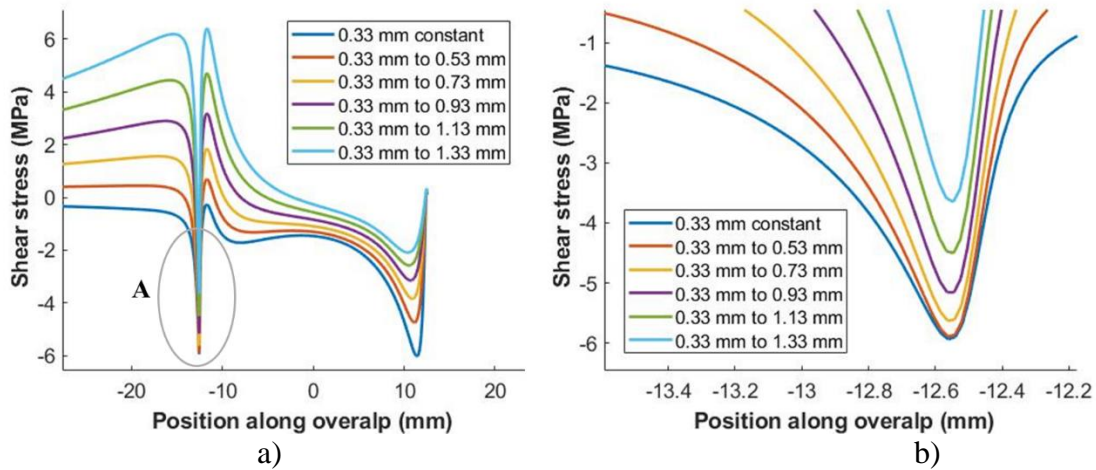


Figure 4.18. a) Plot of shear stress distribution along the middle of first ply closest to the bond line for a joint having a minimum thickness of 0.33mm with various thickness variations b) Magnified view of detail ‘A’

The comparison of maximum shear and peel stress values for increasing difference between minimum and maximum thickness is plotted in Figure 4.19.

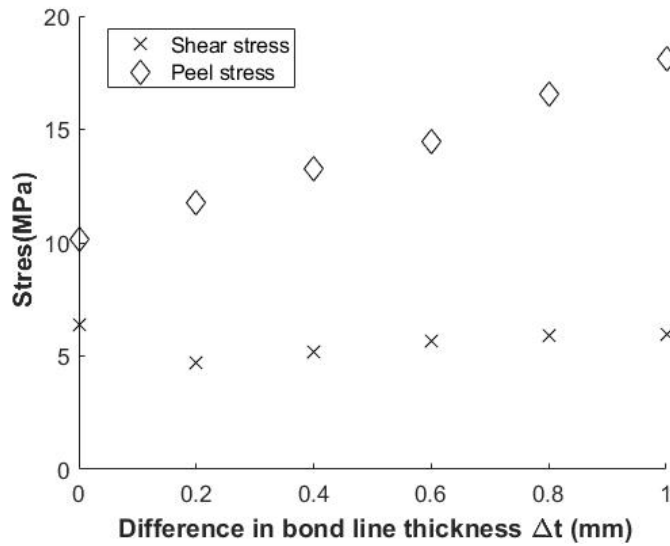


Figure 4.19. Comparison of maximum values of shear and peel stresses for joints with minimum thickness of 0.33 mm and increasing difference between minimum and maximum thickness.

The peel stress increases from 10.14 MPa to 18.1 MPa while the shear stress increases from 6.41 MPa to 5 MPa when a bond line thickness variation of 0.33 mm to 1.33 mm is compared with a uniform bond line joint of 0.33 mm thickness. This increase in the stresses should be the reason for the decrease in failure loads as evident from Table 4.5. in Section 4.2.1.

The influence of bond line thickness on the strength of a bonded joint has been widely studied in the literature. Unfortunately, there is a lack of understanding with regards to the effect of a variation in bond line thickness across the length of the overlap on the strength of bonded joints, that occurs due to a misalignment of the adherends. A misalignment of adherends may occur while joining cylindrical sections in lap joint configurations leading to a variation in thickness across the bond line. The effect of variations in uniform bond line thickness and the effect of linear variation in bond line thickness due to misalignment of the adherends, on the strength of single lap bonded

joints is investigated in the current study. For bonded joints having a uniform bond line thickness, a reduction of approximately 46% is observed in the experimentally fit data, when the bond line thickness increases from 0.25 mm to 1.2 mm. The Critical Zone method using the Hoffman`s failure criterion is found to be the most accurate in predicting the failure loads for bonded joints with a uniform bond line thickness, showing an average absolute error in strength predictions of approximately 7.74% . The stress analysis reveals an increase of approximately 43.43% and 23.7% in peel and shear stresses respectively, when the uniform bond line thickness increases from 0.25 to 1.2 mm. A linear variation in bond line thickness of single lap bonded joints caused by a misalignment of the adherends is found to reduce the failure strength if the bond line thickness increases at either end from its design value. The experimental data suggests that variations in bond line thickness due to misalignments affect the strength of single lap bonded joints by almost 45% on average, for the material set used in this study.

The strength of joint configurations with a linearly varying bond line thickness is predicted using the Critical Zone method using the Hoffman`s criterion, with an accuracy ranging from 0.62% to 22% when compared to the experimental fit values. The stress analysis reveals an increase of 84% and 94% in the peel and the shear stresses respectively, when the bond line thickness variation of 0.33 mm to 1.33 mm is compared with a uniform bond line joint of 0.33 mm thickness. The increase is expected to result from the redistribution of stresses that occurs when the bond joint is not of uniform thickness. The variations between the experimental and finite element predicted strengths may be the result of the bond line thickness variations across the overlap region not being completely accounted for during bond line thickness measurements. The approximation

made while grouping of the test specimens into classes based on the measured minimum bond line thickness may also be a factor behind the variations observed in the finite element predicted and experimental strengths. Designers and manufacturers should be cautious to consider the reduction in strength caused by variations in bond line thickness that result from a misalignment of the adherends.

## CHAPTER FIVE

### Effect of Adhesive Distribution

Adhesives are typically applied in either liquid or paste form or also in the form of tapes [114]. Liquid and paste form adhesives need care during application to ensure an even distribution of the adhesive across the bond area. A lack of precision on the part of the operator or variation in the dispensing equipment could result in an incomplete coverage of the adhesive across the bonded area. The case of incomplete adhesive coverage was tested in this research by improperly applying the adhesive while forming a bond joint between two carbon fiber adherends. It was determined that when the adhesive was applied along a straight line, it spread out into an elliptical shape as shown in Figure 5.1. Similarly, when applied as a circular mound of material, the adhesive spreads out into a circular shape. These shapes fall short of the complete rectangular coverage needed to form a complete bond joint, which is expected to result in a loss of strength.

Incomplete adhesive distribution across the bond overlap has not been extensively researched in literature. Researchers have predominantly addressed the effects of variation in overlap length on the strength of bonded joints. Gultekin, et al. [42] made an observation that square shaped adhesives have a better load carrying capacity than rectangular shaped adhesives. The increase in failure load was attributed to a better stress distribution, in the case of a square shaped adhesive.

The aim of this chapter is to quantify, experimentally and numerically, the effects of an incomplete distribution of the adhesive and demonstrate the ability of the ultrasonic

scanning systems to detect such imperfections. This chapter has been divided into two parts. The first part presents the experimental work performed with woven composites using various adhesive shapes which appears in [115]. The ability to identify incomplete adhesive distribution using ultrasonic scanning is established. The study is then extended to bonded joints consisting of unidirectional carbon fiber composite adherends. Finite element analysis is performed by creating a 3D model of the bonded joints for the different adhesive distributions.

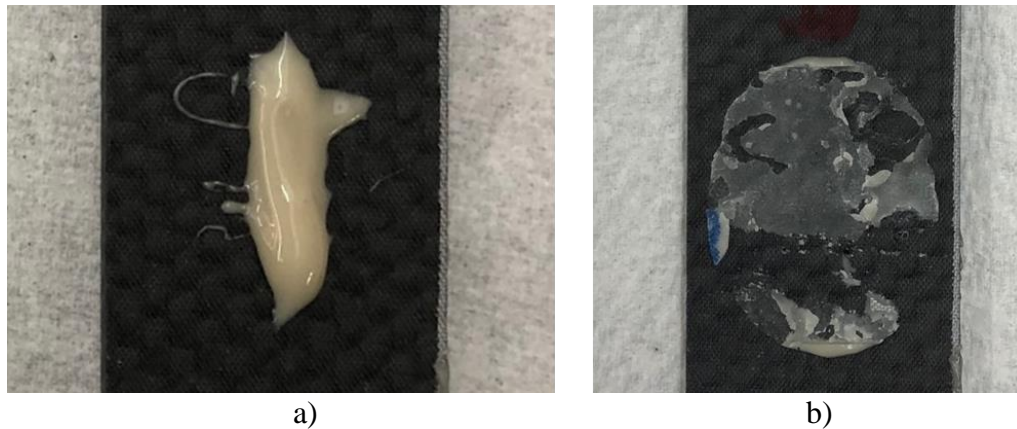


Figure 5.1. a) Adhesive applied along a straight-line b) shape attained after pressure application using the second adherend (Major axis: 25 mm, Minor axis: 21 mm)

### *5.1 Incomplete Adhesive Coverage: Woven Composites*

#### *5.1.1 Experimental Details*

Carbon fiber adherends were fabricated using a T300 plain weave woven carbon fiber composite fabric (Toray International America, New York, USA). Single lap joint samples were fabricated as described in Section 3.1.1. The carbon fiber fabric was laid up in a  $[0/+45/0]_3$  configuration totaling 9 layers resulting in adherend thickness of 2.3 mm. A two-part epoxy adhesive, Fiber Glast 1101 [116] (Fibre Glast Developments Corp,

Brookville, USA), was used for this study. The adhesive was replaced with Hysol 9309 NA adhesive [106] (Henkel Corp, Ohio, USA) for all the other studies with unidirectional composites because of the well documented and consistent chemical and mechanical properties of Hysol 9309 NA . Single lap joint specimens were fabricated with the same dimensions as shown in Figure 3.2 in Section 3.2.1. Three samples were tested for each joint configuration. The required adhesive shapes were created by using templates made of 0.2 m thick PTFE film cut out to form the desired shape. The various shapes and sizes used for this study are detailed in Table 5.1.

Table 5. 1. Experimental plan for study of effect of incomplete adhesive coverage in single lap joints. (Specimen identifiers are shown in brackets), (All dimensions in mm)

<b>Adhesive Shape</b>	<b>Size Level 1</b>	<b>Size Level 2</b>	<b>Size Level 3</b>
<b>Circular</b>	Diameter 25.4 (C1)	Diameter 19.05 (C2)	Diameter 16.35 (C3)
<b>Elliptical Orientation -1</b>	a = 25.4, b = 19.05 (E1-1)	a = 25.4, b = 12.7 (E1-2)	a = 25.4, b = 6.35 (E1-3)
<b>Elliptical Orientation -2</b>	a = 19.05, b = 25.4 (E2-1)	a = 19.05, b = 25.4 (E2-2)	a = 19.05, b = 25.4 (E2-3)
<b>Rectangular</b>	25.4 x 25.4 (R)		

An Elliptical shape with two different orientations and a circular shape, each with three different size levels were selected for this study. Figure 5.2. shows the PTFE cutouts used for this study. The orientations of the elliptical shape adhesive are defined with respect to the loading axis with  $X$  being the load direction while  $Y$  being the transverse direction. Elliptical orientation 1 has the major axis aligned along  $X$  axis while orientation 2 has its major axis aligned along  $Y$  axis. The lengths of the axes along  $X$  and  $Y$  directions have been indicated using ‘ $a$ ’ and ‘ $b$ ’ respectively. During the bond joint

fabrication, the PTFE cutouts remained in the bonded joints during adhesive curing since they do not adhere to the adhesive and function as an empty space effectively [59]. The single lap joint test coupons were ultrasonically scanned and then tested for lap shear strength on a MTS Q-Test 100 tensile testing machine (MTS Systems Corporation, Eden Prairie, USA) having a load rating of 100 KN at a crosshead displacement controlled rate of 0.02 mm/sec for all the tests.

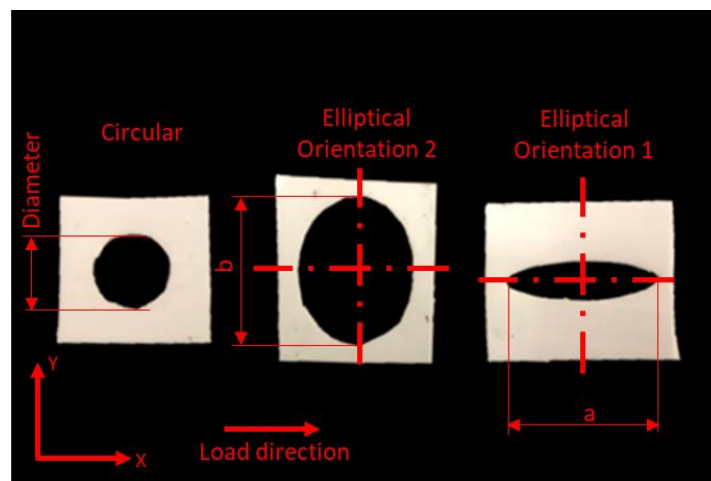


Figure 5.2. PTFE cutouts for fabricating the required adhesive shapes.

Each bond joint that was fabricated with incomplete adhesive coverage was ultrasonically scanned on a custom in-house ultrasonic scanner [19] designed for this purpose as shown in Figure 5.3 .The specimens were scanned in the bonded region along a path as shown in Figure 5.4. A 10 MHz transducer (Olympus, Massachusetts, United States) measuring 0.5 in in diameter and having a 38 mm spherical nominal focal length was used for this study. The ultrasonic signals were sampled in a US Ultratek pulser/receiver (US Ultratek, California, United States). The transducer was mounted on translational stages made by Velmex (Velmex, New York, United States). A parallel coupled bi-slide was used to provide the required motion of the transducer along the X

and Y axes, with a resolution of 0.0013 mm/step. A raster resolution of 0.2 mm/scan was used for this study.

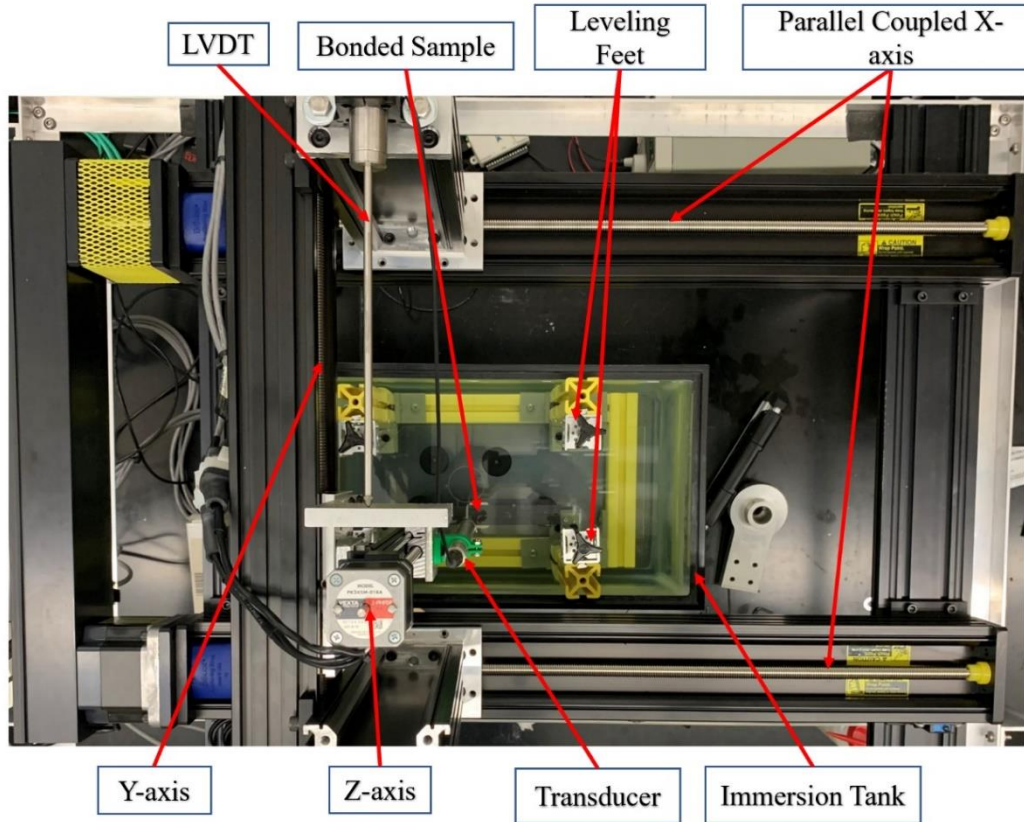


Figure 5.3. Custom immersion scan system

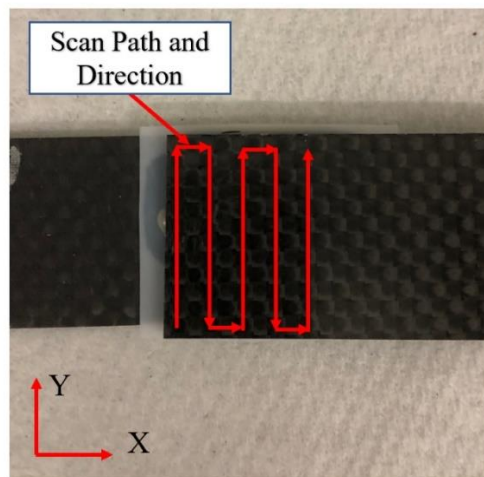


Figure 5.4. Ultrasonic scan path and direction

Light fiber tear failure was observed in all the lap shear tests. The failed surfaces for a joint with complete adhesive coverage (*R*-configuration) is shown in Figure 5.5. The results of the lap shear tests performed are summarized in Table 5.2.

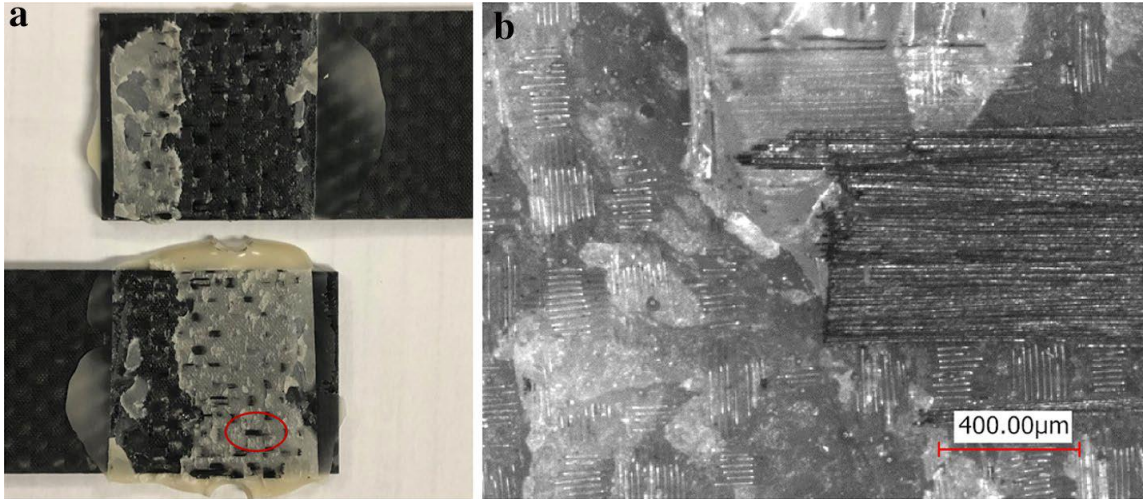


Figure 5.5. a) Failed surface as observed in joints having complete adhesive coverage. b) Magnified image of failed adhesive surface from the region highlighted in a, showing adherent failure

Table 5. 2 Comparison of failure loads across various configurations.

<b>Adhesive Shape</b>	<b>Specimen Identifier</b>	<b>Bond area (mm<sup>2</sup>)</b>	<b>Failure Load (KN)</b>
<b>Circular</b>	C1	506.71	4.76±1.19
	C2	285	3.69±0.14
	C3	126.68	2.45±0.07
<b>Elliptical Orientation -1</b>	E1-1	380.03	3.98±0.47
	E1-2	253.67	3.04±0.45
	E1-3	126.68	2.15±0.39
<b>Elliptical Orientation -2</b>	E2-1	380.03	4.62±0.9
	E2-2	253.67	4.26±0.31
	E2-3	126.68	3.1±0.47
<b>Rectangular</b>	R	645.16	8.46±2.13

A trend is seen where failure load decreases with a decrease in bonded joint area for each of the configurations as expected. The failure strength decreases by approximately 48%, 46% and 33% respectively for the circular, elliptical (orientation 1) and elliptical (orientation 2). The failure load is highest for the joint with complete coverage of adhesive. Considering the failure loads of joints with incomplete coverage, the circular shaped adhesive has the highest failure load. Comparing the failure loads of elliptical shaped adhesive configurations, the elliptical shaped adhesive of orientation 2 exhibits a higher failure load as compared to orientation 1. The failure strengths of the configurations *E2-1*, *E2-2* and *E2-3* are greater than those of *E1-1*, *E1-2* and *E1-3* by 14%, 29% and 31% respectively.

Ultrasonic scans were performed on the single lap joints prior to testing them for lap shear strength. The A-,B- and C- scans were generated with a custom MATLAB code using the data from the ultrasonic system described in Section 5.1.1. The A-scan at a location of  $X = 2$  mm and  $Y = 2$ mm of a carbon fiber laminate (unbonded) is as shown in Figure 5.6a. Distinct peaks appear at the front wall and the back wall of the composite adherend shown. The A-scans along  $X = 2$  mm form the B-scan appearing in Figure 5.6b. The individual plies are detected due to the intensity of sound energy reflected from each ply which are indicated in the B-scan in Figure 5.6 b. The A-scans for a bonded joint appear in Figure 5.7. Figure 5.7a shows an A-scan at a location of PTFE template which remains in the bonded area post fabrication, while Figure 5.7 b shows the A-scan taken from the location where adhesive is present. A peak is seen as the sound is reflected from the PTFE film. This reflection is caused by an acoustic impedance mismatch between the carbon fiber adherend and the PTFE film. The B-scans showing the positions of the

adhesive and the PTFE film are shown in Figure 5.8. C-scans of the bonded specimens were generated to evaluate the shape, size and distribution of the adhesive as shown in Figure 5.9. The red region indicates the PTFE film while the blue region indicates the adhesive. The area of the bonded region was measured in MATLAB by calling the images using the “imread” function and measuring area of the curve generated by picking the outer edge of the C-scan image and the broken surface image. For the circular configuration (*CI*) shown in Figure 5.9 a, the difference between the measured areas is approximately 9% of the C-scan area while that for the elliptical configuration (*E2-2*), it is approximately 7%. The outline of the shapes was overlaid and found to fit the shape from the C-scans. Thus, it can be concluded the C-scans are able to resolve the shape and the size of the adhesive.

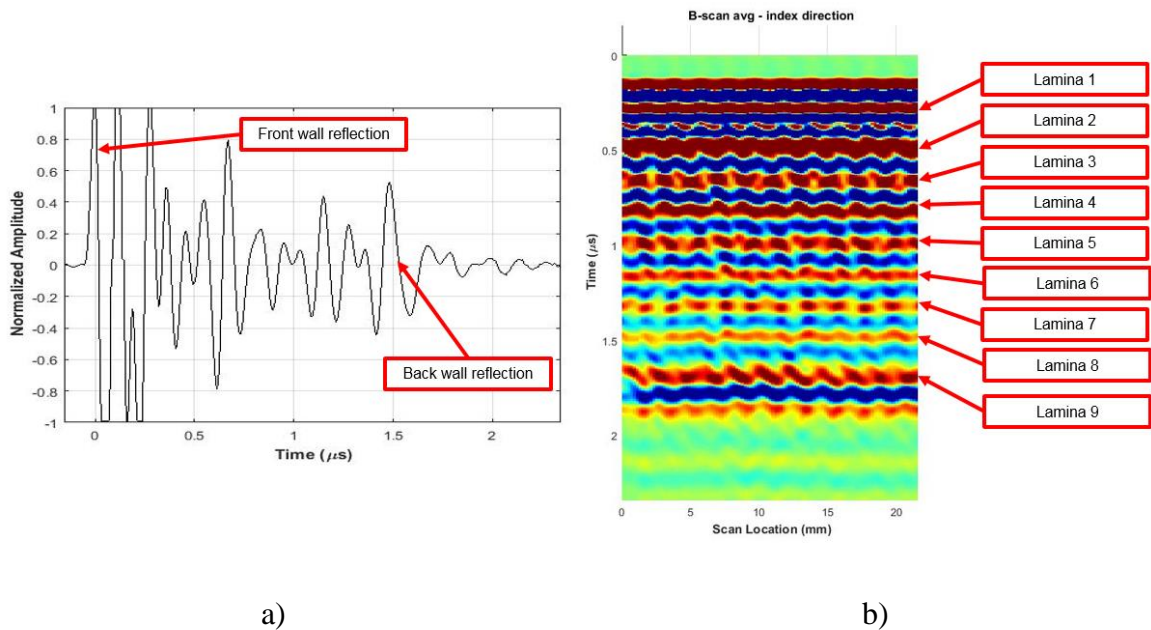


Figure 5.6. a) A-scan at  $X = 2$  mm,  $Y = 2$  mm, and b) B-Scan at  $X = 2$  mm of an unbonded Carbon fiber laminate plate

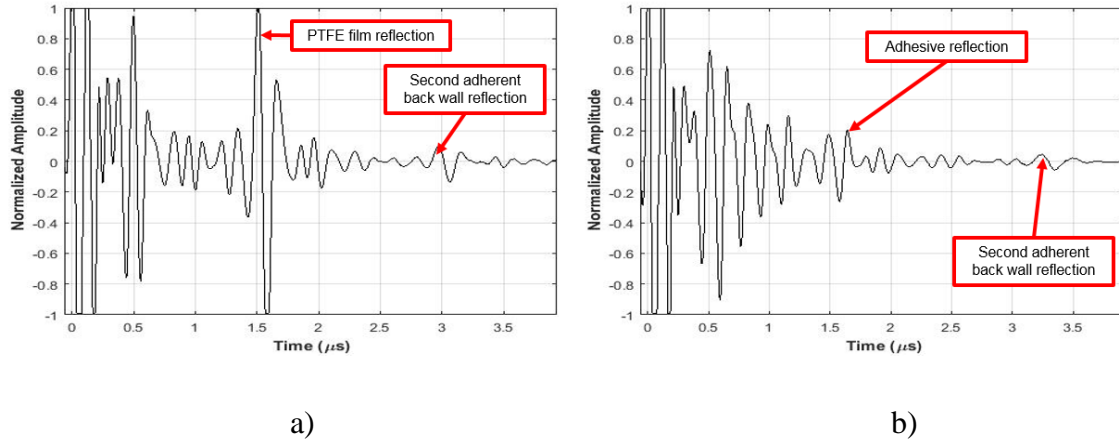


Figure 5.7. Comparison of A-scans at overlap region of the adhesive overlap in the a) PTFE film region and the b) Adhesive region

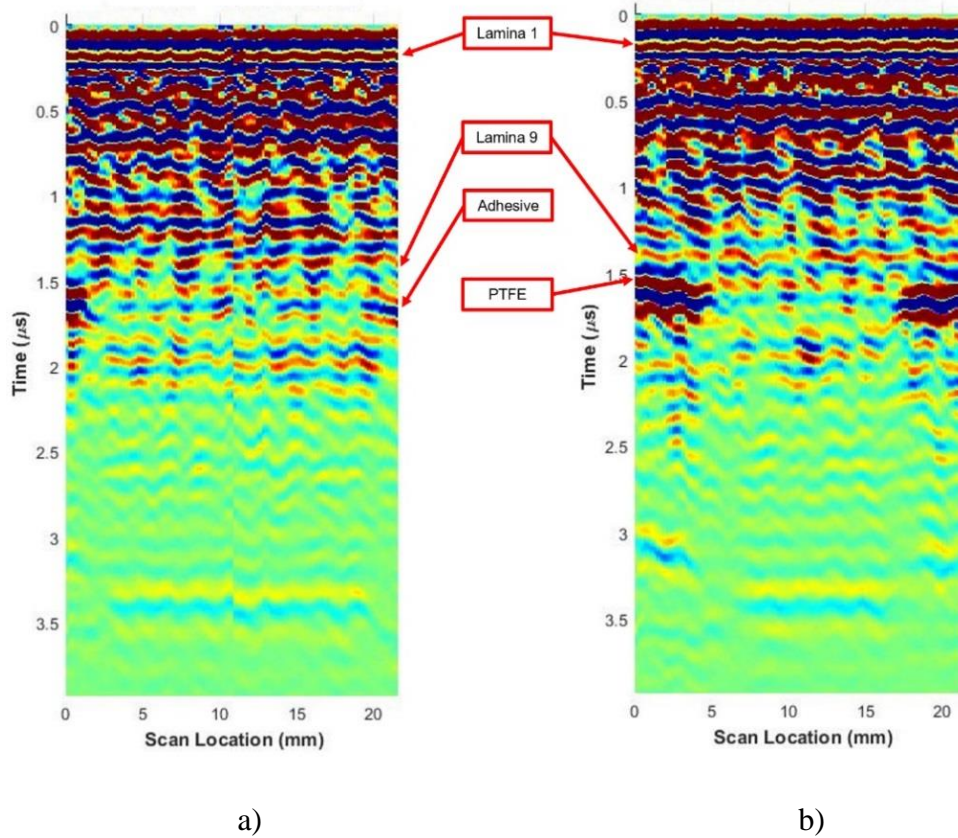


Figure 5.8. B-Scans along a)  $X = 2$  mm and b)  $X = 12$  mm

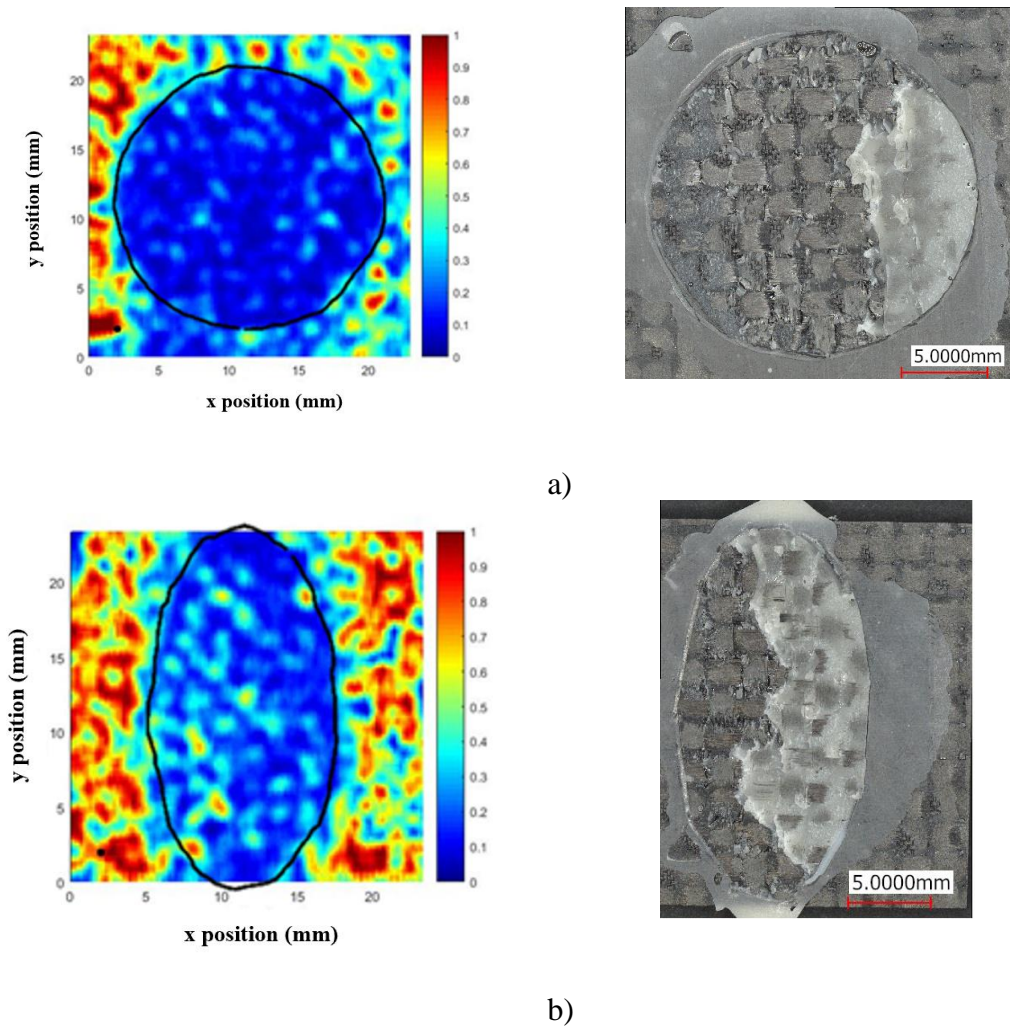


Figure 5.9. C-Scan images at the bond line and comparison with their corresponding broken surfaces of the configurations a) C1, b) E2-2 (The Black outlines on the left images are the adhesive outlines traced from the optical images on the right.)

## 5.2 Incomplete Adhesive Coverage: Unidirectional Composites

### 5.2.1 Experimental Details

The same test configurations used for the study in woven composites as appearing in Table 5.1. in Section 5.1.1, were used in the study with unidirectional composites. The unidirectional carbon fiber test coupons were fabricated using the same procedure as described in Section 3.1.2. The specimens were tested for lap shear strength on the

Instron 3382A tensile testing machine (Instron, Massachusetts, USA), having a load cell rating of 100 KN, at displacement-controlled loading rate of 0.05 mm/min. A total of 5 test specimens for each configuration were tested for strength. The unidirectional carbon fiber test coupons were scanned ultrasonically using the procedure as described in Section 5.1.1. The scans were not able to resolve the shape or position of the adhesive due to the huge noise seen in the C-scans which could be due to higher porosities in the outer layer of the carbon fiber adherends leading to a huge attenuation of signals.

All lap shear test specimens exhibited a light fiber tear failure in the adherend. The failure loads for each of the configurations have been summarized in Table 5.3.

Table 5.3. Comparison of failure loads across various configurations.

<b>Adhesive Shape</b>	<b>Specimen Identifier</b>	<b>Bond area (mm<sup>2</sup>)</b>	<b>Failure Load (KN)</b>
<b>Circular</b>	C1	506.71	10.03±0.63
	C2	285	6.65±0.82
	C3	126.68	3.49±0.49
<b>Elliptical Orientation -1</b>	E1-1	380.03	8.69±0.72
	E1-2	253.67	6.07±0.37
	E1-3	126.68	3.1±0.15
<b>Elliptical Orientation -2</b>	E2-1	380.03	9.28±0.27
	E2-2	253.67	6.23±0.49
	E2-3	126.68	3.47±0.17
<b>Rectangular</b>	R	645.16	14.47±1.6

A similar trend as observed with woven carbon fiber composites as shown in Table 5.2. is seen with the unidirectional composites. In the case of unidirectional composites, the failure strength of elliptical orientation 2 exceeds the failure load of orientation 1 by 6.3%, 2.5% and 10.73% respectively for the size levels of 1,2 and 3. The failure strength also decreases for each shape with a decreasing bond coverage area. A

reduction of approximately 66%, 64% and 63% are observed for the circular, elliptical (orientation 1) and elliptical (orientation 2) respectively.

### 5.2.2 Numerical Analysis

The 3D finite element model was created in ABAQUS CAE (3DS Dassault systems, Massachusetts, USA) for stress analysis for the single lap joint configurations with incomplete coverage is as shown in Figure 5.10. A 3D 8 node element (ABAQUS CAE element type C3D8) was used for the analysis. The adherends and the adhesive were created as separate parts and were assembled in ABAQUS CAE using the tie constraints. The boundary conditions were same as that described in Figure 3.11 in Section 3.2.1, with one end of the single lap joint model fixed while the other end where the axial load is applied, constrained to move in the  $X$  direction.

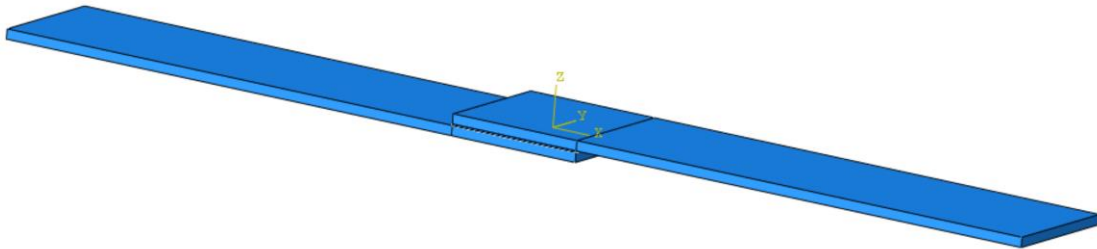


Figure 5.10. 3D model used for FE analysis.

The different adhesive shapes as described in Table 5.3. were created in a plane parallel to the adherend-adhesive interface and were extruded in the  $z$ -direction to form the 3D adhesive domain. The mesh details of an elliptical and circular shape (sizes described in Table 5.3) are as shown in Figure 5.11. A mesh size of 0.02 mm was used which was graded to a size of 2 mm. The same mesh was created on the mating adherends to prevent

any errors arising due to nodes on the mating surfaces being outside of the position tolerance. The mesh assembly details for a circular shaped adhesive (configuration C2) are shown in Figure 5.11.

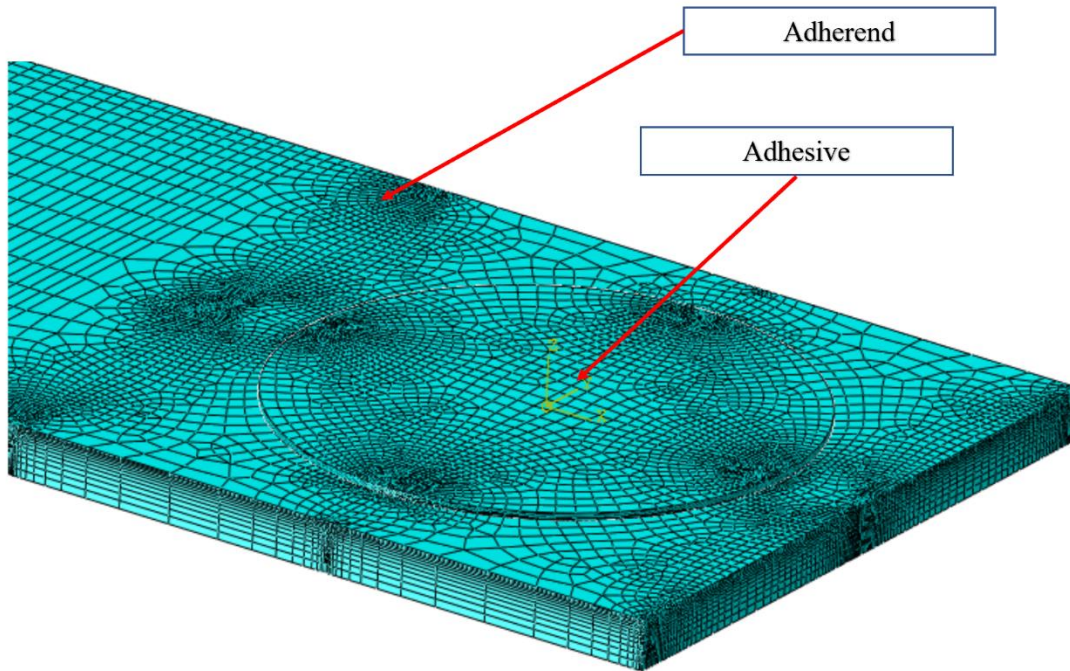


Figure 5.11. Mesh assembly details for a circular shaped adhesive (C2 configuration)

Stresses in the middle first ply counted from the bond line and the middle of the bond were measured by using the path option. The paths were placed along and transverse to the loading axis as shown in Figure 5.12.

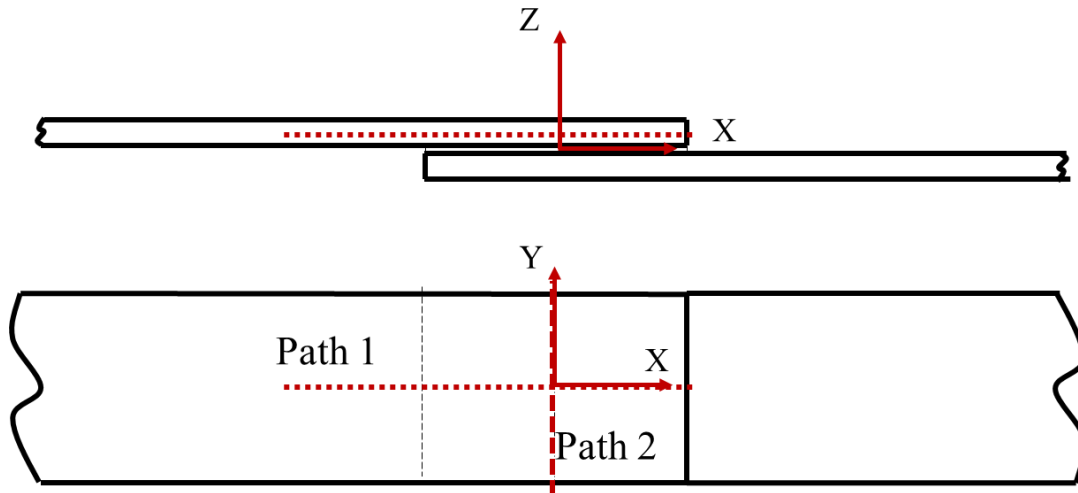
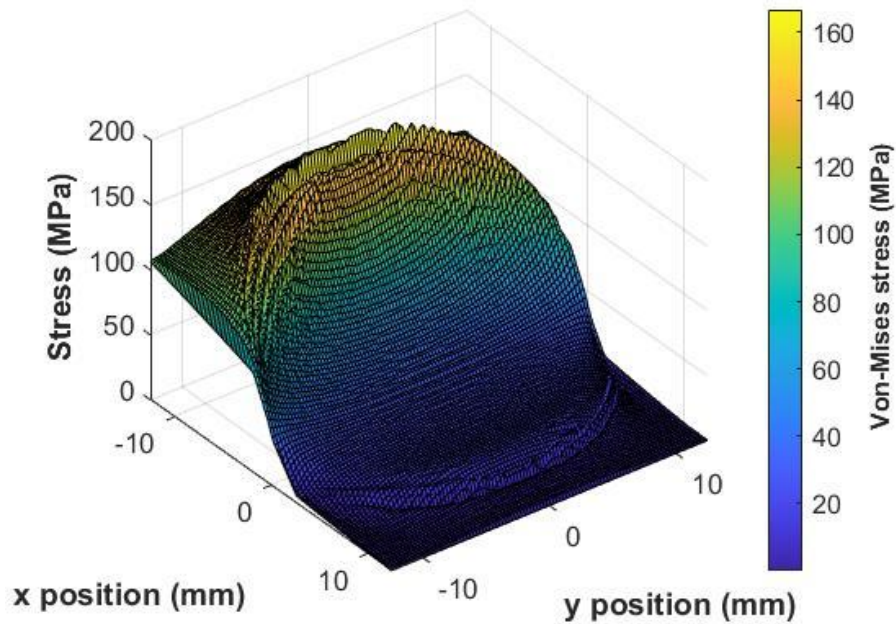
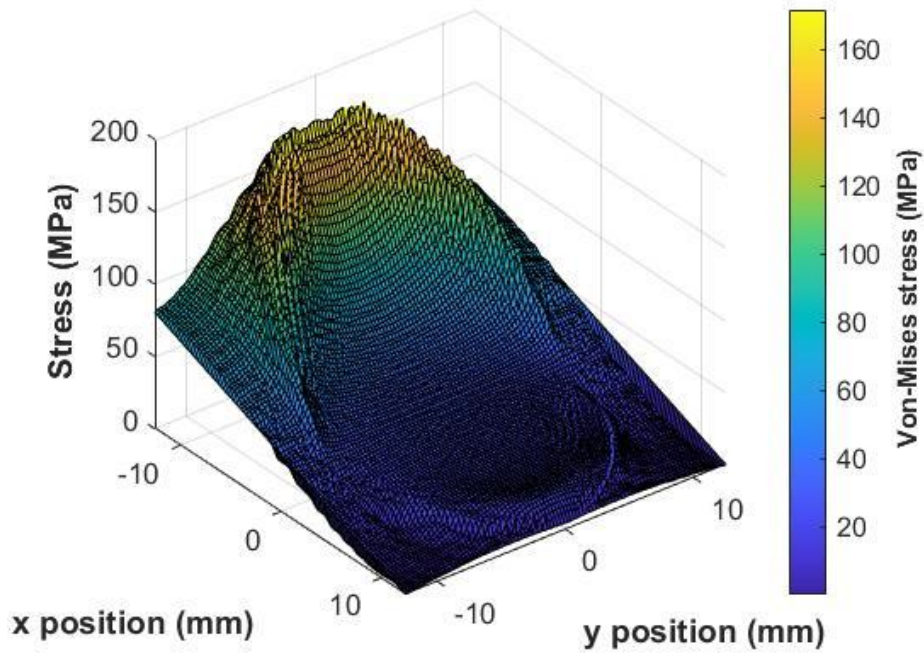


Figure 5.12. Paths used to extract stress values.

The models were loaded at a tensile load of 2000 N for stress analysis. Von-mises stress distributions over the entire overlap region of the bonded joint, along the mid plane of the first ply adjacent to the bond line have been plotted in Figure 5.13. for the elliptical shaped adhesive configurations E2-1 and E1-1.



a)



b)

Figure 5.13. Von Mises stress for a) E2-1 and b) E1-1 configurations

The  $x$  and  $y$  positions shown in Figure 5.13. are along the loading axis ( $X$  axis) and transverse direction ( $Y$  axis) respectively. The equivalent stresses peak at the ends of the overlap irrespective of the orientation of the adhesive along the loading direction. The stresses do not vary considerably in the transverse direction ( $Y$  axis). Thus, all subsequent stress analyses have been performed along Path 1 as shown in Figure 5.12.

The shear and the peel stresses for elliptical orientation 1, elliptical orientation 2 and circular shapes, in the first ply along the loading direction appear in Figure 5.14., Figure 5.15. and Figure 5.16.

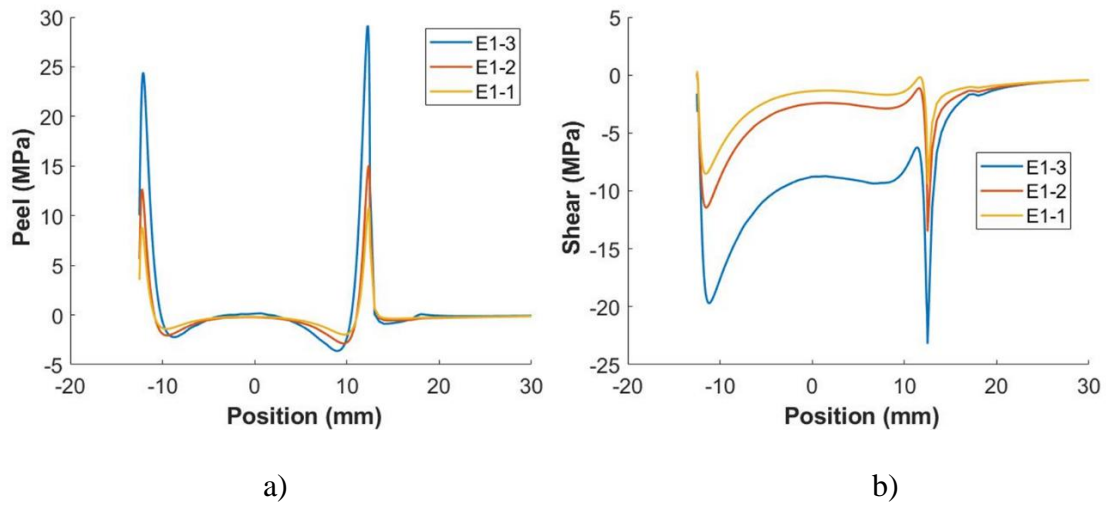


Figure 5.14. Comparison of a) Peel stress and b) Shear stress along the middle of first ply for elliptical adhesive shape of orientation 1

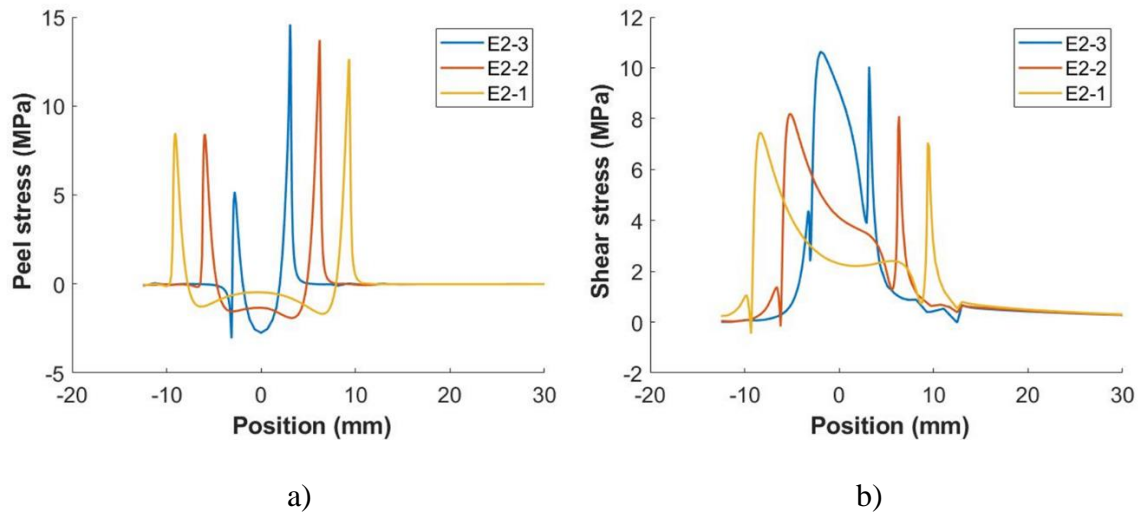


Figure 5.15. Comparison of a) Peel stress and b) Shear stress along the middle of first ply for elliptical adhesive shape of orientation 2

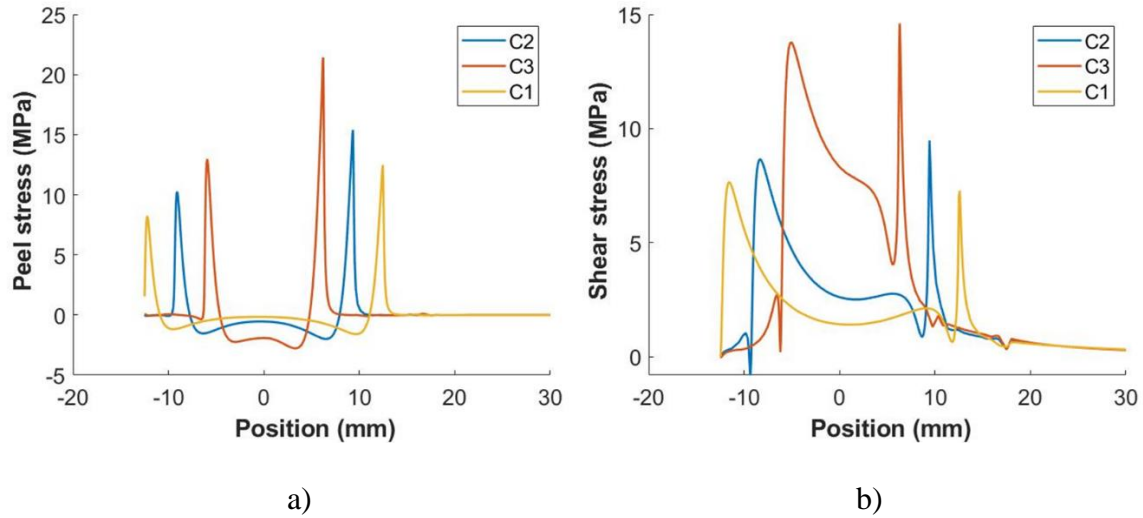


Figure 5.16. Comparison of a) Peel stress and b) Shear stress along the middle of first ply for circular adhesive shape

The stress plots indicate that the shear and the peel stresses increase as the size decreases in each adhesive shape. For the elliptical shaped adhesive of configuration 1, the maximum peel stress increases from 10.79 MPa to 29.08 MPa by approximately 169% while the maximum shear stress increases from 9.4 MPa to 23.2 MPa by approximately 146%, with a reduction of bonded area. For the elliptical shaped adhesive of configuration 2, the maximum peel stress increases from 12.63 MPa to 14.58 MPa by approximately 18% while the maximum shear stress increases from 7.05 MPa to 10.04 MPa by approximately 43%, with a reduction of bonded area. For the circular shaped adhesive, the maximum peel stress increases from 12.47 MPa to 21.42 MPa by approximately 72% while the maximum shear stress increases from 7.28 MPa to 14.6 MPa by approximately 100%, with a reduction of bonded area. The increase in the shear and peel stresses explains the reduction in failure loads as the size of the adhesive decreases.

As discussed above, the failure load for elliptical orientation 2 was found to be higher than that of orientation 1. The shear and peel stresses for each size of the elliptical orientation were compared as shown in Figure 5.17, Figure 5.18, and Figure 5.19.

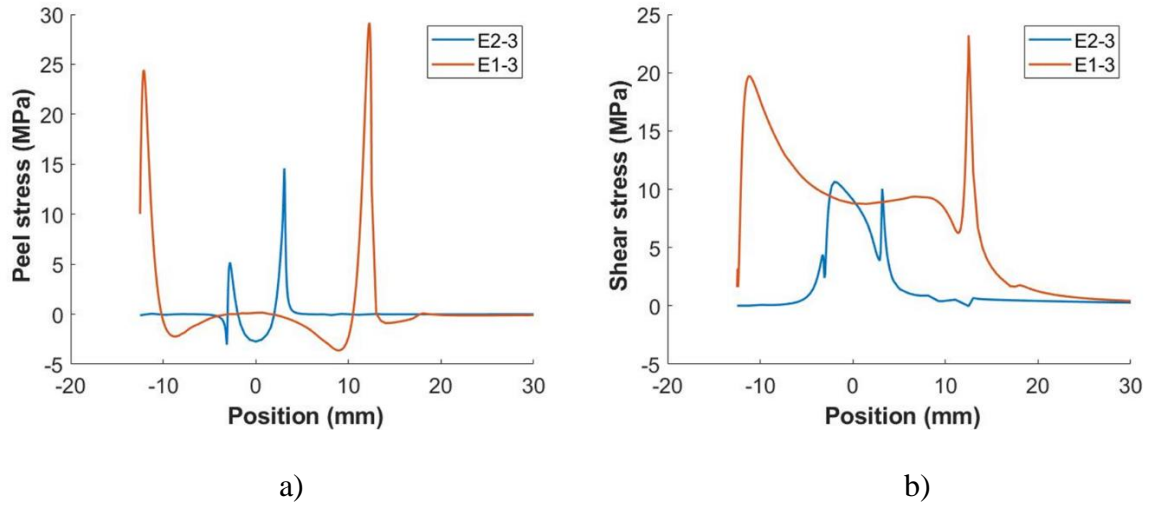


Figure 5.17. Comparison of a) Peel stress and b) Shear stress for elliptical orientations E1-3 and E2-3

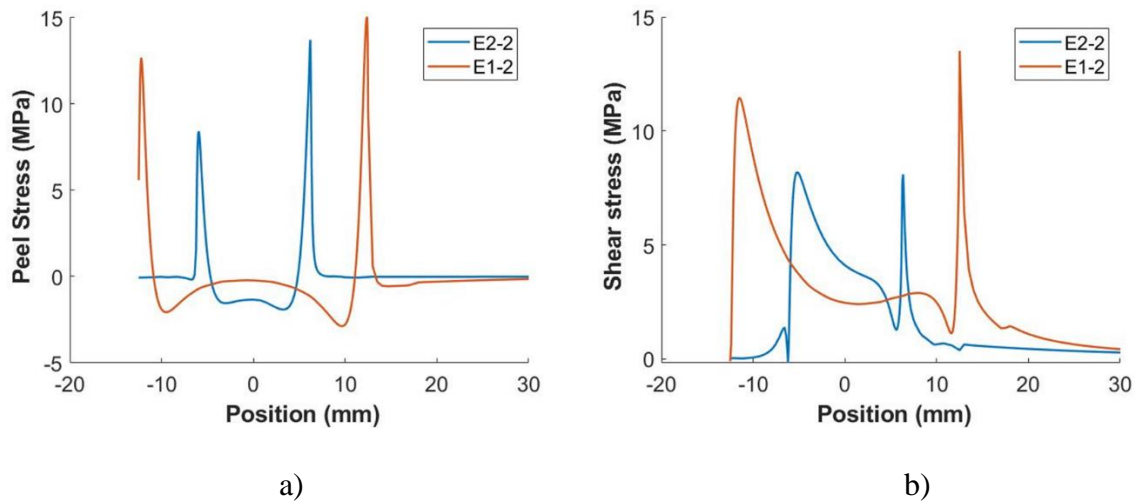


Figure 5.18. Comparison of a) Peel stress and b) Shear stress for elliptical orientations E1-2 and E2-2

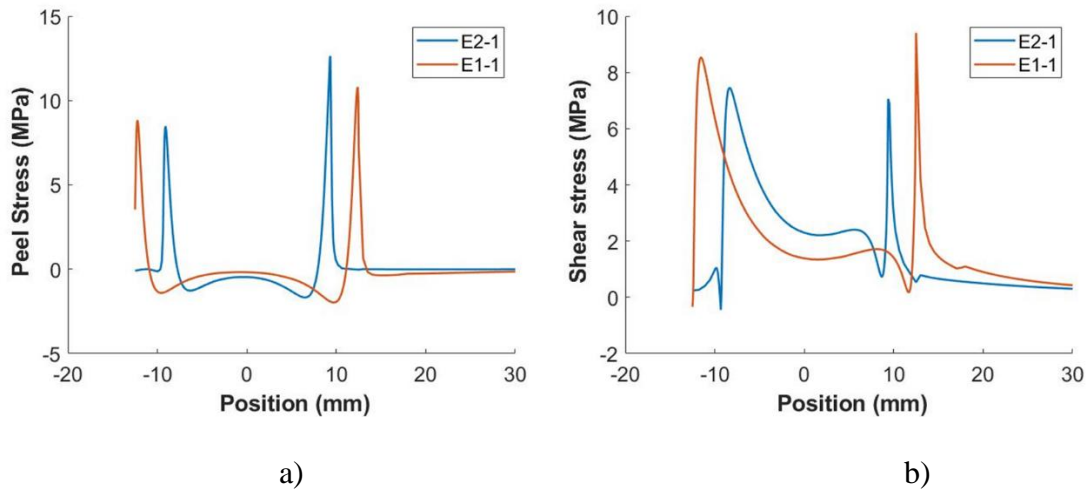


Figure 5.19. Comparison of a) Peel stress and b) Shear stress for elliptical orientations E1-1 and E2-1

The maximum peel increases from 14.58 MPa to 29.08 MPa by approximately 99% while the maximum shear increases from 10.55 MPa to 23.21 MPa by approximately 120% when the adhesive configuration changes from E2-3 to E1-3. The maximum peel increases from 13.71 MPa to 15 MPa by approximately 9% while the maximum shear increases from 8.09 MPa to 13.51 MPa by approximately 67% when the adhesive configuration changes from E2-2 to E1-2. In case of size level 1 The maximum peel decreases from 12.4 MPa to 12.63 MPa by approximately 1.8% while the maximum shear increases from 7.5 MPa to 9.4 MPa by approximately 25% when the adhesive configuration changes from E2-1 to E1-1. Despite the increase in the peel stress, there was a reduction in failure strength observed for configuration E1-1 as compared to E2-1.

To predict the failure loads of the bonded joints with incomplete adhesive distribution, the Critical Zone method as discussed in Section 4.1.3 was applied to the 3D FE model shown in Figure 5.10. To check the validity of the 3D model in predicting failure loads, a preliminary study was performed on models with a complete coverage of

the adhesive, by changing the bond line thickness and comparing the predictions from the 2D model with those from the 3D model. Different bond line thicknesses namely 0.25, 0.5, 0.75, 1.0 and 1.2 mm were modelled. The model with 0.25 mm bond line thickness was used as a reference model to calculate the failure loads of the other configurations. The Hoffman`s criterion [90] was used in the 3D analysis by adapting the general form of Hoffman`s equation as given below. The detailed description of the adaptation is given in Appendix C.

$$C_1(\sigma_y - \sigma_z)^2 + C_2(\sigma_z - \sigma_x)^2 + C_3(\sigma_x - \sigma_y)^2 + C_4(\sigma_x) + C_5(\sigma_y) + C_6(\sigma_z) + C_7(\tau_{yz})^2 + C_8(\tau_{xz})^2 + C_9(\tau_{xy})^2 \geq 1 \quad (5.1)$$

where:

$$C_1 = 0.5 \left( \left( \frac{2}{Z_t Z_c} \right) - \left( \frac{1}{X_t X_c} \right) \right)$$

$$C_2 = 0.5 \left( \frac{1}{X_t X_c} \right)$$

$$C_3 = C_2$$

$$C_4 = \frac{1}{X_t} - \frac{1}{X_c}$$

$$C_5 = \frac{1}{Z_t} - \frac{1}{Z_c}$$

$$C_6 = C_5$$

$$C_7 = \left( \frac{1}{S_{yz}} \right)^2$$

$$C_8 = \left( \frac{1}{S_{xz}} \right)^2$$

$$C_9 = C_8$$

The various notations used are:

$X_t, X_c$  are the longitudinal failure strengths of the composite in tension and compression

$Z_t, Z_c$  are the transverse failure strengths of the composite in tension and compression

$S_{xy}, S_{xz}, S_{yz}$  are the interlaminar shear strengths of the composite

$\sigma_x, \sigma_y, \sigma_z, \tau_{xz}, \tau_{xy}, \tau_{yz}$  are the stress components in X, Y and Z directions as shown in Figure 5.12.

The failure loads for lap joints having various thicknesses, compared with experimental values discussed in Section 4.1 are as shown in Figure 5.20. The 3D FE model used predicted the failure loads for the various uniform bond line thicknesses as shown in Figure 5.20.

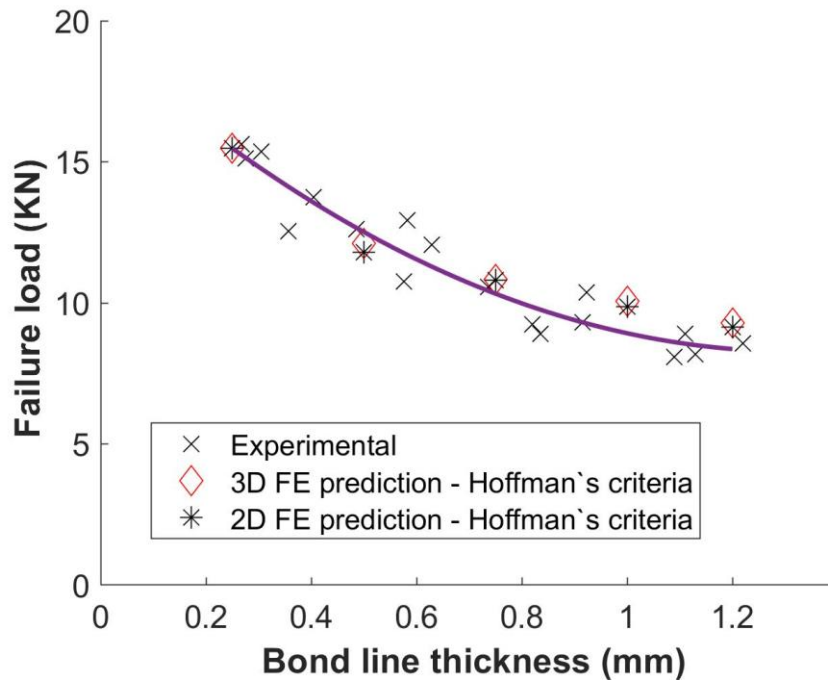
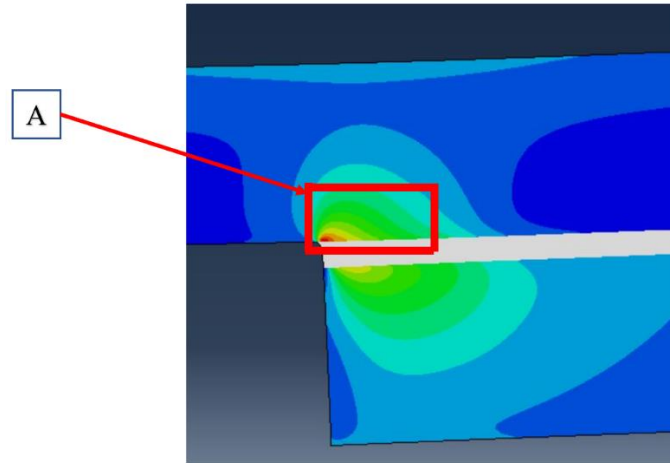


Figure 5.20. Experimental and 3D FE prediction of failure loads for various bond line thickness with complete coverage of adhesive using Hoffman's criteria.

The critical zone method computed using Hoffman's criterion was applied to the FE models of incomplete coverage. The critical volume calculated from the joint with 0.25 mm thickness and a complete coverage with a failure load of 15.48 KN, was 8.72 mm<sup>3</sup>, which was chosen as the reference volume for calculating the failure loads of the other configurations. The reference volume is represented in Figure 5.21.



a)



b)

Figure 5.21. a) Contour showing distribution of solution variable and b) 3D view of the reference volume (Section A) used for calculating the failure loads using the Critical Zone method applying Hoffman`s criterion

It was found that the failure loads could not be predicted using the critical zone method because the criteria for critical volume were never met in either of the cases of incomplete adhesive distribution. To investigate the case further, a static stress analysis was performed using the 3D model used earlier in the current section for stress analysis.

The configurations with complete adhesive coverage ( $R$ ) having a failure load of 15.48 KN, elliptical coverage  $E1-2$  and elliptical coverage  $E1-3$  and circular shape ( $C2$ ) were used for the analysis. A load of 6000 N was applied since the failure loads of the configurations with incomplete coverage are slightly above 6000 N. The non-linear behavior of the adhesive was disregarded to have an estimate of the stresses in the adhesive without plasticity for a comparison of stresses in the bond line. The stresses were extracted from a path along the geometric center of the bond line, passing through the adhesive as shown in Figure 5.22.

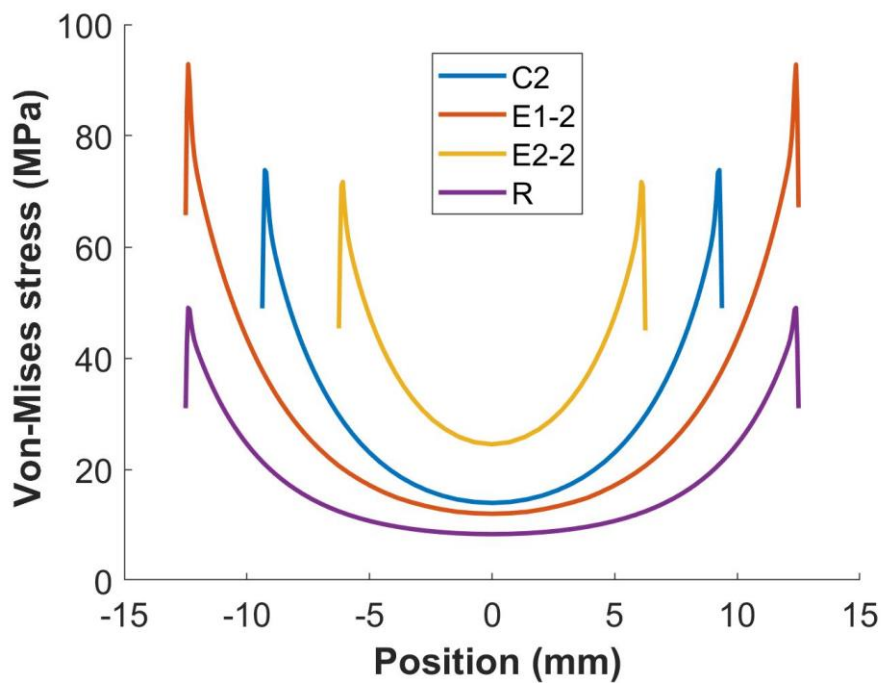


Figure 5.22. Comparison of Von-Mises stresses at the center of the bond line for various configurations

The average stresses measured along the overlap for the Circular ( $C2$  configuration), Elliptical ( $E1-2$  configuration), Elliptical ( $E2-2$  configuration) and the configuration with a complete coverage ( $R$ ) are 55.95 MPa, 45.26 MPa, 51.86 MPa and

25.57 MPa respectively. The joint configurations of *C2*, *E1-2* and *E2-2*, nearing their failure strengths at a 6000 N applied load in the FE model have average Von-mises stresses exceeding the failure strength of the adhesive of 42.16 MPa ,measured in Section 3.1.3.2. This shows that for the joint configurations with incomplete adhesive distribution, there is a stress re-distribution when compared with joints with complete adhesive coverage.

More accurate predictions of failure load can be performed by using a combination of cohesive zone modeling and critical zone methods similar to the work done by Kim, et al. [117] who used two separate UMATs each for the adherend and the adhesive the solution variables were plotted for each. The region which reaches the failure criteria first would be where the failure would instigate. This approach, which uses a combination of critical zone method and fracture mechanics, both of which being described in Section 2.3, would require further material characterization namely the fracture energies for the adhesive and the inter-ply fracture energies of the carbon fiber adherend, to predict failure.

In conclusion, the effect of incomplete adhesive distribution on the strength of bonded joints is presented in this chapter. The effect of incomplete adhesive distribution has not been addressed in the prior literature. An incomplete distribution of the adhesive may occur due to negligence of the operators or due to improper fixturing during the fabrication of bonded joints. Elliptical shape with two orientations and circular shape with three different size levels are investigated where the elliptical shape orientation is found to affect the failure strength of the bonded joints. The elliptical orientation with its major axis placed perpendicular to the loading axis (orientation 2) is found to have higher

load bearing capacity than the one whose major axis aligned with the loading direction (orientation 1). A stress analysis in the first ply of the adherend shows increased stresses for the orientation 1 as compared with orientation 2. The ultrasonic scans are able to detect and resolve the shape and size of the adhesive with the woven carbon fiber adherends while in the unidirectional carbon fiber adherents, increased signal attenuations may be the reason that the adhesive could not be detected. The strength of bonded joints with incomplete adhesive distribution could not be predicted using the Critical Zone method. The issue is possibly due to the load being re-distributed in the adhesive as the size of the adhesive reduces from a complete distribution. Further characterization of the adhesive for its fracture energies and a combined Cohesive Zone and Critical Zone method may provide acceptable failure strength predictions of bonded joints with incomplete adhesive distribution in future work.

## CHAPTER SIX

### Effect of Adherend Inclusions and Ply Orientations

Inclusions are common defects in laminated Fiber Reinforced Polymers (FRPs) which may occur due to improper fabrication procedures during the ply layup process [118]. Prior studies on defects in bonded joints have focused on defects present at the bond line or within the adhesive [56,59,119–122]. However when CFRP adherends are used, bond joint failures may initiate in the adherend within the first three plies closest to the adhesive interface [39,46]. Failures within the adherend near the adhesive interface are due to stress concentrations near the bond line interface of the joint as seen in Figure 6.1.

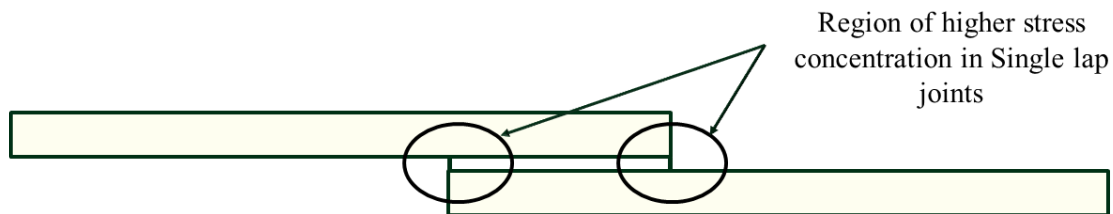


Figure 6.1. Regions of stress concentration in a Single lap joint

Failure within the adherends is more likely if inclusions occur between the layers of the adherends near the high stress regions as shown in Figure 6.1, during the fabrication process. If inclusion defects occur at or near the regions of high stress concentration in a bonded joint, they may compromise the joint strength integrity, causing a reduction in failure load of the bonded joints. The effect of inclusion defects in the adherend on the strength of bonded joints has not been addressed in the literature. The

aim of this study is to quantify the effects of the position of inter-layer inclusion defects between the first and second ply of the composite adherend adjacent to the bond line. Furthermore, the effects of interlayer inclusions with various ply orientations of the composite adherend are also considered.

## *6.1 Adherend Inclusions in a Unidirectional Composite*

### *6.1.1 Experimental Details*

To study the effect of adherend inclusions, laminated composite test coupons were fabricated in a manner similar to that described in Section 3.1.1. To simulate the presence of an inclusion within the adherend adjacent to the bond line, a PTFE film, 0.127 mm thick and 12.7 mm in width was placed between the first and second plies of the adherend during the wet layup process as shown in Figure 6.2. The width of the PTFE film was chosen based on a preliminary finite element study performed on the effect of the inclusion width on adhesive and adherend stress states, as discussed in Section 6.1.2. Simulations revealed no significant difference in the peak stress values over the range of different inclusion widths. The inclusion width of 12.7 mm was chosen so that the film could be easily handled during fabrication of the composite plates. PTFE films were chosen as the inclusion material since it does not interact with epoxy resin which bonds the laminated adherends [59]. Adherend coupons with inclusions were then used to fabricate single lap joint samples following the procedure described in Section 3.1.2. Lap joint test samples were fabricated where only one of the adherend coupons contained the inclusion defect while the other was defect-free as shown in Figure 6.3. The overall thickness of the adhesive in test specimens was maintained by inserting two PTFE strips

at both ends of the overlap during fabrication. Test locations for the imposed defect and the resulting failure loads are shown in Table 6.1. Lap shear tests were performed on the specimens using MTS Q-Test 100 (MTS Systems Corporation, Eden Prairie, USA) tensile testing machine (100 KN load cell) at a loading rate of 0.02 mm/sec. A total of 5 samples were tested for each test iteration.

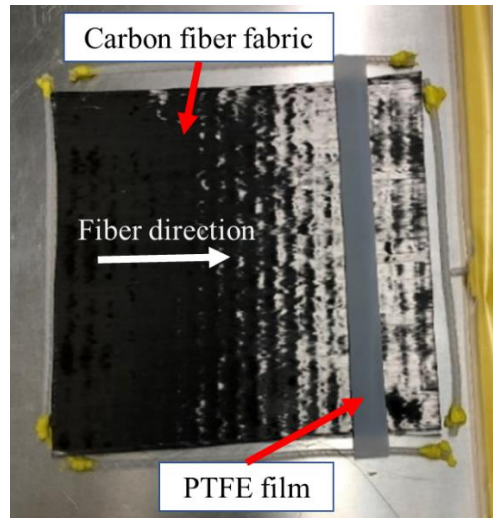


Figure 6.2. Insertion of PTFE strips to simulate inclusion defect during wet laying process between the first and the second layer of the laminate composite.

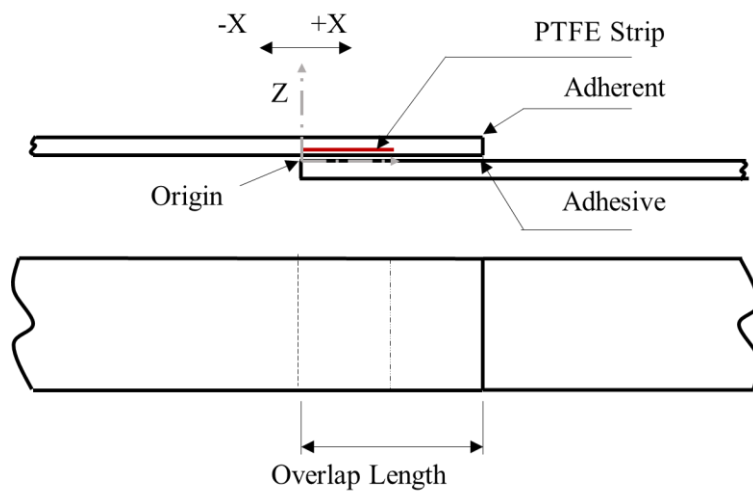


Figure 6.3. Location of PTFE inclusion in the joint assembly along with the position of the coordinate axes used for measurement of inclusion position.

Table 6.1. Experimental Plan and results (Position w.r.t origin as shown in Figure 6.3)

Position of the inclusion (mm)	Mean failure load (N)
$x$	
0	7.56±1.18
-6.25	9.78±2.34
-12.5	12.92±1.05
Non-defective	13.21±1.37

A light fiber tear failure was observed in all the adherend for all specimens tested with failure occurring in the first ply, close to the bond line as shown in Figure 6.4.

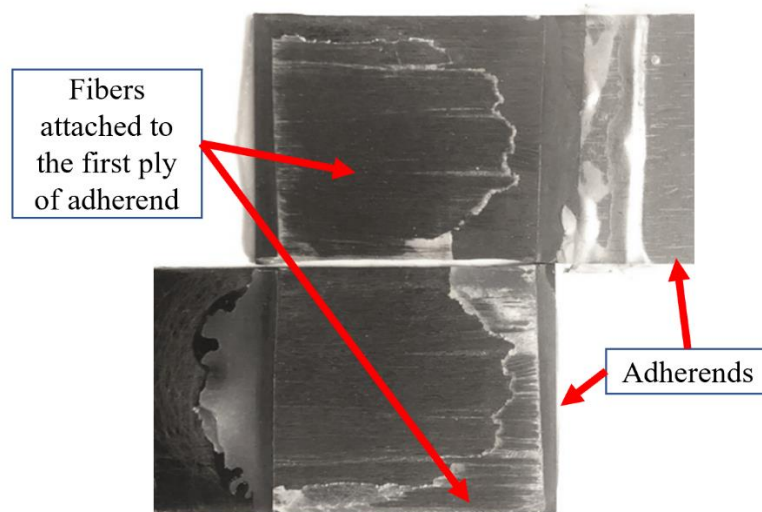


Figure 6.4. Image showing the failed surface exhibiting light fiber tear failure, for a non-defective joint.

The inclusion was placed at various positions of the overlap to study the effect of its position on strength of the bonded joint as indicated in Table 6.1. In all the cases the inclusion position was measured from the left-hand corner of the inclusion with respect to the origin defined. The non-defective configuration yields the highest failure strength as

expected. When the inclusion defect was introduced at the nominal position of  $x=0$  mm, the average failure load decreases by approximately 42%. This position yields the lowest strength among all other positions of the inclusion. When the inclusion was placed at the nominal position of  $x = -6.35$  mm, the average failure load decreases by 25% in comparison with a non-defective configuration. The defect nominal position of  $x = -12.7$  mm does not significantly affect the failure strength with an average reduction of 2.2%. Previously, researchers [54,56,96] have investigated the effect of size and position of inclusions in the bond line adhesive and found that inclusions placed towards the end of the overlap of single lap joints causes a reduction in failure loads because of the increase in the peel and shear stresses at the ends of the bonded joint. Similar reduction in strength is observed in the current study due to the presence of adherend inclusion defects near the ends of the overlap. The effects on shear and peel stresses due to the presence of inclusion defects have been investigated in the following section.

### *6.1.2 Numerical Analysis*

Finite Element modeling was performed using ABAQUS CAE to better understand the stress distributions in bonded joints and for predicting their failure loads. The Finite element model was built in two parts as shown in Figure 6.6. One part consisted of the bond line and the adherend plies adjacent to the bond line, while the other part was composed of the remaining plies. Both the parts were connected using a tie constraint. Since the PTFE inclusion introduced between the plies does not bond with epoxies [59], the plies do not bond at the interface where the inclusion is present. Thus, to simulate the presence of the inclusion, the location of the inclusion was not connected

using the tie constraint and a frictionless contact was specified between them to prevent material overlap under stress.

To assess the stress state of the bonded joints, stresses were evaluated along through a horizontal line through the middle of the first ply adjacent to the adhesive/adherent interface as shown in Figure 6.7. A minimum mesh size of 0.02 mm, appearing in Figure 6.5, was selected after performing convergence studies on the bonded joint. The region consisting of the first two plies and the adhesive was meshed using a finer mesh which was functionally graded to a coarser mesh towards the ends of the lap joint geometry. The stress analysis was performed by applying a constant load of 2000 N at the right end of the joint model while fixing the left end against motion in all directions as shown in Figure 6.7. The adhesive thickness has been designated using  $t_a$ .

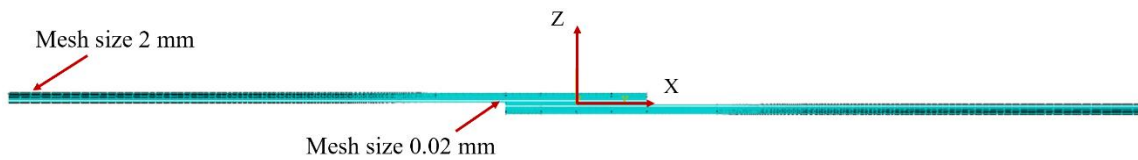


Figure 6.5. Mesh details of the model used for stress analysis.

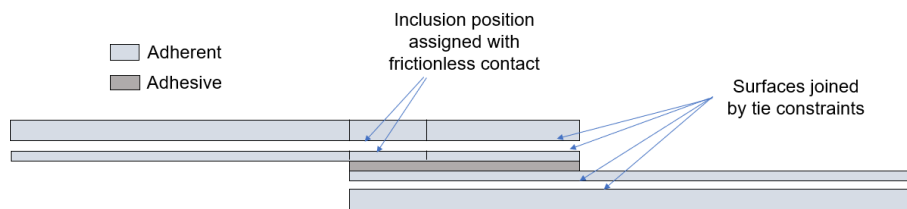


Figure 6.6. Schematic of Finite Element model

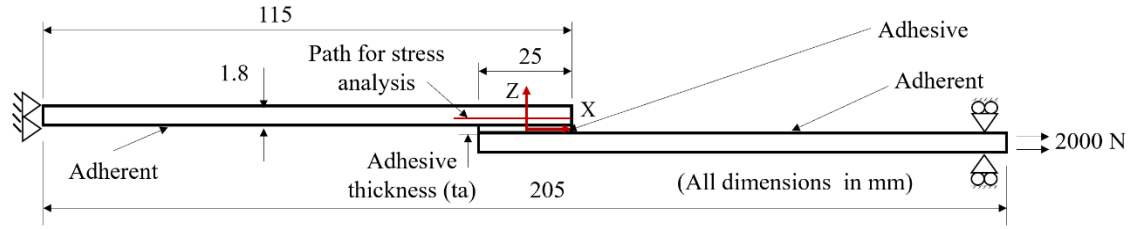


Figure 6.7. Path through middle of the first ply used to plot the stresses in the FE model.

The shear and peel stresses were extracted along a path defined through the mid plane of the first ply as shown in Figure 6.7, using the “Path” option in ABAQUS. All stresses were measured along the overlap length with the origin as defined at the top left corner of the overlap as shown in Figure 6.3.

The shear and the peel stresses were computed at the mid-line of the first ply closest to the bond line since failure occurred in the first ply in all the test cases. These shear and peel stresses appear in Figure 6.8 and Figure 6.9 respectively.

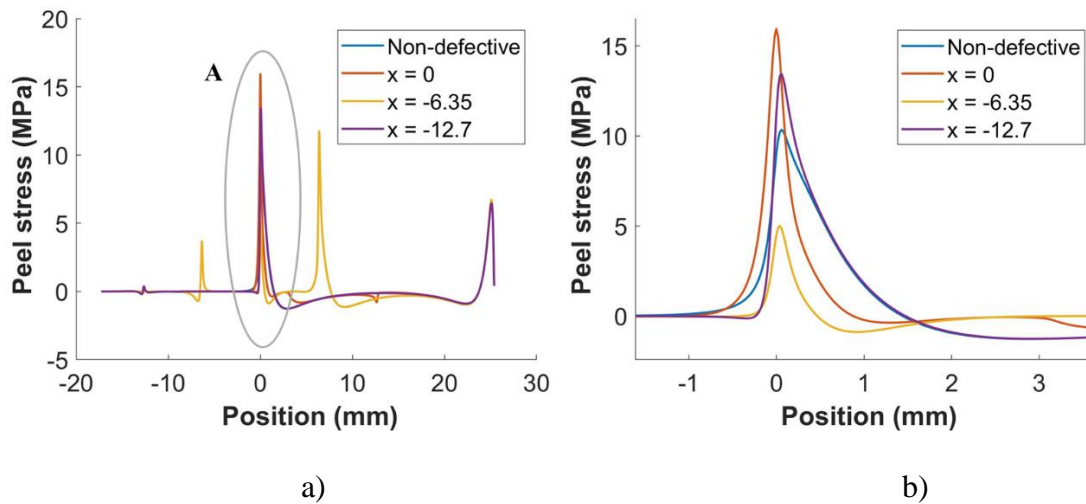


Figure 6.8. a) Peel stress distributions in the middle of first ply for various configurations b) magnified view of detail A

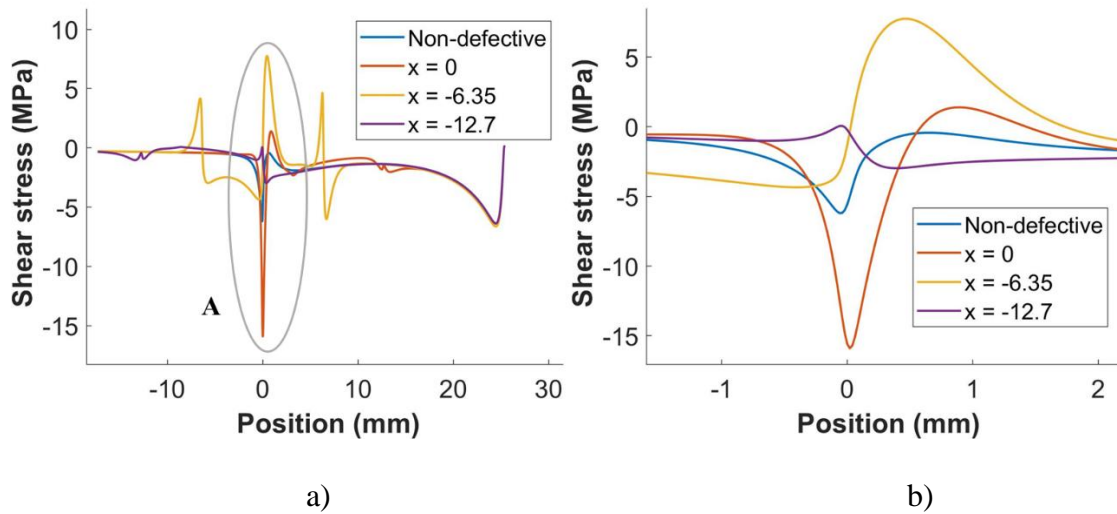


Figure 6.9. a) Shear stress distributions in the middle of first ply for various configurations b) magnified view of detail A

The peel and the shear stresses are the highest at 15.9 and 15.85 MPa respectively, for the nominal position of  $x = 0 \text{ mm}$  (see Figure 6.3). This correlates with the lower failure strength for a joint having the defect at this position. The nominal defect position of  $x = -6.35 \text{ mm}$  exhibits the next highest maximum shear stress at 7.73 MPa, but the maximum peel stress having a value of 5MPa is the lowest maximum peel stress among all the configurations. The vertical displacements of the first ply for each of the configurations studied are shown in Figure 6.10. All the other configurations exhibit similar values of vertical displacements except for the configuration of nominal position of  $x = -6.35 \text{ mm}$ , at the origin. The vertical displacement is approximately 50% greater at the inclusion at nominal position of  $x = -6.35 \text{ mm}$  position of the inclusion as compared with the other positions. The inclusion at  $x = -6.35$  is the same position where all the peel stresses peak as seen in Figure 6.8. The origin also corresponds to the maximum peel stress location for all the other configurations. The presence of the inclusion is expected to create a delamination between the ply adjacent to the bond line and the plies above it

as shown in Figure 6.11. The delamination (not evaluated here) would cause a relaxation of peel stress in the first ply for the nominal inclusion defect position of  $x = -6.35 \text{ mm}$ .

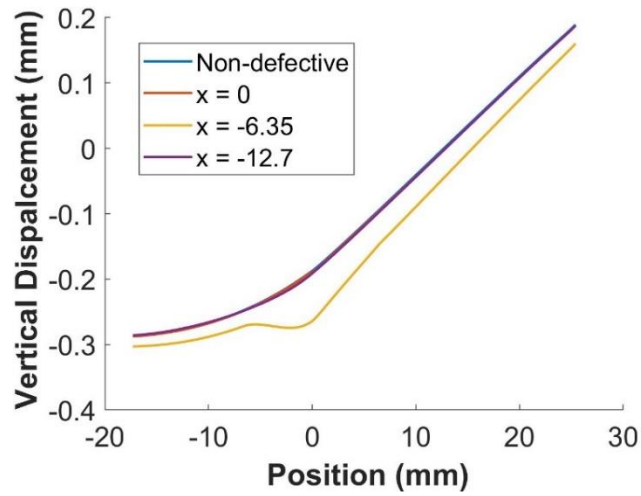


Figure 6.10. Vertical displacements of the first ply for various configurations

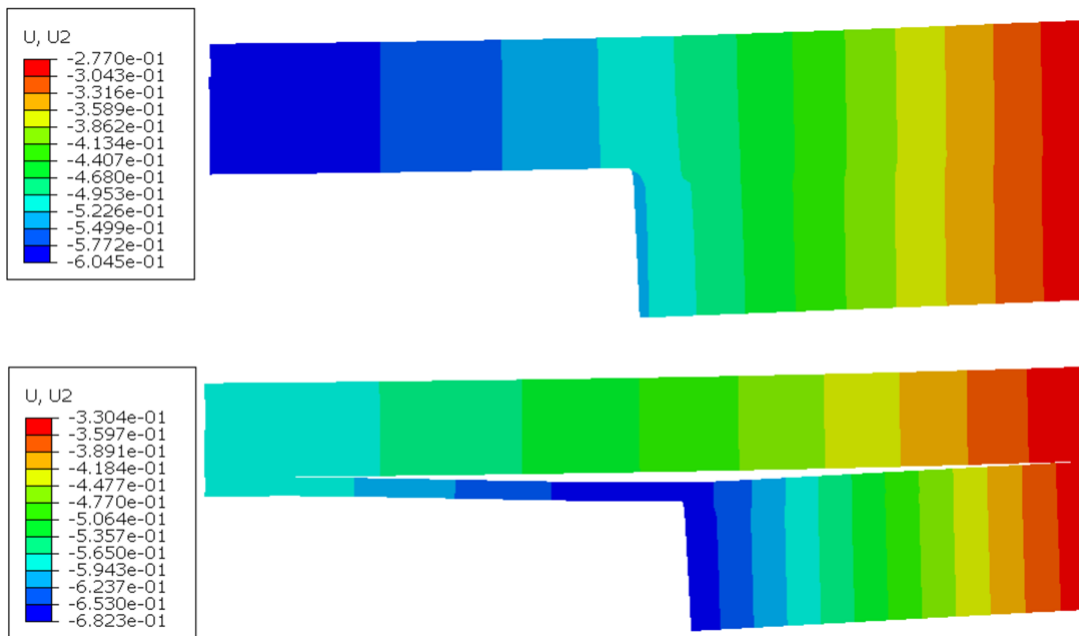


Figure 6.11. Vertical displacement ( $U_y$ ) contours for a) Defect position  $x = -6.35$  b) Non-defective joint

Figure 6.12 shows the shear stress distribution for the applied load of 2000 N for a joint having the inclusion nominal position of  $x = 0 \text{ mm}$ . The results indicate that there is no significant impact on the peak shear stresses developed due to variations in the inclusion width along the overlap.

Composite laminate failure was also evaluated using the Critical Zone method following the same procedure as discussed in Section 4.1.2. In this study, The Hoffman`s criterion was used to predict the failure loads. A comparison of the failure loads predicted using the critical zone method and the experimental values are shown in Table 6.2.

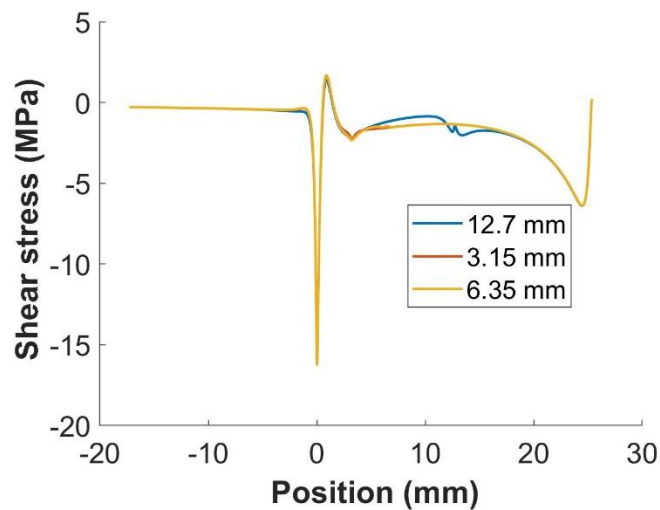


Figure 6.12. Comparison of shear stresses for various widths of inclusion at a position of the inclusion at  $x = 0$

Table 6.2. Experimental and Finite element failure load comparison

<b>Position of the defect x (mm)</b>	<b>Mean Experimental strength (KN)</b>	<b>Finite Element predictions using Critical zone method (KN)</b>
0	7.56±1.18	8.17
-6.35	9.78±2.34	9.27
-12.7	12.92±1.05	7.76
Non-defective	13.21±1.37	13.21 (Ref)

The Critical zone method using the Hoffman`s criterion is able to predict the failure load for the inclusion defect positions of  $x = 0$  and the  $x = -6.35 \text{ mm}$  configurations within an error margin of approximately 8% and 5% respectively, while the failure load for the nominal inclusion defect position of  $x = -12.7 \text{ mm}$  is incorrectly predicted with an absolute percentage error of approximately 40%. The reason for this anomaly may be the material discontinuities that are produced in the FE model with the introduction of the inclusion defect. The critical zone method relies on the estimation of the volume of a region near the point of onset of failure to predict failure [85]. In the case of bonded joints with interlayer inclusions, the method of modeling inclusions creates two points of stress singularity at each of its ends. Since these singularities are the artefacts of numerical stress computations, there may be an over- estimation of the critical volume, which in turn affects the accuracy of strength predictions. Alternatively, a fracture mechanics-based approach such as XFEM may be utilized in this case to estimate the bond failure strength. This would require further characterization of the adherends to estimate its fracture energy properties.

## *6.2 Study on the Effect of Adherend Inclusions with Various Ply Orientations*

It is well understood that ply orientations in laminated polymer composite affects the longitudinal bending stiffness of composite adherends [47]. Prior research has shown that the fiber orientation of the ply adjacent to the bond line has a significant effect on the failure load of the bonded joint [46,50,51]. Unfortunately, little is known about the effect of an inclusion defect position on bonded single lap joint strength. Section 6.1 presented the effect of inclusion defect position on single lap joint strength. It was shown that the failure load is least for an inclusion placed at the location of  $x = 0 \text{ mm}$ . The current section investigates the effect of the inclusions at the same position of  $x = 0 \text{ mm}$  for various ply orientations.

### *6.2.1 Experimental Details*

Laminate polymer composite test coupons having ply orientations  $[90/0]_3$ ,  $[45/0/-45]_s$ ,  $[45/90/45]_s$  and  $[90/45/0]_s$  were fabricated using the procedure described in Section 3.1. The individual plies having orientations of  $0^\circ$ ,  $45^\circ$  and  $90^\circ$  were cut into rectangular sheets of from a unidirectional fiber roll and were laid up in the sequence desired as shown schematically in Figure 6.13a. A PTFE film of 0.127 mm thickness and 12.7 mm width was placed between the first and second plies adjacent to the bond line as shown in Figure 6.13b in Section 6.1.1. Note that the first digit in each stacking sequence designates the orientation of the laminate ply adjacent to the bond line. The laminate polymer composite coupons with inclusions were then used to form the adherend in single lap joints which were fabricated using the procedure described in Section 3.1.2. Lap joint test samples were fabricated where only one of the adherend coupons contained

the inclusion defect while the other was defect-free. Each configuration with defect was compared with a non-defective test specimens to study the amount of failure load strength reduction due to the presence of the inclusion. Five samples each were fabricated for each of the configurations and lap shear tests were performed on each specimen using MTS Q-Test 100 tensile testing machine (MTS Systems Corporation, Eden Prairie, USA) (100 KN load cell) at a loading rate of 0.02 mm/sec.

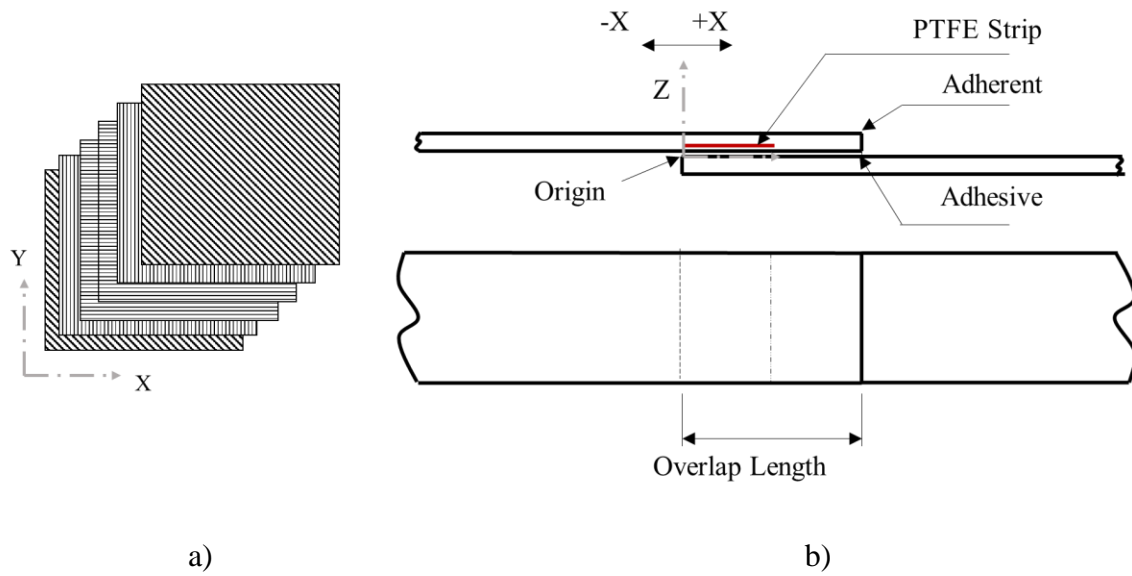


Figure 6.13. a) Schematic diagram showing stacking sequence in the adherend with layup along the out of plane Z axis b) Location of PTFE inclusion in the joint assembly

The bending moments produced in a composite laminate in a single lap joint test are related to the respective curvatures through [1].

$$\begin{bmatrix} M_x \\ M_y \\ M_z \end{bmatrix} = \begin{bmatrix} D_{11} & D_{12} & D_{16} \\ D_{12} & D_{22} & D_{26} \\ D_{16} & D_{26} & D_{66} \end{bmatrix} \begin{bmatrix} \kappa_x \\ \kappa_y \\ \kappa_z \end{bmatrix} \quad (6.1)$$

where:  $M_x$ ,  $M_y$  and  $M_z$  are the bending moments about X,Y and Z axes respectively  
 $\kappa_x$ ,  $\kappa_y$ ,  $\kappa_z$  are the curvatures about Z,Y and Z axes respectively

The bending stiffness matrix parameters  $D_{ij}$  were evaluated for each ply orientations using [1].

$$D_{ij} = \sum_{k=1}^n \overline{Q}_{ij} \left( t_k z_k^2 + \frac{t_k^3}{12} \right) \quad (6.2)$$

where:  $t_k$  is the thickness of the  $k^{\text{th}}$  ply  
 $z_k$  is the position of the  $k^{\text{th}}$  ply from the middle surface  
 $i, j = 1, 2, 6$   
 $\overline{Q}_{ij}$  are the components of the transformed reduced stiffness matrix.

The ply positions are defined as shown in Figure 6.14. If an external bending about the X axis was applied, the radii of curvatures about the Y- and the Z- axes are zero. The longitudinal bending moment  $M_x$  in Equation 6.1 reduces to

$$M_x = D_{11} \kappa_x \quad (6.3)$$

where, it can be seen that the bending moment is directly proportional to  $D_{11}$  for a given radius of curvature. In this research, values of  $D_{ij}$  are evaluated for each laminate orientation as appearing in Table 6.3.

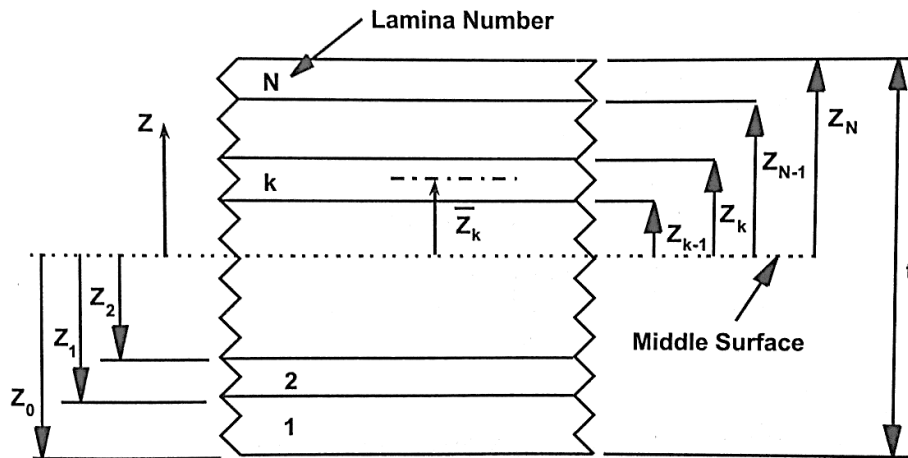


Figure 6.14. Ply position in a laminated composite [1]

Table 6.3. Comparison of experimental failure load and bending stiffness.

Stacking sequence	Mean experimental failure load (Non-defective) (N)	Mean experimental failure load (Defective) (N)	Bending stiffness of Non-defective composite adherend $D_{II}$
[0] <sub>6</sub>	13205.05	7568.94	6.21e+04
[90/0] <sub>3</sub>	6279.61	4119.59	3.45e+04
[45/0/-45] <sub>s</sub>	9502.34	4986.22	2.28e+04
[45/90/0] <sub>s</sub>	8069.82	4356.36	1.05e+04
[90/45/0] <sub>s</sub>	4856.24	3042.92	9.5e+03

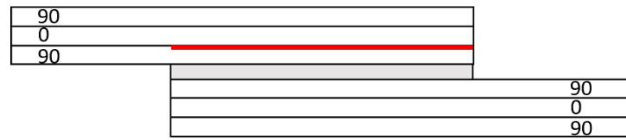
The results of the experimental lap shear tests are summarized in Table 6.3. Among the non-defective bonded joint specimens, the configuration with unidirectional composite adherends [0]<sub>6</sub> exhibits the highest failure load while the specimens with [90/45/0]<sub>s</sub> adherend configuration exhibits the least failure load. There is almost 60% decrease in failure load when the stacking sequence is changed from [0]<sub>6</sub> to [90/45/0]<sub>s</sub>. Additionally, for both defective and non-defective specimens, the bonded joints with adherends having the stacking sequence [45/0/-45]<sub>s</sub> and [45/90/0]<sub>s</sub> yield a higher failure load than those with a stacking sequence of [90/0]<sub>3</sub> and [90/45/0]<sub>s</sub>. These observations are consistent with results of the previous researchers who have shown that joints with higher angle plies closer to the bond line have lower strengths [47].

A comparison of the bending stiffness matrix coefficient,  $D_{II}$  shows that the [0]<sub>6</sub> configuration has the highest value of  $D_{II}$  while [90/45/0]<sub>s</sub> shows the least value. There is a reduction of approximately 85% in the value of  $D_{II}$  when the stacking sequence of the adherends is changed from [0]<sub>6</sub> to [90/45/0]<sub>s</sub>. For adherends with the 90° ply adjacent to the bond line there is a decrease of approximately 73% in the value of  $D_{II}$  when the adherend ply stacking is changed from [90/0]<sub>3</sub> to [90/45/0]<sub>s</sub>. This change is associated

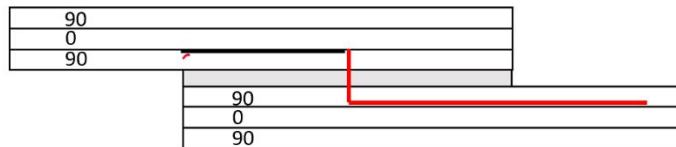
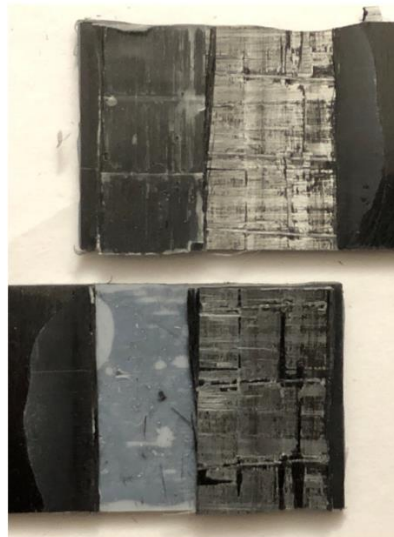
with an approximately 23% decrease in the failure load as compared to a bonded joint having adherends with a  $[90/3]_3$  layup. Similarly, there is an approximately 8% decrease in the failure load when the stacking sequence is changed from  $[45/0/-45]_s$  to  $[45/90/0]_s$  with the stiffness of  $[45/90/0]_s$  being approximately 53% less than that of  $[45/0/-45]_s$ .

For bond joints having an inclusion defect, a decrease in failure load is observed across all the configurations. The configuration with adherend ply stacking  $[45/0/-45]_s$  exhibits the highest decrease in failure strength of approximately 48%. The configuration with the adherend stacking  $[90/0]_3$  shows a 35% decrease in failure strength with the inclusion present as compared to the defect-free configuration.

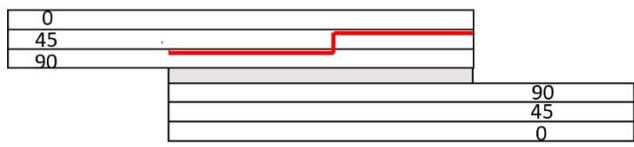
All single lap joint samples exhibit an interply adherend failure except for adherends with a  $[0]_6$  configuration which exhibit a light fiber tear failure. Figure 6.15 shows the images of the failed surfaces for the various layup configurations. The solid black line indicates the position of the inclusion while the red line indicates the path of failure.



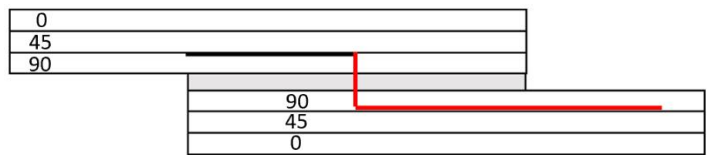
[90/0]<sub>3</sub> Non defective



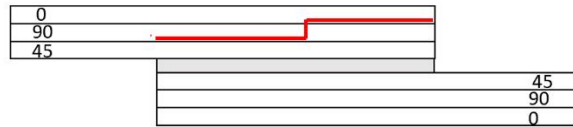
[90/0]<sub>3</sub> Defective



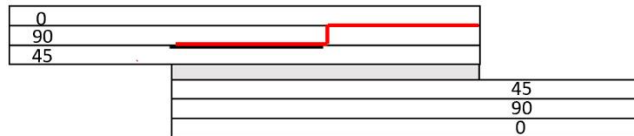
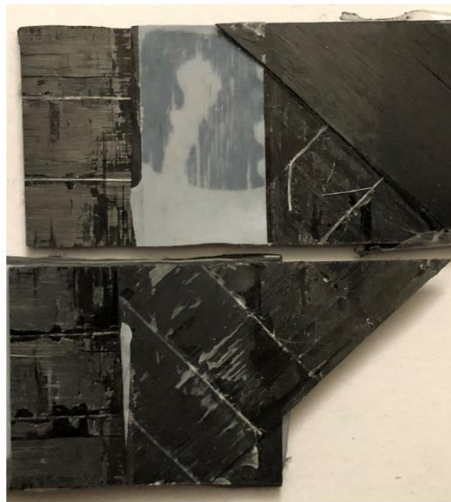
[90/45/0]s Non defective



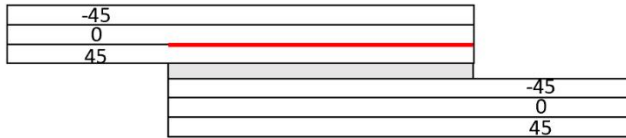
[90/45/0]s Defective



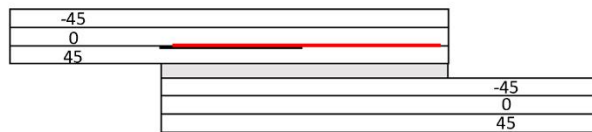
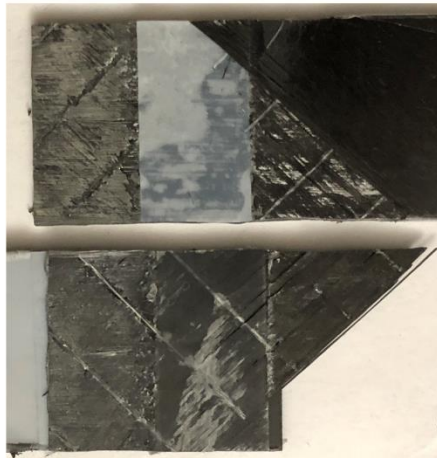
[45/90/0]s Non defective



[45/90/0]s Defective



[45/0/-45]s Non defective



[45/0/-45]s Defective

Figure 6.15. Failed surfaces for various layup configurations with and without defects.

In most of the non-defective joints, failure is localized in one of the adherends, with the failure following the interface of plies. One exception is for  $[90/45/0]_S$  and  $[45/90/0]_S$  which show the failed surface passing through the ply. The  $0^\circ$  ply stops the progression of failure through it and relegates it along a tangential path between the ply adjacent to it. In the bonded joint configurations where the  $90^\circ$  plies are located adjacent to the bond line, the inclusions cause the failure to propagate through the bond line into the other adherend. For the specimens with a  $45^\circ$  ply adjacent to the bond line, the failure propagates along the interface of the  $45^\circ$  and  $0^\circ$  ply when a  $0^\circ$  ply is located above it, meanwhile failure propagates through the  $90^\circ$  ply when it is placed above the  $45^\circ$  ply. This is consistent with observations by previous researchers [46,50] who also noted that the  $0^\circ$  ply stops the failure from propagating inside the composite. The same behavior is observed for the  $[45/0-45]_S$  and  $[45/90/0]_S$  configurations with the inclusion.

### 6.2.2 Numerical analysis

Finite element models were prepared in ABAQUS CAE to analyze stresses in the adherends and the adhesive. Each model was developed in two parts as shown in Figure 6.6 in Section 6.1.2. The model was also sub-divided into six partitions of 0.15 mm thickness to represent each ply layer as shown in Figure 6.16.

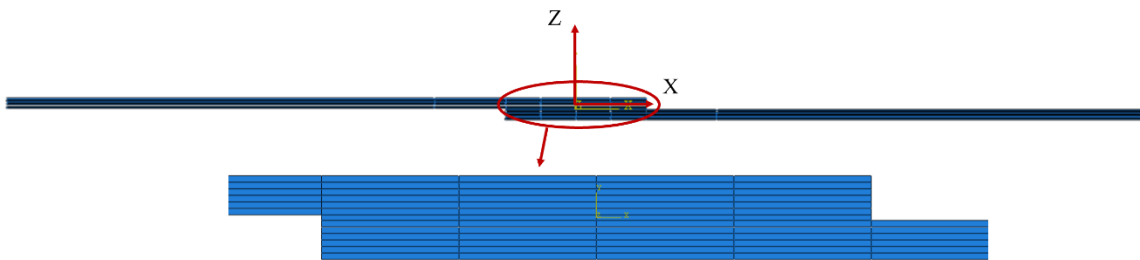


Figure 6.16. FE model used for stress analysis.

A fine mesh of element size of 0.02mm was used near the ends of the overlap which was graded to a coarser mesh of element size of 2 mm towards the ends of the joint model as shown in Figure 6.5 in Section 6.1.2.

A stress analysis was performed on the configurations used in this study by applying a tensile load of 2000 N at the unconstrained end of the model as shown in Figure 6.17. The adhesive thickness has been designated by  $t_a$ .

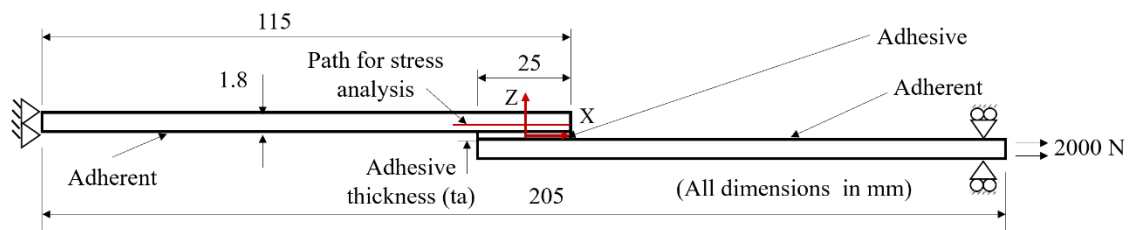


Figure 6.17. Paths used to plot the stresses in the FE model.

The peel and shear stresses were plotted along a path through the mid-plane of the first ply adjacent to the bond line as shown in Figure 6.17, for the non-defective configurations as appearing in Figure 6.18 and Figure 6.19 respectively. The magnitude of shear and the peel stresses are the highest for the  $[90/45/0]_S$  adherend stacking while the magnitudes are lowest for the adherend stacking of  $[0]_6$ . The increase in shear and peel stresses is consistent with the decrease in failure load observed when the adherend stacking changes from  $[0]_6$  to  $[90/45/0]_S$ .

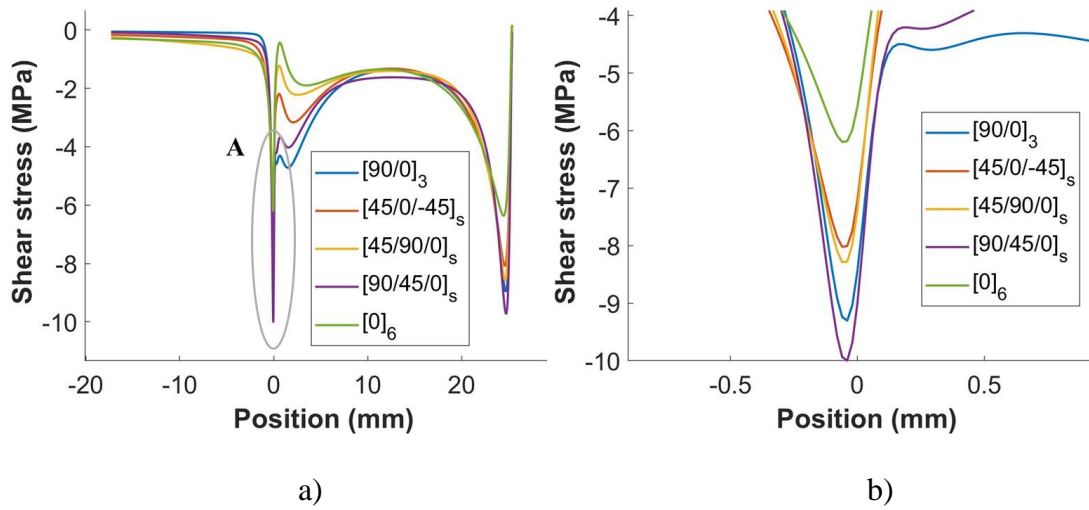


Figure 6.18. a) Shear stress distributions along the middle of the first ply adjacent to the bond line for the non-defective configurations b) magnified view of detail A

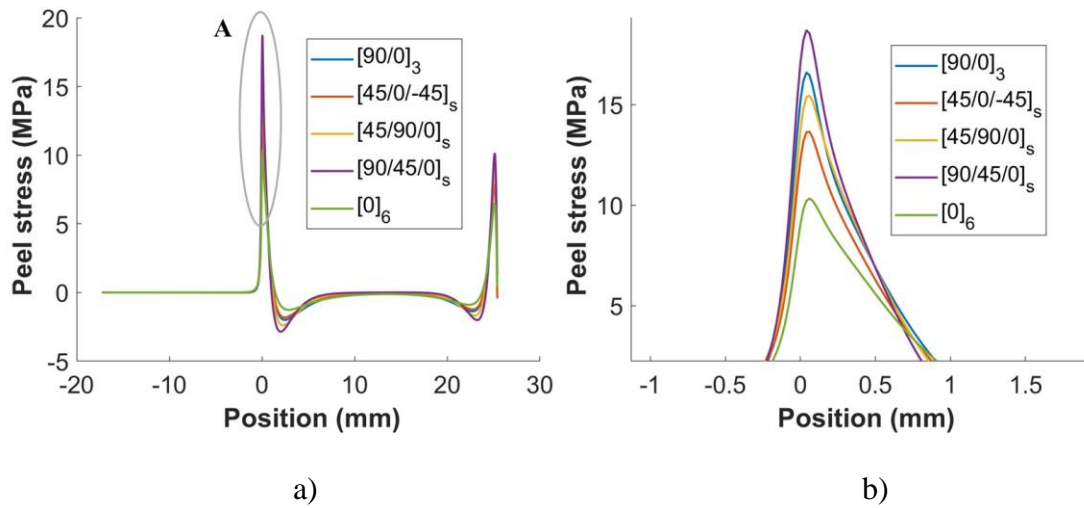


Figure 6.19. a) Peel stress distributions along the middle of the first ply adjacent to the bond line for the non-defective configurations b) magnified view of detail A

The stresses with the adherend stacking configuration  $[90/45/0]_s$  are greater than  $[90/0]_3$  with shear stress decreasing from 9.99 MPa to 9.31 MPa by approximately 7% while the peel stress decreases from 18.7 MPa to 16.6 MPa by approximately 64% respectively, which is consistent with a reduced failure strength observed for the

[90/45/0]<sub>s</sub> adherend stacking. The stresses with the adherend stacking configuration of [45/90/-45]<sub>s</sub> are greater than [45/0/-45]<sub>s</sub> with shear stress decreasing from 8.28 MPa to 8.02 MPa by approximately 3% while the peel stress decreases from 15.46 MPa to 13.66 MPa by approximately 12% respectively, which is consistent with a reduced failure strength observed for the [45/90/-45]<sub>s</sub> adherend stacking.

The peel and the shear stresses for the joints with inclusion defects are compared in Figure 6.20. and Figure 6.21. The shear and the peel stresses are the lowest for the adherend stacking of [0]<sub>6</sub> at 15.9 MPa and 15.49 MPa respectively, which is consistent with higher failure strength observed experimentally as summarized in Table 6.4 .The shear stress is highest at 20.45 MPa for the [90/0]<sub>3</sub> adherend stacking configuration while the peel stress is highest at 28.59 MPa for [90/45/0]<sub>s</sub> stacking configurations. The peel stress increases by approximately 8% from 20.45 MPa to 21.96 MPa while the shear stress increases approximately 7% from 17.84 MPa to 19.03 MPa, when the adherend stacking sequence changes from [45/0/-45]<sub>s</sub> to [45/90/-45]<sub>s</sub>.

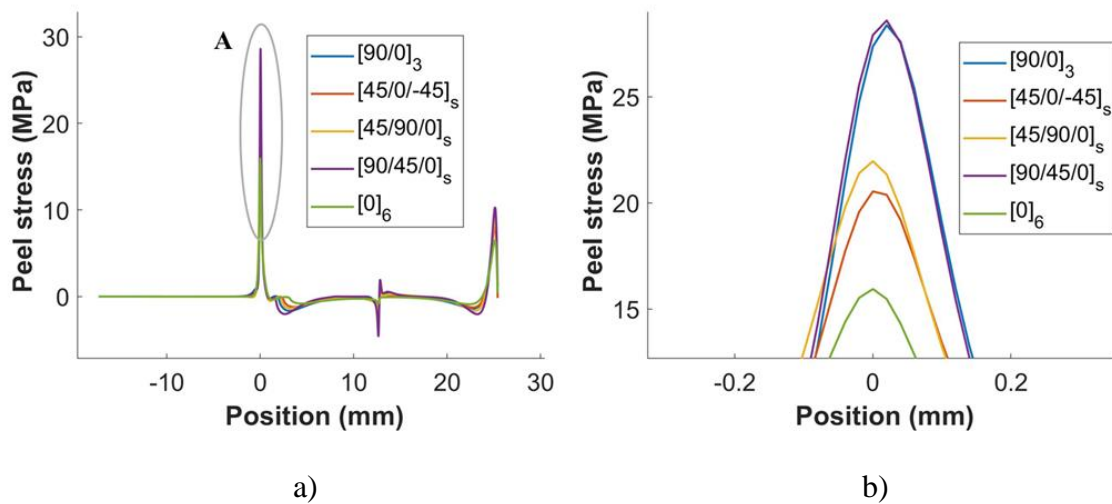


Figure 6.20. a) Shear stress distributions along the middle of the first ply adjacent to the bond line for the configurations with inclusion defect b) magnified view of detail A

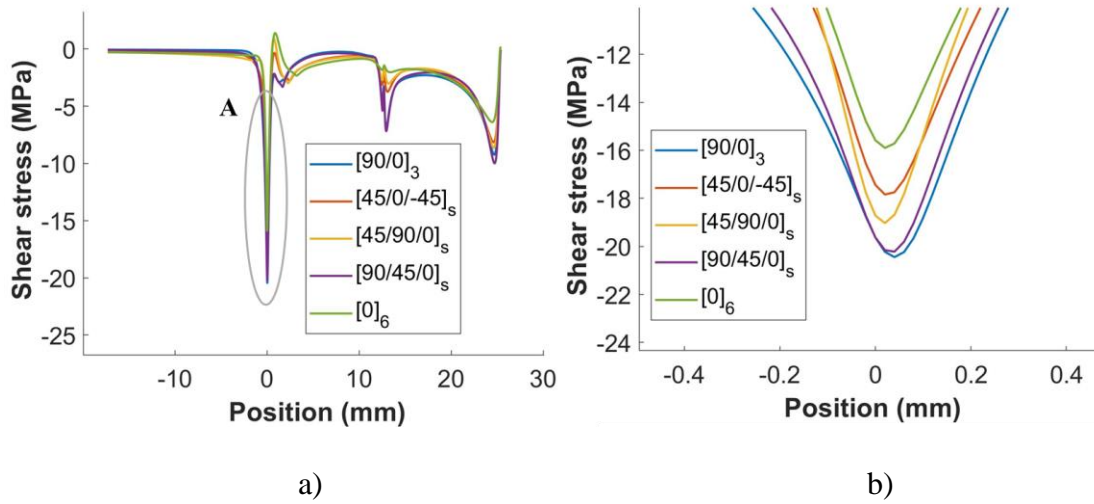


Figure 6.21. a) Peel stress distributions along the middle of the first ply adjacent to the bond line for the configurations with inclusion defect b) magnified view of detail A

Shear and peel stresses of the non-defective and defective adherends, are compared in the Figure 6.22 through Figure 6.25.

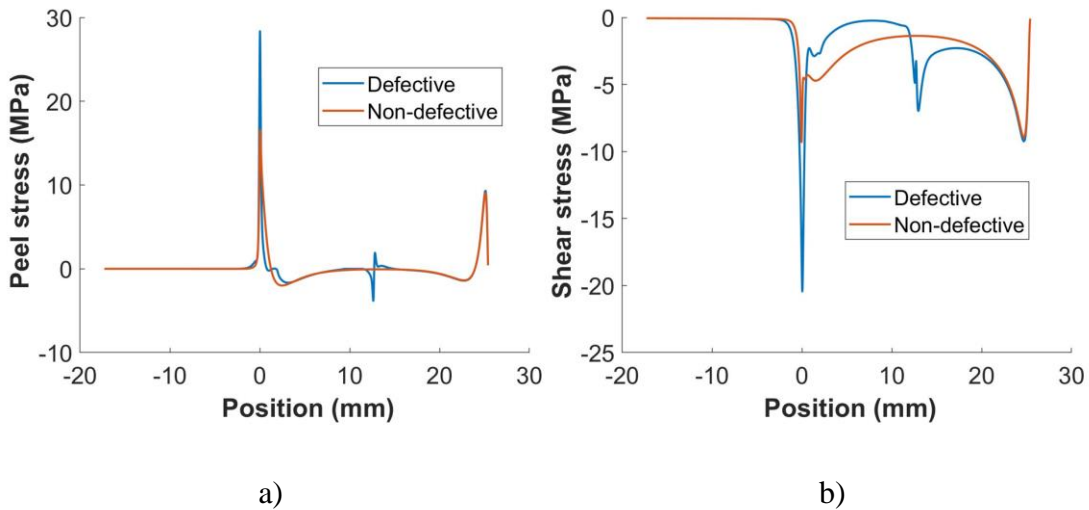


Figure 6.22. a) Peel and b) Shear stress comparison for  $[0/90]_3$  adherend stacking

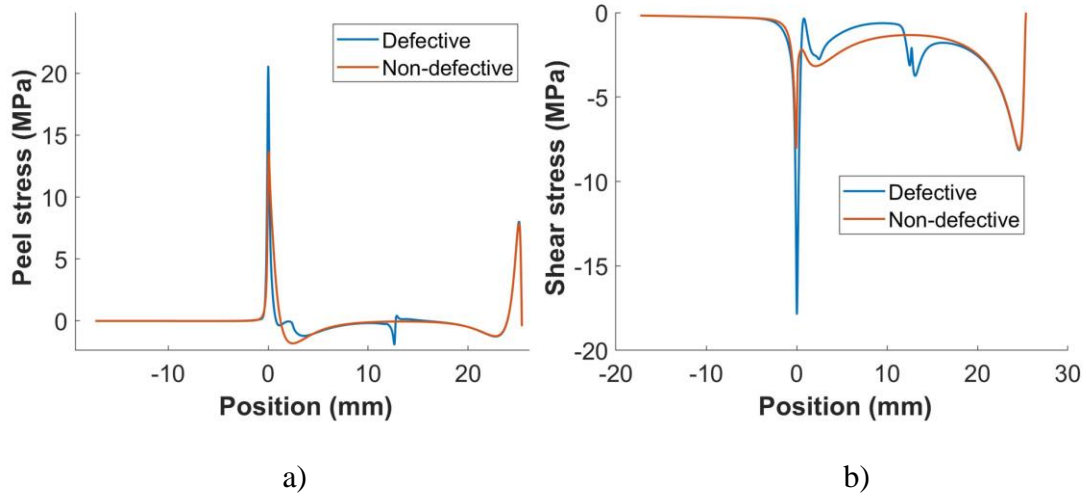


Figure 6.23. a) Peel and b) Shear stress comparison for  $[45/0/-45]_s$  adherend stacking

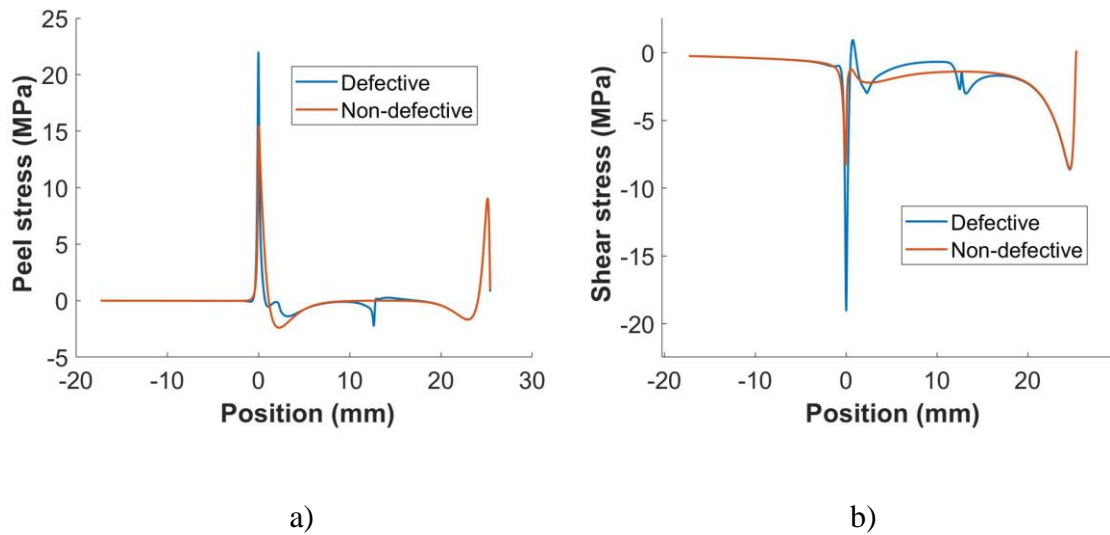


Figure 6.24. a) Peel and b) Shear stress comparison for  $[45/90/0]_s$  adherend stacking

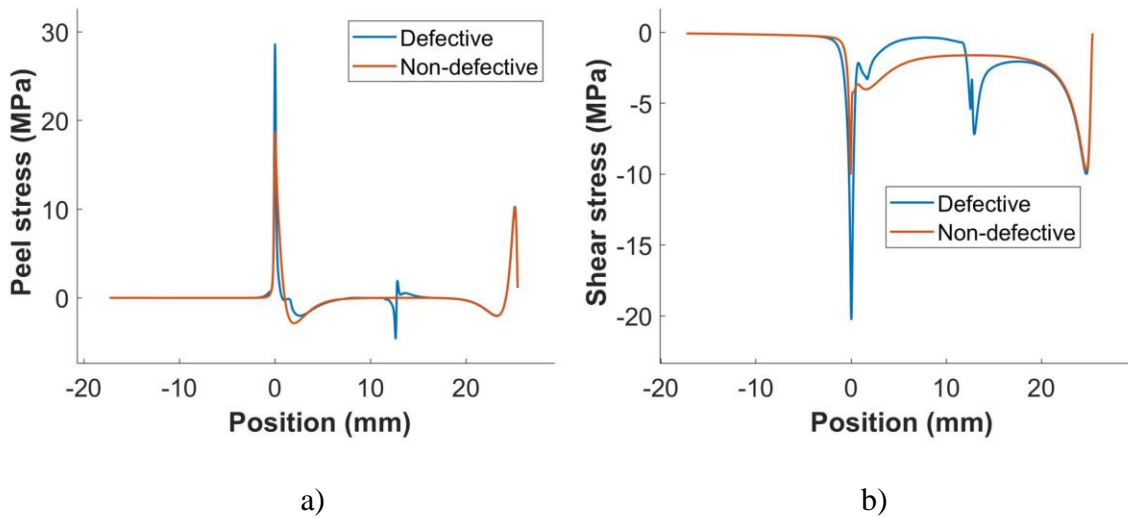


Figure 6.25. a) Peel and b) Shear stress comparison for  $[90/45/0]_s$  adherend stacking

The increase in the shear and the peel stresses due to the presence of an inclusion defect is summarized in Table 6.4.

Table 6.4. Percentage increase in shear and peel stress with different adherend stacking sequences due to presence of inclusion defect.

Stacking sequence	Increase in shear stress (%)	Increase in peel stress (%)
$[90/0]_3$	120	70
$[45/0/-45]_s$	121	50
$[45/90/0]_s$	130	43
$[90/45/0]_s$	102	53

The increase in shear stress due to the presence of an inclusion defect is highest at 130% for the adherend stacking of  $[45/90/0]_s$  while the increase in peel stress is highest at 70% for the adherend stacking of  $[90/0]_3$ . Unfortunately, the comparison of reduction in shear and peel stresses does not offer a clear picture regarding the reason behind the higher reduction in failure strength for the  $[45/90/0]_s$  adherend stacking. A progressive

damage model would have to be used for understanding this reduction in failure strength, which would capture the stress re-distributions with the progress of cracks in the adherend.

Figure 6.26 shows the distribution of peel and shear stress at the center of the bond line across the overlap length for defective joints. There is an increase in the peel and the shear stresses for  $[90/0]_3$  and  $[90/45/0]_s$  configurations at the center of the overlap length. This corresponds to the failure passing through the bond line to the other adherend in these configurations as shown in Figure 6.15.

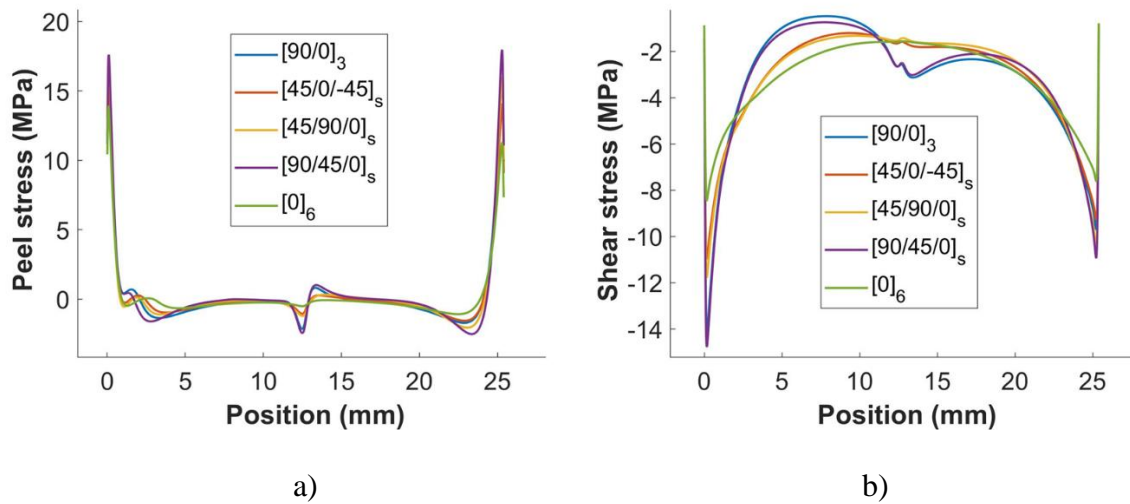


Figure 6.26. a) Peel and b) Shear stress distributions at the center of the bond line across the overlap length for defective joints

Failure prediction for the various configurations with a varying ply orientation could not be performed using the Critical zone method. The Critical zone method has been shown to be effective when intra-ply failure is observed [85] as seen with  $0^\circ$  unidirectional composites, described in Section 4.1.2. Note that, inter-ply failures were observed in all the other configurations having varying ply orientations as shown in

Figure 6.15. Hence for the strength prediction of bonded joints with varying ply orientations, an approach using cohesive surface elements between the plies and using a continuum based cohesive element for the adhesive, implemented in a Cohesive Zone Model approach is expected to be able to predict the failure of the configurations with the other ply orientations. This would need further characterization of the adherends to estimate their inter-ply fracture characteristics.

Interlayer inclusion defects in adherends may likely occur due to negligence during adherend fabrication process. The effect of inclusion defects in the adherends have not been addressed in the literature. The current study addresses the effects of inter-layer inclusions on the strength of single lap bonded joints. Inclusions present within the overlap region with one of the ends above the corner of the overlap, cause the greatest reduction in failure strength for unidirectional composites. Numerical analysis reveals an increase in the shear and peel stresses due to the presence of the inclusion defects at this position. Failure prediction using the Critical Zone method is able to predict the failure load for the defect positions inside the bond overlap but not for the defect position outside of the overlap region. This may be due to over-estimation of the critical volume, due to the presence of singularities at the ends of the discontinuities in the FE model, introduced to simulate the inclusion defects. The effect of interlayer inclusions in adherends with different ply stacking is also investigated. The ply orientation is found to influence the magnitude of reduction in failure strength for joints with inclusion defects. A 48% reduction in failure strength is observed for the adherend stacking of  $[45/0/-45]_s$  due to the presence of inclusion defects. Failure prediction could not be performed on the bonded joints with varying ply orientations, using the Critical Zone method since inter-

ply failure is observed in all the specimens. A FE model incorporating a progressive damage approach would be expected to better predict the failure loads more accurately.

## CHAPTER SEVEN

### Effect of Adhesive Thickness Variations in Strap Joints

#### *7.1 Study on Constant Bond Line Thickness*

Patch repairs are used for repairs made on fuselage structures of aircrafts [123]. Patch repair joints are structurally similar to strap joints [124]. A strap joint consists of a single or double strap made of either a metallic or a composite material to join the adherends together. Bond line thickness is one of the critical parameters, which influences the strength in strap joints. The strength of strap joints typically decreases with an increase in the bond line thickness [125]. Linear variation in bond line thickness can occur in strap joints due to improper fabrication techniques and has not been addressed in the literature. Bond line thickness imperfections could affect the joint integrity and strength of patch repairs. This chapter investigates the effects of bond line thickness variations on the strength of single strap bonded joints. The critical zone method along with the various criteria are used for estimating the failure load of the single strap joint. The validated FE model is then used on a single strap joint with a linearly varying bond line thickness to investigate the effects of such a variation on the joint strength.

##### *7.1.1 Experimental Details*

Test coupons for the single strap joints were fabricated using the procedure described in Section 3.1.1. The schematic diagram of the single strap joint is shown in Figure 7.1. The displacement applied at the right end of the model has been designated using  $u_x$ .

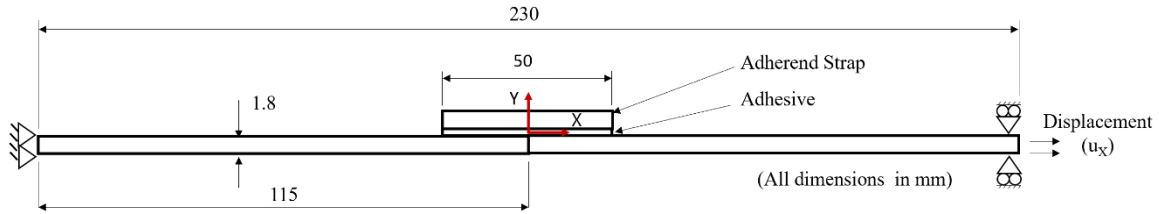


Figure 7.1. Schematic of a single strap joint used for the study.

The two adherend test coupons were joined using a single strap having the same fiber orientation as the test coupons. To maintain the same load transfer area between the adherends, for a comparative study with a single lap joint, an overlap length of 50mm was chosen. A similar bonding procedure was used for fabricating the single strap joints as described in Section 3.1.2. The fabrication fixture shown in Figure 3.2 in Section 3.1.2 was used for fabricating the strap joints as shown in Figure 7.2 The two adherends were laid on the fixture plate and the straps were placed over the ends of the two adherends.

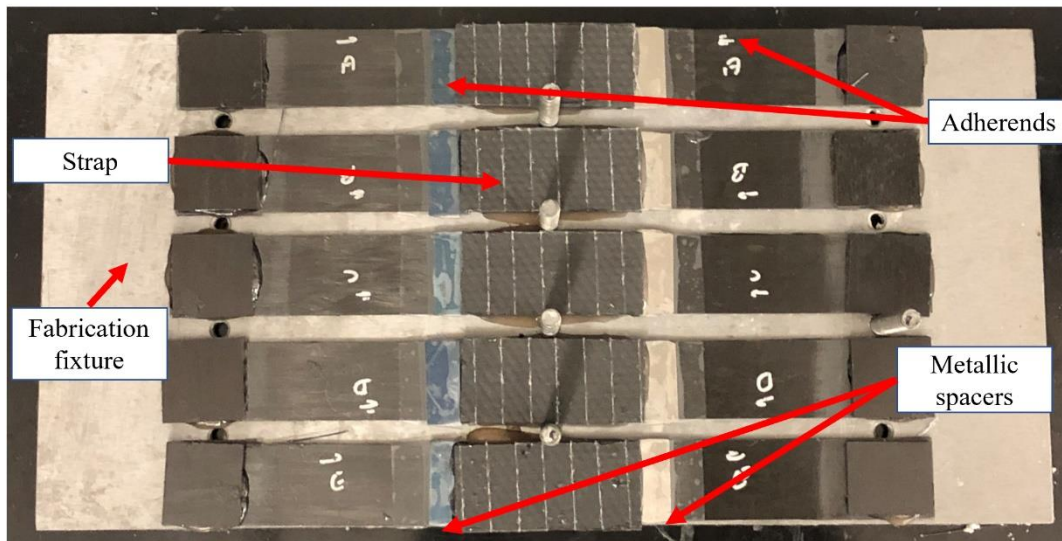


Figure 7.2. Fabrication of single strap joint in the fabrication fixture

For the experimental study of bond line thickness variations, metallic spacers of 0.25, 0.5, 0.75 and 1.00 mm were placed at each end of the overlap. The bond-line thickness of the bonded specimens were measured using the Keyence VR3100 3D microscope (Keyence corporation, Itasca, Illinois, USA) as shown in Figure 3.5 in Section 3.1.2. Images of the bond line showed that there was a deviation in thickness from the target values in the single strap specimens. The average bond line thickness was measured and recorded and was used for further analysis as shown in Figure 7.3. A gap between the adherends being joined is also seen in the Keyence microscope image at the middle of the strap joint. The gap occurs due to the end faces of the adherends not being perfectly straight along the width. The adhesive flows in to fill this gap. Tensile tests were performed on all the test specimens on the Instron 3382A tensile testing machine (Instron USA, Massachusetts, USA), having a load cell rating of 100 KN, at a displacement-controlled loading rate of 0.05 mm/min as described in Section 3.1.2.

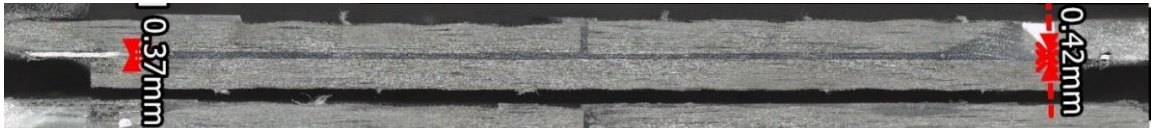


Figure 7.3. Bond line thickness measurement using a Keyence microscope.

The experimental test results are plotted in Figure 7.4. The failure load decreases by approximately 32% with an increase in the bond line thickness, similar to what is seen in single lap bonded joints. The data points were fit with a second-degree polynomial, which yields a correlation coefficient of 0.82. The curve fit equation is given as

$$P = 0.2151t^2 - 3.667t + 8.874 \quad (7.1)$$

where:  $P$  = Applied load (N)  
 $t$  = Bond line thickness (mm)

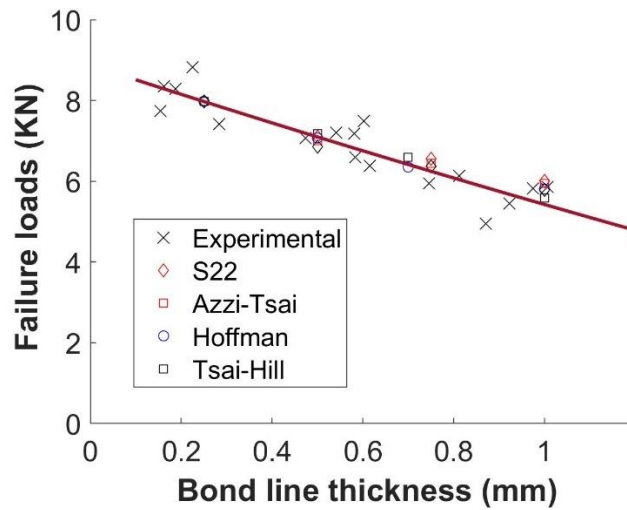


Figure 7.4. Experimental and FE predictions of failure loads for a single strap joint with varying constant thickness

A light fiber tear adherend failure was observed in the straps of all the specimens tested as shown in Figure 7.5.

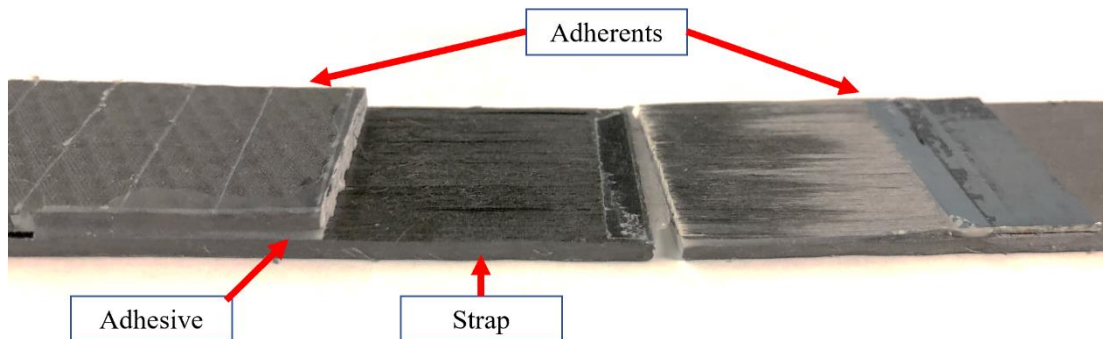


Figure 7.5. Failed surface of a single strap joint

### 7.1.2 Numerical Analysis

A 2D finite element model was prepared for the analysis of stresses and failure predictions. The model was meshed with elements of size of 0.02 mm at each end and the

middle of the overlap in the bonded region, which was graded to elements of 2 mm size towards the end of the joint, as shown in Figure 7.6.

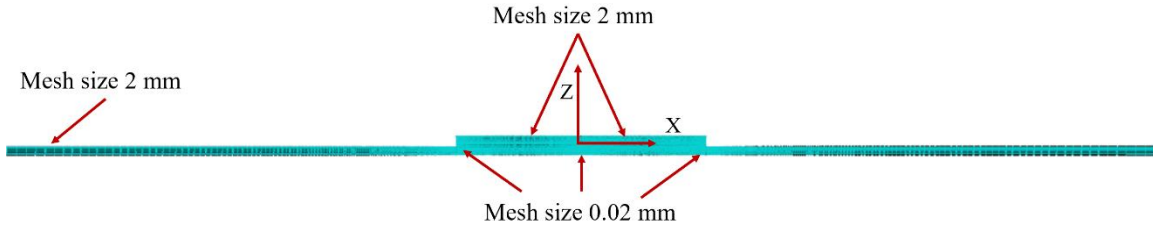


Figure 7.6. Mesh details of a single strap joint model

The left end of the specimen was fixed against translation while the right end was free to move in the  $X$ -direction as per the boundary conditions shown in Figure 7.1 . A tensile load of 2000 N was applied to the right end of the model for stress analysis. Models were made for joints having bond line thickness of 0.25, 0.5, 0.75 and 1.00 mm. The peel and shear stress contours for the applied load of 2000 N and a bond line thickness of 0.25 mm are shown in Figure 7.7 and Figure 7.8 respectively.

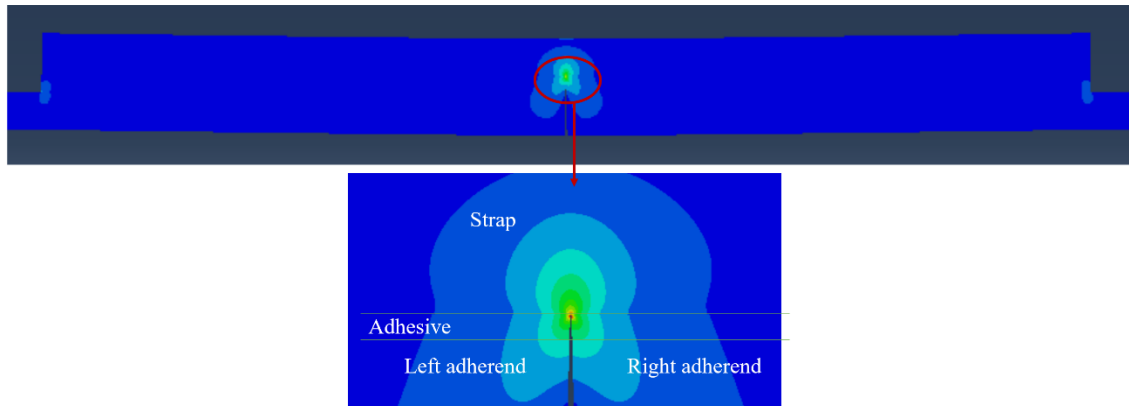


Figure 7.7. Peel stress contour in the bonded region

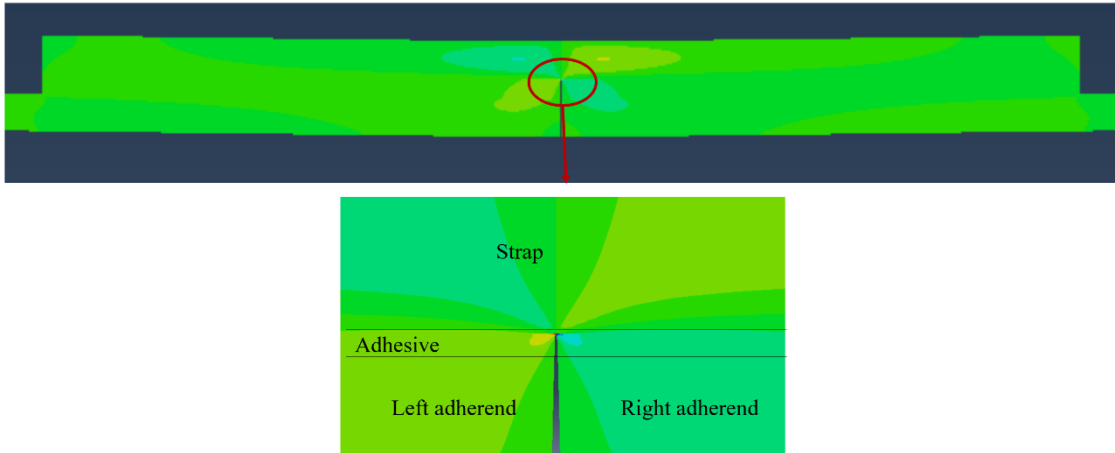


Figure 7.8. Shear stress contour in the bonded region

The stress contours show a higher stress concentration in the adhesive region at the middle of the bonded joint which is similar to the observations of previous researchers [126,127]. This indicates the failure of the joint would initiate at this location, which is similar to the observations made by Hart-Smith [128].

The shear and the peel stresses were plotted along a path passing through the middle of the first ply of the strap as shown in Figure 7.9. This location was chosen since a light fiber tear failure was observed in all the specimens in the first ply adjacent to the bond line as shown in Figure 7.5.

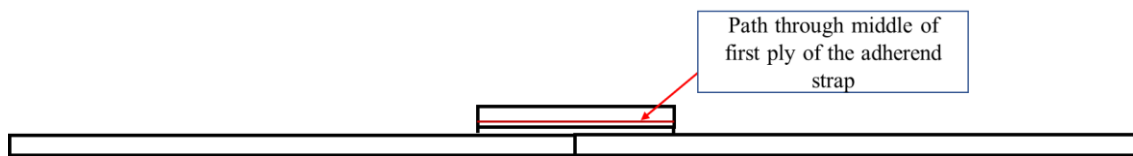


Figure 7.9. Path defined in the model for plotting of shear and peel stress.

The shear and the peel stress plots for the first ply are as shown in Figure 7.10 and Figure 7.11.

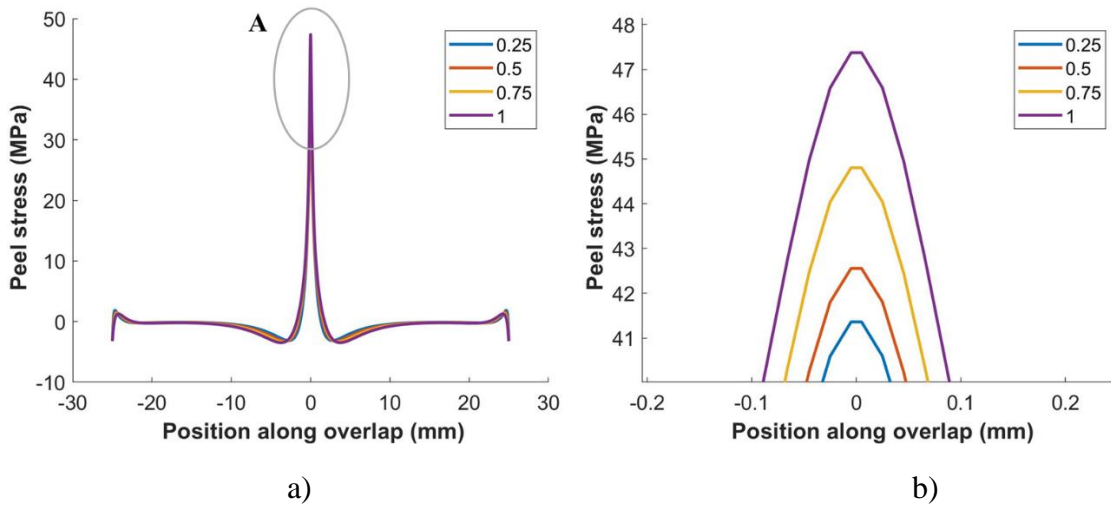


Figure 7.10. a) Peel stress distribution along middle of first ply closest to the bond line  
 b) Magnified view of detail 'A'

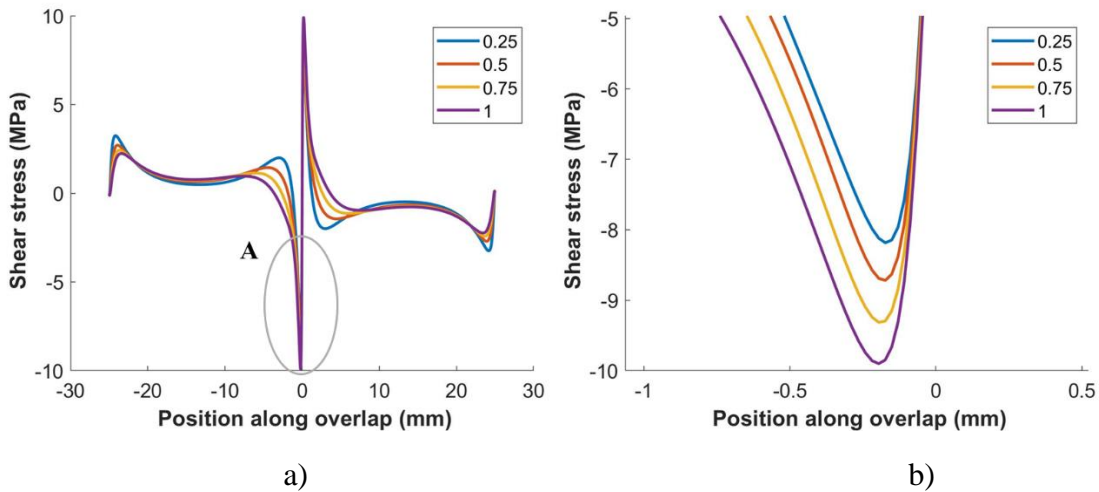


Figure 7.11. a) Shear stress distribution along middle of first ply closest to the bond line  
 b) Magnified view of detail 'A'

The position along the overlap in Figure 7.10 and Figure 7.11 was measured with the origin being at the geometric center of the single strap joint as shown in Figure 7.6. The shear and the peel stresses increase as the bond line thickness increases. Lee, et al. [125] observed the same trend with double strap joints with increasing bond line

thickness. The maximum shear and peel stresses along with the calculated failure loads for the bond line thickness 0.2, 0.5, 0.75 and 1.00 mm are shown in Table 7.1. The failure loads were calculated using the curve fit equation, Equation 7.1 in Section 7.1.1

Table 7.1. Comparison of stresses and failure loads

<b>Bond line thickness (mm)</b>	<b>Maximum Shear stress (MPa)</b>	<b>Maximum Peel Stress (MPa)</b>	<b>Calculated failure load (KN)</b>
<b>0.25</b>	8.184	41.36	7.974
<b>0.5</b>	8.719	42.56	7.097
<b>0.75</b>	9.314	44.8	6.2478
<b>1.0</b>	9.901	47.37	5.425

The shear stresses increase from 8.96 MPa to 10.73 MPa by approximately 20% while the peel stress increase from 24.35 MPa to 39.58 MPa by 63% as the bond line thickness increases from 0.25 to 1 mm. The increase in bond line thickness is also associated with approximately 32% decrease in the failure loads. On comparison of the single strap joint with a single lap joint having the same effective bonding area, a large reduction is seen in the failure loads when compared to a single lap joint as shown in Table 7.2. The failure loads were calculated using the curve fit equations, Equation 7.1 in Section 7.1.1 and Equation 4.1 in Section 4.1.1.

Table 7.2. Comparison of failure strength of Single lap and Single strap joints

<b>Bond line thickness (mm)</b>	<b>Single lap joint (KN)</b>	<b>Single strap joint (KN)</b>	<b>Difference (%)</b>
<b>0.25</b>	15.48	7.98	48.5
<b>0.5</b>	12.51	7.1	43.4
<b>0.75</b>	10.32	6.25	39.5
<b>1.0</b>	8.92	5.45	39.2

The single lap joint exhibits a higher failure load for the same bond line thickness and effective bonding area. A major reason for the reduction in failure load of the Single strap joints is the huge stress spike at the middle of the joint, which acts like a stress concentration [128].

Failure load predictions were performed using the “Critical Zone method” as described in Section 4.1.2. The model with 0.25 mm bond line thickness was chosen as the reference model to establish the reference volume for the analysis. The reference volumes calculated using the Maximum stress, Azzi-Tsai, Hoffman`s and the Tsai-Hill criteria given by equations Equation 2.1, 2.2, 2.3 and 2.4 in Section 2.3.2 are summarized in Table 7.3.

Table 7.3. Reference values of volumes used for strength prediction.

<b>Criterion used</b>	<b>Reference Volume for 0.25 mm thick joint (mm<sup>3</sup>)</b>	<b>Bond line Thickness 0.5 (mm)</b>	<b>Bond line Thickness 0.75 (mm)</b>	<b>Bond line Thickness 1.0 (mm)</b>
Maximum Peel Stress	44.85	7.1	6.53	6.01
Yamada-Sun	49.17	7.01	6.45	5.95
Azzi-Tsai Norris	59.14	7.07	6.35	5.81
Hoffman`s	43.62	7.18	6.6	5.69
Tsai-Hill	50.75	6.85	6.37	5.78
Experimental	--	7.1	6.25	5.45

The average absolute percentage error is 4.9%, 4.54%, 2.87%, 3.7% and 3.83% for Max Peel stress, Yamada Sun, Azzi-Tsai Norris, Hoffman`s and Tsai-Hill`s criteria respectively.

## 7.2 Study on Variable Bond Line Thickness

The previous section considered a single strap joint with uniform bond line thickness. However, imperfections in the fabrication procedure can produce a variation in thickness of the bond line which may affect the failure load of strap joints. The current section investigates the effects of linear variations in bond line thickness of single strap joints.

### 7.2.1 Experimental Details

The test coupons for the study on varying bond line thickness in single strap joints were fabricated using the same procedure as described in Section 3.1.1. A schematic diagram of a typical test specimen is as shown in Figure 7.12. The displacement applied at the right end of the model has been designated using  $u_x$ .

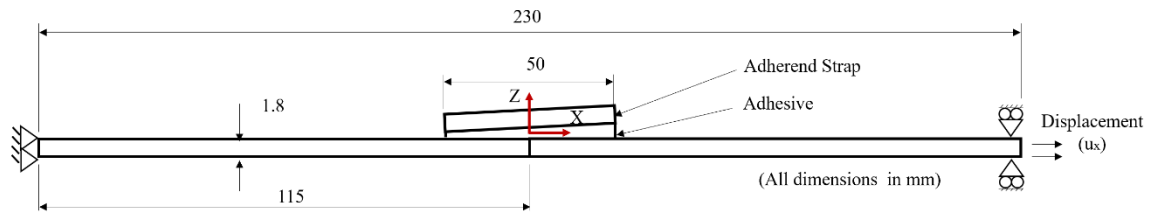


Figure 7.12. Schematic of a single strap joint with varying bond line thickness

The single strap joint test specimens were prepared using a similar procedure as that described in Section 7.1.1. above, except for the placement of metallic spacers of unequal thickness at each end of the strap. A minimum thickness spacer of 0.25 mm was placed at one end while a maximum thickness spacer of 0.5, 0.75 and 1.00 mm were placed at the opposite end depending on the desired configuration. Similar to the case with the constant bond line single strap joints and single lap joints, bond line thickness could not be maintained at its intended target values during fabrication. Additionally, some of the

coupons had to be discarded due to errors in fabrication, since the fixture used for fabrication was intended for single lap joints. The thickness of the specimen was measured at its cross-section, at the ends and the center of the bonded joint, using a Keyence VR3100 3D microscope (Keyence corporation, Itasca, Illinois, USA) as shown in Figure 7.13.

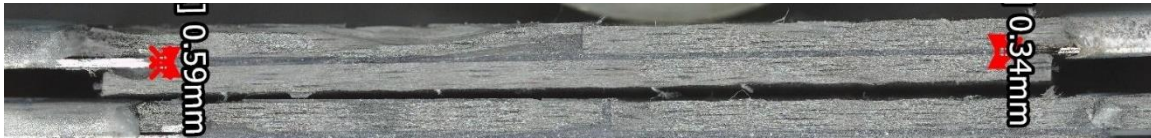


Figure 7.13. Cross-sectional image of single strap joint with varying bond line thickness

Lap shear tests were performed on all the test specimens on an Instron 3382A tensile testing machine (Instron USA, Massachusetts, USA), having a load cell rating of 100 KN, at displacement-controlled loading rate of 0.05 mm/min as described in Section 3.1.2.

A total of 5 test specimens were fabricated for three sets of thickness variation namely from 0.25 mm minimum thickness to a maximum thickness of 0.5, 0.75 and 1.00 mm. Out of these 15 samples, 7 were found to be satisfactory, while the other seven had to be discarded due to irregularities in joint fabrication as mentioned earlier. The bond line thickness measured using the Keyence microscope and the respective failure loads for the 7 samples tested for lap shear are listed in Table 7.4.

Table 7.4. Measured bond line thickness and failure loads for various specimens.

<b>Sample number</b>	<b>Minimum thickness (mm)</b>	<b>Maximum thickness (mm)</b>	<b>Difference in thickness (mm)</b>	<b>Mean thickness (mm)</b>	<b>Failure load (KN)</b>
1	0.35	0.8	0.45	0.58	7.91
2	0.31	0.94	0.64	0.63	6.45
3	0.42	0.56	0.14	0.49	7.46
4	0.37	0.65	0.28	0.51	6.83
5	0.38	0.54	0.16	0.46	7.21
6	0.34	0.59	0.24	0.47	7.3
7	0.33	0.55	0.22	0.44	7.61

All specimens exhibited light fiber tear failure in the first ply of the strap adjacent to the bond line, similar to the broken surface shown in Figure 7.5 of Section 7.1.1. The data presented in Table 7.4 does not give a conclusive trend of bond joint failure strength as a function of bond line thickness, since only 7 specimens were tested. The specimens could not be grouped into classes based on minimum thickness, using the method that was described above for linearly varying bond line thickness of single lap joints as described in Section 4.2.1. Future work should include better quality specimens that can be fabricated by using a fixture specifically designed for single strap joints.

### 7.2.2 Numerical Analysis

Due to the lack of sufficient number of samples in the experimental study as discussed in Section 7.2.1, a finite element study on predicting the strength of single strap bonded joints with varying bond line thickness could not be performed. Instead, a parametric strength and stress analysis was performed on a single strap bonded joint with a bond thickness of 0.6 mm at the center of the bond with various minimum and maximum thicknesses at the ends of the strap. The finite element model was meshed with

a finer mesh having element with a size of 0.02 mm in the overlap region, which was graded to a coarse mesh of element size of 2 mm towards the ends of the joint as shown in Figure 7.14. The boundary conditions as shown in Figure 7.12 were applied on the FE model.

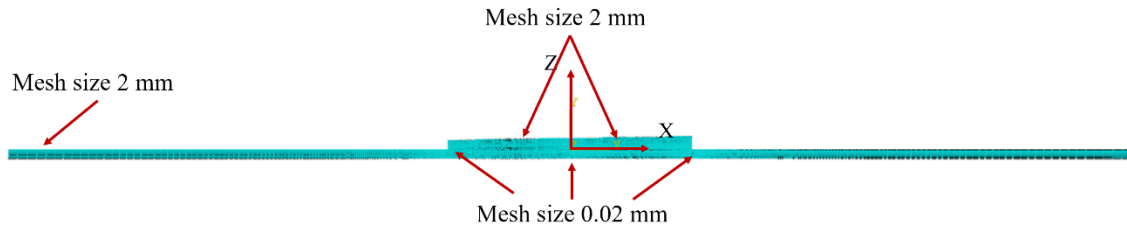


Figure 7.14. Mesh details for the study of varying bond line thickness in strap joints

The Critical zone method was used with the Azzi-Tsai criterion to predict the failure strength. The Azzi-Tsai criteria was employed here since it yielded the least average absolute percentage error in predicting the strength of single strap joints, as presented in Section 7.1.2. The results of the varying bond line thickness strap joint finite element study appear in Table 7.5. The FE predictions indicate no significant change in failure loads with an increase in the bond line thickness variation.

Table 7.5. FE predicted values for failure load for bond line thickness variations.

<b>Thickness variation (mm)</b>	<b>FE Failure load (KN)</b>
0.6 const	6.98
0.5 to 0.7	6.98
0.4 to 0.8	6.96
0.3 to 0.9	6.95
0.2 to 1	6.91

To investigate the effect of variation in thickness for single strap joints on the stress states in the adherend, a stress analysis was performed along a path through the mid plane of the first ply of the strap adherend as shown in Figure 7.15, since failure in all test specimens was observed at this location.

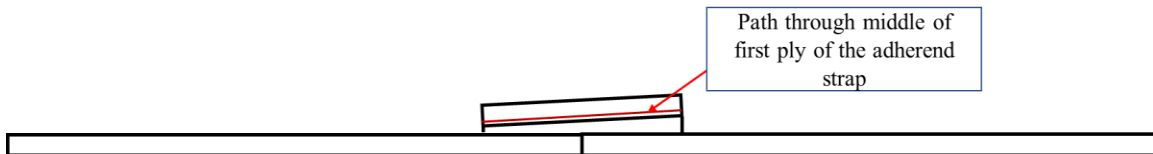


Figure 7.15. Path defined in the model for plotting of shear and peel stress.

The shear and the peel stresses are plotted at the center of the overlap, keeping the thickness at the center constant at 0.6 mm while changing the difference between the minimum and maximum bond thickness at each end of the strap, as shown in Figure 7.16 and Figure 7.17.

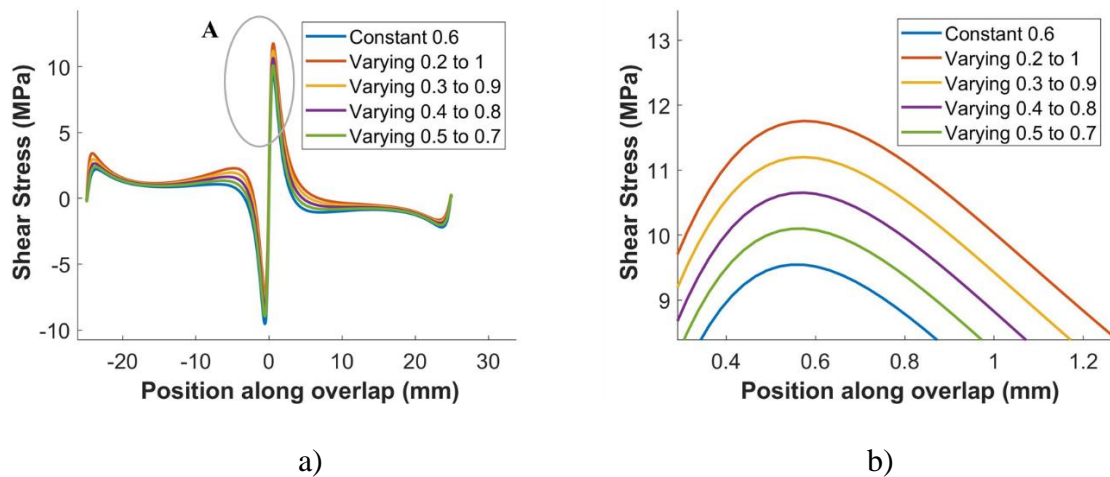


Figure 7.16. a) Shear stress distribution along middle of first ply closest to the bond line  
b) Magnified view of detail 'A'

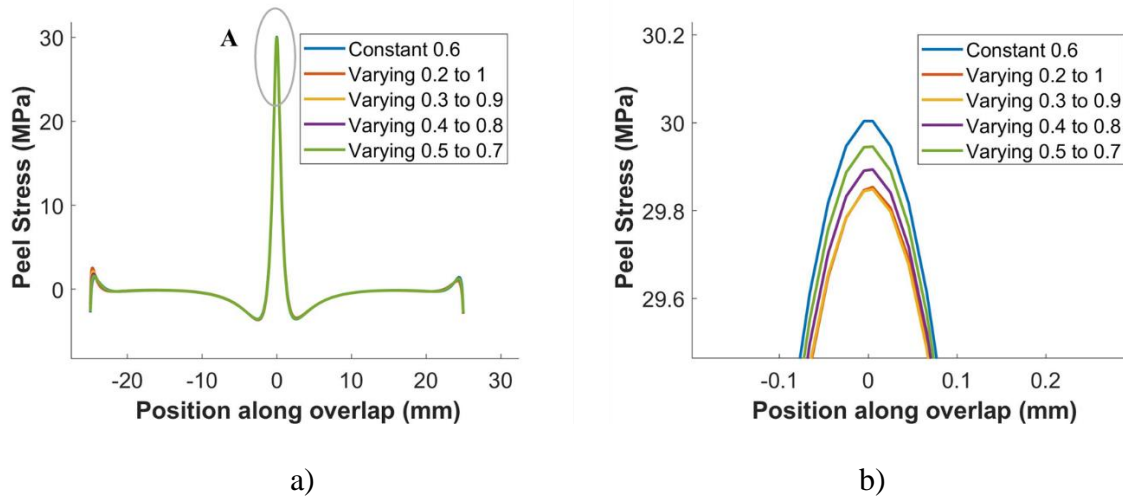


Figure 7.17. a) Peel stress distribution along middle of first ply closest to the bond line  
 b) Magnified view of detail 'A'

The peel stresses increase from 29.85 MPa to 30 MPa by 0.05% while shear stress increase from 7.25 MPa to 9.54 MPa by approximately 32% as the difference between the minimum and maximum bond line thickness increases.

Bond line thickness variations may occur in single strap joints due to improper fixturing. Experimental curve fits indicate that the failure strength decreases by approximately 32% when the thickness of a uniform bond line strap joint increases from 0.25 mm to 1.0 mm. Alternatively, the predicted shear stress increases by approximately 21% and the predicted peel stress increases by 15% as the bond line thickness increases from 0.25 to 1 mm. The Critical Zone method using Azzi-Tsai criterion is able to predict the failure loads of the uniform thickness strap joint within an average absolute percentage error of approximately 2.7% as compared to the experimental fit values. The study on linear variation of bond line thickness of single strap joints does not yield a conclusive experimental trend with regard to the variation in failure strength due to the lack of significant number of specimens. The Critical Zone method using Azzi-Tsai

criterion predicts no significant variation in failure strength in the models when the linear thickness variation increases, provided the thickness at the middle of the bond line remains constant. A stress analysis in the adherend's first layer shows that the shear stress at its mid plane increases by approximately 32% while the peel stress increases by only 0.05% with an increase in the difference between the minimum and the maximum bond line thickness. Further investigations using an improved fixture for fabricating single strap joint specimens of consistent quality has to be performed for quantifying the effects of linear bond line thickness variations.

## CHAPTER EIGHT

### Conclusions and Future Work

Adhesive bonding offers advantages such as light weight construction and corrosion resistance over other forms of joining such as riveting and bolting [4]. The presence of defects and imperfections deteriorate the load carrying capacity of bonded joints. Defects such as voids and inclusions have been widely studied in literature and have been found to decrease the strength of bonded joints. Unfortunately, there remains a lack of understanding of the effects of imperfections such as bond line thickness variations and adhesive distribution, and defects such as inclusions in the bonding adherend, on the strength of bonded joints.

The aim of the current study was to investigate the effects of bond line thickness variations, inclusion defects in the adherends and incomplete adhesive distribution on the strength of bonded laminated polymer composites and to understand the underlying stress states that occur in the presence of such defects and imperfections.

#### *8.1 Conclusions*

In Chapter Four, the effect of variation in the bond line thickness was investigated. The effects of changes in constant bond line thickness have been widely studied in literature but the effect of linear variations in bond line thickness on the strength of bonded joints, have not been addressed. Linear bond line thickness variations may occur due to improper fabrication techniques employed while bonding.

The initial part of the study investigated the effect of increasing the bond line thickness in the composite bonded single lap joints with a uniform bond line thickness. Four sets of experiments were planned with bond line thickness increasing from 0.25 mm to 1.00 mm in steps of 0.25 mm. An increase in the bond line thickness in the uniform bond line thickness joints caused a reduction in failure load by almost 46% when the bond line thickness increased from 0.25 mm to 1.2 mm. A similar trend of decrease in failure strengths was observed by previous researchers [21,31,37–39,110]. The Critical Zone method using the Hoffman's failure criterion was found to be the most effective in predicting the failure loads for bonded joints with a uniform bond line thickness, showing an average absolute error in strength predictions of approximately 7.74% . The stress analysis revealed an increase in peel and shear stresses respectively, when the bond line thickness increased from 0.25 to 1.2 mm.

The linear variations in bond line thickness, due to misalignment of the adherends in a single lap joint configuration, was investigated in the second part of Chapter Four. Three sets of experiments were planned with a minimum bond line thickness of 0.25 mm and a maximum bond thickness at the other end of the overlap of 0.5, 0.75 and 1.0 mm. Due to difficulties in maintaining the bond line thickness at its intended values, the tested specimens were divided into four classes based on their minimum bond line thickness. The average of the minimum thickness measured was used to represent each class. Test results showed that the failure strength decreased with an increase in the difference between the minimum and maximum bond thickness, provided the minimum bond line thickness remained constant. The strength of joint configurations with a linearly varying bond line thickness was predicted using the Critical Zone method applying the Hoffman's

criterion, with an accuracy ranging from 0.62% to 22% with respect to the experimental fit values. The large variation in accuracy may be due to the assumptions made in the analysis of grouping the specimens based on their minimum thickness. The stress analysis revealed an increase of in the peel and the shear stresses when the bond line thickness variation of 0.33 mm to 1.33 mm is compared with a uniform bond line joint of 0.33 mm thickness.

In Chapter Five, the effect of adhesive distribution across the overlap area of a single lap bonded joint, on their failure strength was investigated. The effect of an incomplete distribution of the adhesive has not been addressed in the prior literature. Incomplete distribution of the adhesive may occur due to carelessness from the part of the operator or due to improper fabrication techniques. Such scenarios were practically demonstrated by applying the adhesive as a straight line and as a circular mound in the overlap region. The adhesive spread out into an elliptical and circular shape respectively not filling the complete bond overlap area.

The first part of Chapter Five studied the effect of using woven carbon fiber composite adherends on the strength of the bonded joints. The effect of adhesive distribution was studied by creating circular and elliptical shaped adhesive in the bond overlap region using PTFE templates. The shapes were selected on the basis of initial trials which investigated the shape of spread of the adhesive when applied as a straight line or as a spherical mound. Two orientations of the elliptical shaped adhesive were studied with the major axis either parallel (Orientation 1) or perpendicular (Orientation 2) to the loading direction. Three size levels for each configuration were studied. The failure loads decreased with a decrease in the coverage area of the adhesive for each shape

configuration studied. The orientation of the adhesive in the case of elliptical shaped adhesive was found to affect the failure load. For the adhesives having an elliptical shape and same bonded area, the configuration having its major axis perpendicular to the loading direction was found to show a higher failure strength than that with the major axis parallel to the load direction. Ultrasonic scans were performed on the joints, which were able to detect the size and shape of the bonded area of the adhesive.

The effect of incomplete adhesive distribution while bonding unidirectional composites was addressed in the second section of Chapter Five. The orientation of the adhesive had the same effect on the strength of bonded joints with incomplete coverage, with the elliptical shaped adhesive having the major axis transverse to the loading direction exhibiting higher failure strength than that aligned along the loading axis. FE simulations were performed on the joints to assess the stress states in the adherend and the adhesive with an incomplete adhesive distribution. The shear and the peel stresses in the first ply adjacent to the bond line were studied since a light fiber tear failure at this location was observed in all the joints. The shear and the peel stresses increased with decrease in the bond area for each shape configuration. The comparison of shear and peel stresses between the different orientations of the adhesive revealed that the maximum peel and shear decreased when the adhesive configuration changed from orientation 1 to orientation 2 which correlated with a higher failure strength of orientation 1. The failure in the bonded joints with incomplete adhesive coverage could not be predicted by the Critical Zone method which may be because of the redistribution of stresses due to the reduction in the bonded area when compared to a joint with complete coverage of the adhesive.

In Chapter Six, the effect of inter-layer inclusions in the adherends, between the first and the second ply adjacent to the bond line was studied. The effect of inclusions embedded in the adhesive have been widely studied in the literature. Inclusion defects in the adherend especially in the region near the ends of the bonded overlap could significantly affect the failure strength of composite bonded joints.

The inclusion defect was introduced in form of a PTFE strip inserted along the entire width of the bond area, in one of the adherends bonded in a single lap joint configuration. In the first part of Chapter Six, the effect of the position of the inclusion defect along the loading axis, on the bond joint strength was investigated. A preliminary finite element analysis revealed no significant change in the stresses with the length of the inclusion along the overlap length of the bonded joints. Hence a length of 12.7 mm for the inclusion was selected. Three different positions of the inclusion were chosen with the inclusion located completely inside with one end above the end of the overlap, half inside the overlap and completely outside of the bonded overlap region with one end above the end of the overlap. Experimental results showed that the joint specimens with the inclusion completely inside of the bonded region yielded the least bond failure strength, approximately 42% lower than a non-defective configuration. The specimens with the inclusion completely outside had failure strength comparable with the non-defective configuration. A stress analysis on the adherends showed an increase in the shear and peel stresses in the first ply adjacent to the bond line when the inclusion defects were located inside of the overlap. Failure prediction using Critical Zone method was able to predict the failure load for the first two configurations but not for the case where the inclusion was located completely outside of the overlap. The over-estimation of the

critical volume due to the presence of singularities induced in the model because of the introduction of a discontinuity to simulate the inclusion defect may be the cause of this under-prediction of failure load.

In the second part of the study, the effect of varying the ply orientations and inclusion defect between the first and second ply of the adherend was investigated. Four different adherend stacking configurations were investigated namely  $[90/0]_3$ ,  $[90/45/0]_S$ ,  $[45/90/0]_S$  and  $[45/0/90]_S$ . All the configurations were compared with the bonded joints having  $[0]_6$  unidirectional layup of adherends. The orientation of the ply adjacent to the bond line influenced the failure strength of the bonded joint. The adherend layup with the  $0^\circ$  ply adjacent to the bond line yielded higher strengths while the ones with a higher angle of  $90^\circ$  yielded the least strength. The longitudinal bending stiffness of the adherends also affected the failure strength of the bonded joints. The same trend was observed for joints having inclusion defects. A reduction in failure strength was observed across all the joint configurations, with the  $[45/0/-45]_S$  configuration exhibiting almost 46% decrease while the  $[90/0]_3$  exhibiting almost 35% decrease in failure strength in the presence of inclusion defects. Inter-ply failure was observed in all the joint specimens with varying ply orientations. The  $0^\circ$  ply stopped the progression of failure through it and relegated it along a tangential path between the ply adjacent to it. Failure predictions using critical zone method could not be performed because of the inter-laminar failure observed in the bonded joint specimens. Alternatively, approaches like the Cohesive Zone modeling coupled with a progressive damage simulation approaches such as XFEMs could be used to predict the failure in the bonded joints with different ply layups.

In Chapter Seven, the effect of bond line thickness variations in Single strap joints was investigated. Strap joints are used for patch repairs of composite and metal structures. Bond line thickness variations may occur due to improper fabrication techniques employed while bonding the adherends. The effect of bond line thickness variations in single strap joints have not been addressed in literature.

The first part of the chapter investigated the effects of varying the bond line thickness in uniform bond line thickness joints. Four different bond line thicknesses 0.25, 0.5, 0.75 and 1.00 mm were chosen for the study. A reduction in failure strength was observed when the bond line thickness increased. The shear and the peel stresses also increased when the bond line thickness increased. The increase in bond line thickness was also associated with approximately 32% decrease in the failure loads. The Critical Zone method was used to predict the failure loads of the single strap joint. The Azzi-Tsai and Hoffman`s criteria yielded better failure strength predictions with an average absolute percentage error of 2.87% and 3.7% respectively, when compared with the experimental trend. The study on linear bond line thickness variations did not yield significant results due to imperfections in the prepared specimens. The strength predictions performed using the Critical Zone method suggested no significant variation in failure strength when the thickness at the middle of the strap overlap length remained constant, while the bond thickness at each end varied. A stress analysis revealed no significant change in the peel stress but a significant increase in the shear stress, with an increase in the difference between the minimum and the maximum bond line thickness. Further investigations using better quality specimens would be required to ascertain the effect of linear variation of bond line thickness on bonded single strap joint strength.

## 8.2 Future Scope

The investigations into the variations in bond line thickness can be extended by incorporating the bond thickness data across the whole bonded area into the FE model. This can be achieved by using a non-destructive test such as ultrasonic scanning. A detailed 3D model can be modelled on the basis of the bond line thickness measured using ultrasonic scanning. The analysis of failure can be performed using the Critical Zone methods which should yield better predictions of failure strength.

The Critical Zone method was not found to be applicable in the case of bonded joints with incomplete adhesive distribution. A combination of Cohesive zone modeling and damage zone approach can be used to predict the failure load of bonded joints with incomplete adhesive distribution.

In the study of inclusions in the composite adherends, a damage-mechanics based approach like XFEM may be used to better predict the failure strength. For the composites with varying ply orientations, interlaminar failure was observed in the current study. Interlaminar failure cannot be predicted using the Critical Zone methods and would require the use of a Cohesive zone modeling approach to predict the location of failure.

Better fabrication fixtures can be designed for fabrication of single strap joints. Improvised fixtures would help in fabrication of better-quality test specimens using which the effect of linear variation in bond line thickness on strength of single strap joints can be better understood.

The applicability of the Critical Zone method can be extended for other type of joint configurations such as a Double lap joint or a Double strap joint. The effect of imperfections or defects can also be studied.

## APPENDICES

## APPENDIX A

### Characterization of Carbon Fiber Adherends and Adhesive

Carbon fiber reinforced polymer adherends were tested for their tensile, compressive, and transverse shear strengths and the elastic moduli using the procedures described in Section 3.1.3.1. The experimental data of the tests performed have been summarized in this section.

Tensile tests were performed based on the ASTM D3039 standard. The results of the tensile test for the unidirectional carbon fiber adherends of  $0^\circ$  orientation have been tabulated in Table A.1. Five samples of unidirectional carbon fiber adherends were tested. Sample D was discarded because it failed prematurely due to it being a defective sample. The elastic modulus  $E_x$ , in-plane shear modulus ( $G_{XY}$ ) and the in-plane Poisson's ratio ( $\nu_{XY}$ ) calculated for each sample have been tabulated in Table A.1.

Similarly, results of the tensile tests for the unidirectional carbon fiber adherends of  $90^\circ$  orientation have been tabulated in Table A.2.

Table A.1. Tensile test results of unidirectional carbon fiber adherends of 0° orientation

	<b>Samples</b>				
	<b>A</b>	<b>B</b>	<b>C</b>	<b>D</b>	<b>E</b>
<b>Force (KN)</b>	31148	37058.9	43360.2	--	38748
<b>Width (mm)</b>	15.2	16.7	15.6	--	15.15
<b>Thickness (mm)</b>	1.86	1.73	1.78	--	1.72
<b>Area (mm<sup>2</sup>)</b>	28.27	27.98	27.76	--	26.05
<b>Maximum stress (MPa)</b>	1101.73	1324.76	1561.52	--	1486.1
<b>Modulus of Elasticity-E<sub>x</sub> (MPa)</b>	117670	141833.4	123543.15	--	124367.97
<b>Shear Modulus-G<sub>XY</sub> (MPa)</b>	3500	4369	2269.67	--	2369.64
<b>Poisson's ratio-ν<sub>xy</sub></b>	0.33	0.26	0.25	--	0.25

Table A.2 Tensile test results of unidirectional carbon fiber adherends of 90° orientation

	<b>Samples</b>				
	<b>A</b>	<b>B</b>	<b>C</b>	<b>D</b>	<b>E</b>
<b>Force (N)</b>	742.8	810.5	836	769.5	908.5
<b>Width (mm)</b>	24.76	26.03	23.9	25.9	27.12
<b>Thickness (mm)</b>	1.78	1.73	1.72	1.8	1.85
<b>Area (mm<sup>2</sup>)</b>	44.08	45.04	41.11	46.62	50.18
<b>Maximum stress (MPa)</b>	16.85	17.98	20.34	16.51	18.11
<b>Modulus of Elasticity-E<sub>y</sub> (MPa)</b>	9330.72	8555.84	8793.36	7157.7	8449.2

The stress-strain curves for the unidirectional carbon fiber adherends in the 0° orientation are as shown in Figure A.1. The strains appearing in the figure were as measured from the strain gauges.

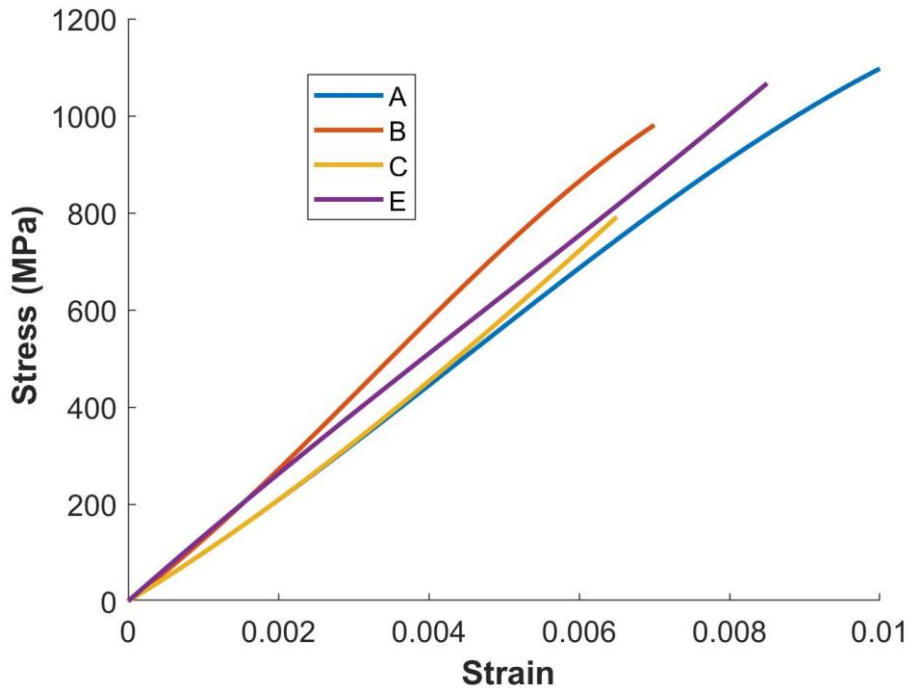


Figure A.1. Stress-strain curves of unidirectional carbon fiber adherends of 0° orientation

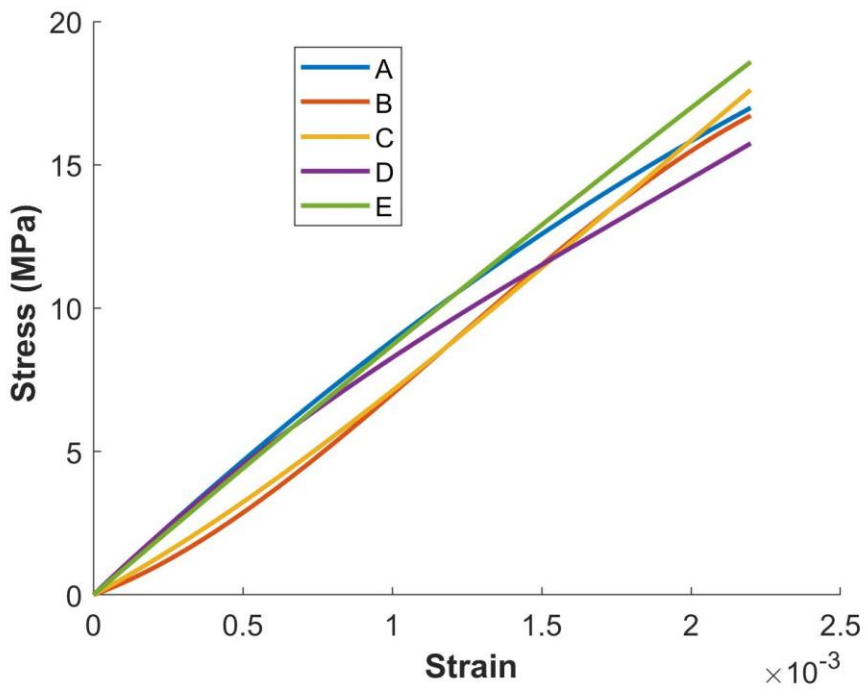


Figure A.2. Stress-strain curves of unidirectional carbon fiber adherends of 90° orientation

The compression tests were performed as per the SRM IR-94 standard. The results for the five samples of unidirectional carbon fiber adherends of 0° orientation have been tabulated in Table A.3.

Table A.3. Compression test results of unidirectional carbon fiber adherends of 0° orientation

	<b>Samples</b>				
	<b>A</b>	<b>B</b>	<b>C</b>	<b>D</b>	<b>E</b>
<b>Force (N)</b>	8621.47	9786.8	9624.8	6131.88	11403.6
<b>Width (mm)</b>	15.97	15.8	16.2	16.1	16.01
<b>Thickness (mm)</b>	1.83	1.85	1.83	1.84	1.79
<b>Area (mm<sup>2</sup>)</b>	29.23	29.23	29.65	29.63	28.65
<b>Maximum stress (MPa)</b>	295.01	334.83	324.65	206	397.93

Similarly, the results for the carbon fiber adherends of 90° orientation are as shown in Table A.4. The results of sample E were discarded because sample was found defective.

Table A.4. Compression test results of unidirectional carbon fiber adherends of 90° orientation

	<b>Samples</b>				
	<b>A</b>	<b>B</b>	<b>C</b>	<b>D</b>	<b>E</b>
<b>Force (N)</b>	2125.06	2165.73	1589.13	2349.98	--
<b>Width (mm)</b>	15.9	15.8	16.2	16.1	--
<b>Thickness (mm)</b>	1.83	1.82	1.85	1.8	--
<b>Area (mm<sup>2</sup>)</b>	29.09	28.76	29.97	29.98	--
<b>Maximum stress (MPa)</b>	73.04	75.31	53.03	81.09	--

The short beam test was performed as per ASTM D2344. The results of the test have been summarized in Table A.5.

Table A.5. Short beam test results

	<b>Samples</b>				
	<b>A</b>	<b>B</b>	<b>C</b>	<b>D</b>	<b>E</b>
<b>Force (N)</b>	732.58	818.06	833.44	714.21	860.49
<b>Area (mm<sup>2</sup>)</b>	10.54	10.69	10.08	9.85	10.23
<b>Maximum stress (MPa)</b>	52.14	57.37	62.01	54.41	63.15

The tensile properties of the Hysol 9309 NA adhesive were estimated using ASTM D638. The experimental data has been summarized in Table A.6

Table A.6. Tensile test results of Hysol 9309 NA adhesive

	<b>Samples</b>				
	<b>A</b>	<b>B</b>	<b>C</b>	<b>D</b>	<b>E</b>
<b>Force (N)</b>	3066.2	2899.6	2903	2840.4	2827.2
<b>Width (mm)</b>	12.96	13.11	12.87	13.02	12.82
<b>Thickness (mm)</b>	5.92	5.73	5.74	5.7	5.65
<b>Area (mm<sup>2</sup>)</b>	76.73	75.12	73.88	74.22	72.44
<b>Maximum stress (MPa)</b>	39.97	38.6	39.3	38.28	39.04
<b>Modulus of Elasticity-E (MPa)</b>	2163	1937	1935	2404	2144

The stress-strain curves of the adhesive tensile test samples tested are as shown in Figure A.3. The strains appearing in the figure were as measured from the strain gauges.

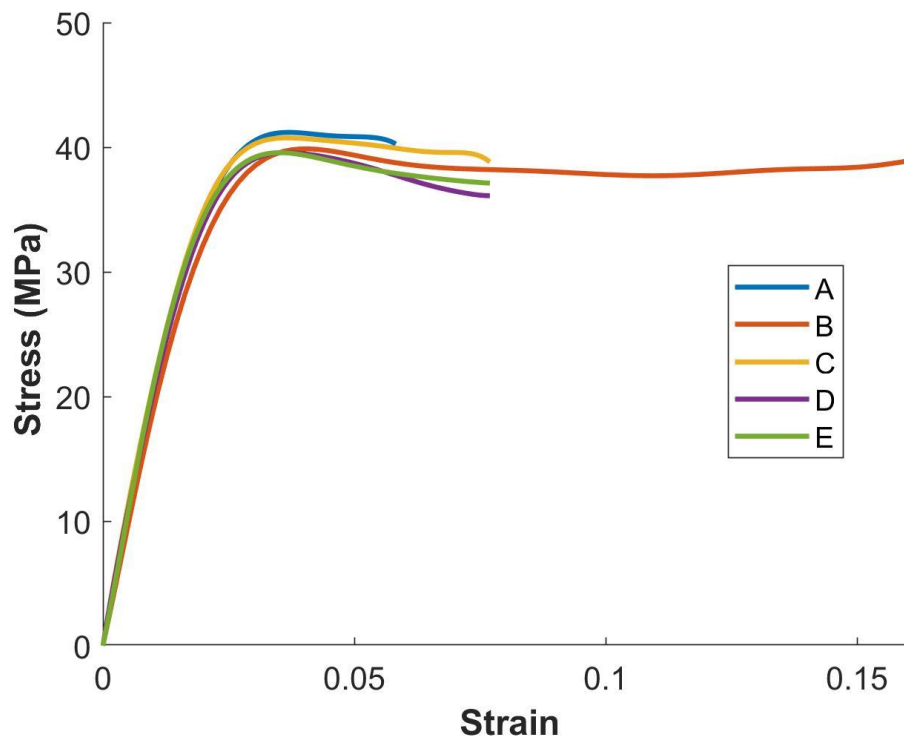


Figure A.3. Stress-strain curves of Hysol 9309 NA adhesive

## APPENDIX B

### ABAQUS UMAT FORTRAN Code for Strength Prediction Using Critical Zone Method

A user subroutine (UMAT) was developed for calculating the failure criteria coefficients required for predicting the failure loads using the Critical Zone method. The damage variables *DAM 1 to DAM7* evaluates the various criterion namely the maximum longitudinal stress, maximum normal stress, maximum shear stress, Yamada-Sun, Azzi-Tsai Norris, Hoffman`s and Tsai-Wu criteria listed as Equation 2.3 to 2.7 in Section 2.3.2.

The FORTRAN code for the UMAT subroutine is:

```
SUBROUTINE UMAT(STRESS,STATEV,DDSDDE,SSE,SPD,SCD,  
1 RPL,DDSDDT,DRPLDE,DRPLDT,  
2 STRAN,DSTRAN,TIME,DTIME,TEMP,DTEMP,PREDEF,DPRED,CMNAME,  
3 NDI,NSHR,NTENS,NSTATV,PROPS,NPROPS,COORDS,DROT,PNEWDT,  
4 CELENT,DFGRD0,DFGRD1,NOEL,NPT,LAYER,KSPT,JSTEP,KINC)  
  
C  
    INCLUDE 'ABA_PARAM.INC'  
  
C  
    CHARACTER*80 CMNAME  
  
    DIMENSION STRESS(NTENS),STATEV(NSTATV),  
1 DDSDDE(NTENS,NTENS),DDSDDT(NTENS),DRPLDE(NTENS),
```

```
2 STRAN(NTENS),DSTRAN(NTENS),TIME(2),PREDEF(1),DPRED(1),
3 PROPS(NPROPS),COORDS(3),DROT(3,3),DFGRD0(3,3),DFGRD1(3,3),
4 JSTEP(4),EMAT(NTENS,NTENS),IMAT(NTENS,NTENS)
```

```
C ELASTIC USER SUBROUTINE
```

```
C CALCULATING STIFFNESS TERMS
```

```
DO I=1,NTENS
```

```
DO J=1,NTENS
```

```
DDSDDE(I,J)=0.0D0
```

```
ENDDO
```

```
ENDDO
```

```
C
```

```
C COMPLIANCE MATRIX ENTRIES
```

```
DDSDDE(1,1) = PROPS(1)
```

```
DDSDDE(1,2) = PROPS(2)
```

```
DDSDDE(2,2) = PROPS(3)
```

```
DDSDDE(1,3) = PROPS(4)
```

```
DDSDDE(2,3) = PROPS(5)
```

```
DDSDDE(3,3) = PROPS(6)
```

```
DDSDDE(4,4) = PROPS(7)
```

```
DDSDDE(5,5) = PROPS(8)
```

```
DDSDDE(6,6) = PROPS(9)
```

```
C CALCULATING STRESS VALUES
```

```
DO I=1,NTENS
```

```

DO J=1,NTENS
  STRESS(I)=STRESS(I)+DDSDDE(I,J)*DSTRAN(J)
ENDDO
ENDDO
S1 = STRESS(1)
S2 = STRESS(2)
S3 = STRESS(3)
Ss = STRESS(4)
Xt = PROPS(10)
Xc = PROPS(11)
Yt = PROPS(12)
Yc = PROPS(13)
tau12 = PROPS(14)
! Max S11 stress
IF (S1 >= 0) THEN
  DAM1 = (S1/Xt)
ELSE
  DAM1 = ABS((S1/Xc))
ENDIF
! Max S22 stress
IF (S2 >= 0) THEN
  DAM2 = (S2/Yt)
ELSE

```

```

        DAM2 = ABS((S2/Yc))
    ENDIF

! Max S12 stress

        DAM3 = ABS((Ss/tau12))

! Yamada-Sun criteria

        DAM4 = (S2/Yt)**2 + (Ss/tau12)**2

! Azzi-Tsai criteria

        DAM5 = ((S1**2-(S1*S2))/(Xc*Xt)+(S2**2/Yt**2)+(Ss/tau12)**2

! Hoffman`s criteria

        DAM6 = (S1**2-(S1*S2))/(Xc*Xt)+(S2**2)/(Yc*Yt)+(Xc-Xt)/(Xc*Xt)
&          *S1 + (Yc-Yt)/(Yc*Yt)*S2 + (Ss/tau12)**2

! Tsai Hill criteria

        DAM7 = (S1/Xt)**2 + (S2/Yt)**2 - (S1*S2/Xt**2) + (Ss/tau12)**2

! Damage Variables

        STATEV(1) = DAM1

        STATEV(2) = DAM2

        STATEV(3) = DAM3

        STATEV(4) = DAM4

        STATEV(5) = DAM5

        STATEV(6) = DAM6

        STATEV(7) = DAM7

RETURN

END

```

## APPENDIX C

### Three-Dimensional Adaptation of the Generalized Form of Hoffman`s Criteria for Strength Prediction

The failure criterion for orthotropic brittle materials was presented by Hoffman [90] as an equation in its the general form as Equation C.1. The coordinate axes are as defined as per Figure C.1. The general form of the Hoffman`s equations were expanded to implement the user subroutine UMAT in a 3D model as described in Section 5.2.2.

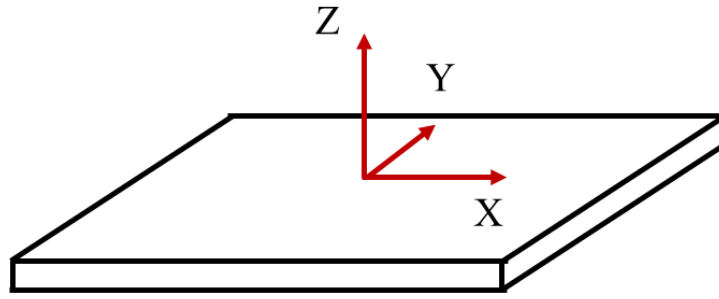


Figure C.1. Coordinate system on a 3D plate.

$$C_1(\sigma_y - \sigma_z)^2 + C_2(\sigma_z - \sigma_x)^2 + C_3(\sigma_x - \sigma_y)^2 + C_4(\sigma_x) + C_5(\sigma_y) + C_6(\sigma_z) + C_7(\tau_{yz})^2 + C_8(\tau_{zx})^2 + C_9(\tau_{xy})^2 = 1 \quad (C.1)$$

$C1$  to  $C9$  are material parameters given by

$$C_1 = \frac{1}{2}[(Y_t Y_c)^{-1} + (Z_t Z_c)^{-1} - (X_t X_c)^{-1}] \quad (C.2)$$

$$C_2 = \frac{1}{2}[(Z_t Z_c)^{-1} + (X_t X_c)^{-1} - (Y_t Y_c)^{-1}] \quad (C.3)$$

$$C_3 = \frac{1}{2}[(X_t X_c)^{-1} + (Y_t Y_c)^{-1} - (Z_t Z_c)^{-1}] \quad (C.4)$$

$$C_4 = (X_t)^{-1} - (X_c)^{-1} \quad (C.5)$$

$$C_5 = (Y_t)^{-1} - (Y_c)^{-1} \quad (C.6)$$

$$C_6 = (Z_t)^{-1} - (Z_c)^{-1} \quad (C.7)$$

$$C_7 = (S_{yz})^{-2} \quad (C.8)$$

$$C_8 = (S_{zx})^{-2} \quad (C.9)$$

$$C_9 = (S_{xy})^{-2} \quad (C.10)$$

where:  $X_t$ ,  $Y_t$  and  $Z_t$  are the three axial tensile strengths,  $X_c$ ,  $Y_c$  and  $Z_c$  are the three axial compressive strengths,  $S_{xy}$ ,  $S_{yz}$  and  $S_{zx}$  are the three shearing strengths.

Since the carbon fiber reinforced polymer materials, used in this study as adherends, are orthotropic in nature,  $Y_t = Z_t$ ,  $Y_c = Z_c$  and  $S_{yz} = S_{zx}$ . Substituting these in Equation C.2 to C.10.

$$C_1 = \frac{1}{2}[2 (Z_t Z_c)^{-1} - (X_t X_c)^{-1}] \quad (C.11)$$

$$C_2 = \frac{1}{2}[(X_t X_c)^{-1}] \quad (C.12)$$

$$C_3 = \frac{1}{2}[(X_t X_c)^{-1}] \quad (C.13)$$

$$C_4 = (X_t)^{-1} - (X_c)^{-1} \quad (C.14)$$

$$C_5 = (Z_t)^{-1} - (Z_c)^{-1} \quad (C.15)$$

$$C_6 = (Z_t)^{-1} - (Z_c)^{-1} \quad (C.16)$$

$$C_7 = (S_{zx})^{-2} \quad (C.17)$$

$$C_8 = (S_{zx})^{-2} \quad (C.18)$$

$$C_9 = (S_{xy})^{-2} \quad (C.19)$$

The equations C.11 through C.19 along with Equation C.1 was used in the FORTRAN code for implementing the user subroutine UMAT, as described in Appendix B.

## BIBLIOGRAPHY

- [1] Barbero, E. J., 2017, "Introduction to Composite Materials Design", CRC Press.
- [2] Carson E G, 2012, "The Future of Carbon Fiber to 2017," London.
- [3] Das, S., Warren, J., West, D., and Laboratory, O. R. N., 2016, "Global Carbon Fiber Composites Supply Chain Competitiveness Analysis," Technical Report, p. 116.
- [4] Ebnesajjad, Sina, 2010 "Handbook of Adhesives and Surface Preparation - Technology, Applications and Manufacturing."
- [5] Banea, M. D., and da Silva, L. F. M., 2009, "Adhesively Bonded Joints in Composite Materials: An Overview," Proceedings of the Institution of Mechanical Engineers, Part L: Journal of Materials: Design and Applications, **223**(1), pp. 1–18.
- [6] Goland, M., 1944, "The Stresses in Cemented Joints," J. Appl. Mech., **17**, p. 66.
- [7] Tong, L., 2016, "An Assessment of Failure Criteria to Predict the Strength of Adhesively Bonded Composite Double Lap Joints:," Journal of Reinforced Plastics and Composites.
- [8] He, X., 2011, "A Review of Finite Element Analysis of Adhesively Bonded Joints," International Journal of Adhesion and Adhesives, **31**(4), pp. 248–264.
- [9] Miki, C., 1993, "Discontinuities, Imperfections and Defects in Welded Joints and Their Effects on Joint Performance," Welding International, **7**(1), pp. 5–8.
- [10] Karachalios, E. F., Adams, R. D., and da Silva, L. F. M., 2013, "Strength of Single Lap Joints with Artificial Defects," International Journal of Adhesion and Adhesives, **45**, pp. 69–76.
- [11] Allin, J. M., "Disbond detection in adhesive joints using low-frequency ultrasound," p. 147.
- [12] Adams, R. D., and Cawley, P., 1988, "A Review of Defect Types and Nondestructive Testing Techniques for Composites and Bonded Joints," NDT International, **21**(4), pp. 208–222.

- [13] Brotherhood, C. J., Drinkwater, B. W., and Dixon, S., 2003, "The Detectability of Kissing Bonds in Adhesive Joints Using Ultrasonic Techniques," *Ultrasonics*, **41**(7), pp. 521–529.
- [14] D. Stratakis, 2017, "Performance of Aerospace Composites in the Presence of Process-Induced Defects," Cranfield University.
- [15] Jiao, D., and Rose, J. L., 1991, "An Ultrasonic Interface Layer Model for Bond Evaluation," *Journal of Adhesion Science and Technology*, **5**(8), pp. 631–646.
- [16] Heslehurst, R. B., 1999, "Observations in the Structural Response of Adhesive Bondline Defects," *International journal of adhesion and adhesives*, **19**(2–3), pp. 133–154.
- [17] Ramalho, L. D. C., Campilho, R. D. S. G., Belinha, J., and da Silva, L. F. M., 2020, "Static Strength Prediction of Adhesive Joints: A Review," *International Journal of Adhesion and Adhesives*, **96**, p. 102451.
- [18] Korzeniowski, M., Piwowarczyk, T., and Maev, R. G., 2014, "Application of Ultrasonic Method for Quality Evaluation of Adhesive Layers," *Archives of Civil and Mechanical Engineering*, **14**(4), pp. 661–670.
- [19] N.Blackman and D.A.Jack, 2019, "Foreign Object Identification within a Laminated Carbon Fiber Composite Using Pulse-Echo Ultrasonics," Conference proceedings ASNT 2019.
- [20] Lee, D.-B., Ikeda, T., Miyazaki, N., and Choi, N.-S., 2004, "Effect of Bond Thickness on the Fracture Toughness of Adhesive Joints," *J. Eng. Mater. Technol*, **126**(1), pp. 14–18.
- [21] Silva, L. F. M. da, Rodrigues, T. N. S. S., Figueiredo, M. A. V., Moura, M. F. S. F. de, and Chousal, J. A. G., 2006, "Effect of Adhesive Type and Thickness on the Lap Shear Strength," *The Journal of Adhesion*, **82**(11), pp. 1091–1115.
- [22] Kim, H., 2003, "The Influence of Adhesive Bondline Thickness Imperfections on Stresses in Composite Joints," *The Journal of Adhesion*, **79**(7), pp. 621–642.
- [23] Ghrib, M., Berthe, L., Mechbal, N., Rébillat, M., Guskov, M., Ecault, R., and Bedreddine, N., 2017, "Generation of Controlled Delaminations in Composites Using Symmetrical Laser Shock Configuration," *Composite Structures*, **171**, pp. 286–297.
- [24] Campilho, R. D. S. G., 2017, "Strength Prediction of Adhesively-Bonded Joints", Chapman and Hall/CRC, Portland, United States.

- [25] D14 Committee, "Test Method for Apparent Shear Strength of Single-Lap-Joint Adhesively Bonded Metal Specimens by Tension Loading (Metal-to-Metal)", ASTM International.
- [26] E28 Committee, "Test Methods for Tension Testing of Metallic Materials", ASTM International.
- [27] SACMA Recommended Methods, "Compressive Properties of Oriented Fiber-Resin Composites".
- [28] D30 Committee, "Test Method for Short-Beam Strength of Polymer Matrix Composite Materials and Their Laminates", ASTM International.
- [29] Hertzberg, R. W., 2012, "Deformation and Fracture Mechanics of Engineering Materials, 5th Edition,"
- [30] Budhe, S., Banea, M. D., de Barros, S., and da Silva, L. F. M., 2017, "An Updated Review of Adhesively Bonded Joints in Composite Materials," *International Journal of Adhesion and Adhesives*, **72**, pp. 30–42.
- [31] Gleich, D. M., Tooren, M. J. L. V., and Beukers, A., 2001, "Analysis and Evaluation of Bondline Thickness Effects on Failure Load in Adhesively Bonded Structures," *Journal of Adhesion Science and Technology*, **15**(9), pp. 1091–1101.
- [32] Gardon, J. L., 1963, "Peel Adhesion. I. Some Phenomenological Aspects of the Test," *Journal of Applied Polymer Science*, **7**(2), pp. 625–641.
- [33] Petrie, E. M., 2007, "Handbook of Adhesives and Sealants", McGraw Hill Professional.
- [34] Bascom, W. D., and Cottingham, R. L., 1976, "Effect of Temperature on the Adhesive Fracture Behavior of an Elastomer-Epoxy Resin," *The Journal of Adhesion*, **7**(4), pp. 333–346.
- [35] Loch, A. J. K., and Shaw, S. J., 1981, "The Fracture Resistance of a Toughened Epoxy Adhesive," *The Journal of Adhesion*, **12**(1), pp. 59–77.
- [36] Adams, R. D., and Peppiatt, N. A., 1974, "Stress Analysis of Adhesive-Bonded Lap Joints:," *Journal of Strain Analysis*.
- [37] Banea, M. D., da Silva, L. F. M., and Campilho, R. D. S. G., 2015, "The Effect of Adhesive Thickness on the Mechanical Behavior of a Structural Polyurethane Adhesive," *The Journal of Adhesion*, **91**(5), pp. 331–346.
- [38] Crocombe, A. D., 1989, "Global Yielding as a Failure Criterion for Bonded Joints," *International Journal of Adhesion and Adhesives*, **9**(3), pp. 145–153.

- [39] Rahman, N. M., and Sun, C. T., 2014, "Strength Calculation of Composite Single Lap Joints with Fiber-Tear-Failure," *Composites Part B: Engineering*, **62**, pp. 249–255.
- [40] Neto, J. A. B. P., Campilho, R. D. S. G., and da Silva, L. F. M., 2012, "Parametric Study of Adhesive Joints with Composites," *International Journal of Adhesion and Adhesives*, **37**, pp. 96–101.
- [41] Li, J., Yan, Y., Zhang, T., and Liang, Z., 2015, "Experimental Study of Adhesively Bonded CFRP Joints Subjected to Tensile Loads," *International Journal of Adhesion and Adhesives*, **57**, pp. 95–104.
- [42] Gültekin, K., Akpınar, S., and Özel, A., 2014, "The Effect of the Adherend Width on the Strength of Adhesively Bonded Single-Lap Joint: Experimental and Numerical Analysis," *Composites Part B: Engineering*, **60**, pp. 736–745.
- [43] Park, J.-H., Choi, J.-H., and Kweon, J.-H., 2010, "Evaluating the Strengths of Thick Aluminum-to-Aluminum Joints with Different Adhesive Lengths and Thicknesses," *Composite Structures*, **92**(9), pp. 2226–2235.
- [44] Kwakernaak, A., Hofstede, J., Poulis, J., and Benedictus, R., 2012, "8 - Improvements in Bonding Metals for Aerospace and Other Applications," *Welding and Joining of Aerospace Materials*, M.C. Chaturvedi, ed., Woodhead Publishing, pp. 235–287.
- [45] Aydin, M. D., Özel, A., and Temiz, Ş., 2005, "The Effect of Adherend Thickness on the Failure of Adhesively-Bonded Single-Lap Joints," *Journal of Adhesion Science and Technology*, **19**(8), pp. 705–718.
- [46] Kupsi, J., Teixeira de Freitas, S., Zarouchas, D., Camanho, P. P., and Benedictus, R., 2019, "Composite Layup Effect on the Failure Mechanism of Single Lap Bonded Joints," *Composite Structures*, **217**, pp. 14–26.
- [47] Hart-Smith, L. J., 1973, "Adhesive-Bonded Single-Lap Joints.[Analytical Solutions for Static Load Carrying Capacity]."
- [48] Renton, W. J., and Vinson, J. R., 1975, "The Efficient Design of Adhesive Bonded Joints," *The Journal of Adhesion*, **7**(3), pp. 175–193.
- [49] Ozel, A., Yazici, B., Akpınar, S., Aydin, M. D., and Temiz, Ş., 2014, "A Study on the Strength of Adhesively Bonded Joints with Different Adherends," *Composites Part B: Engineering*, **62**, pp. 167–174.
- [50] Khan, M. A., Hamar, C. O., Aglietti, G. S., Crocombe, A. D., and Viquerat, A. D., 2016, "Development of Rules for the Design of Composite Bonded Joints," 11th European Adhesion Conference, Glasgow, United Kingdom, pp. 331–334.

- [51] Purimpat, S., Jérôme, R., and Shahram, A., 2013, "Effect of Fiber Angle Orientation on a Laminated Composite Single-Lap Adhesive Joint," *Advanced Composite Materials*, **22**(3), pp. 139–149.
- [52] Meneghetti, G., Quaresimin, M., and Ricotta, M., 2010, "Influence of the Interface Ply Orientation on the Fatigue Behaviour of Bonded Joints in Composite Materials," *International Journal of Fatigue*, **32**(1), pp. 82–93.
- [53] Meneghetti, G., Quaresimin, M., and Ricotta, M., 2012, "Damage Mechanisms in Composite Bonded Joints under Fatigue Loading," *Composites Part B: Engineering*, **43**(2), pp. 210–220.
- [54] Schonhorn, H., Ryan, F. W., and Wang, T. T., 1971, "Effects of Symmetrical Bonding Defects on Tensile Shear Strength of Lap Joints Having Ductile Adhesives," *Journal of Applied Polymer Science*, **15**(5), pp. 1069–1078.
- [55] Wang, T. T., Ryan, F. W., and Schonhorn, H., 1972, "Effect of Bonding Defects on Shear Strength in Tension of Lap Joints Having Brittle Adhesives," *Journal of Applied Polymer Science*, **16**(8), pp. 1901–1909.
- [56] Olia, M., and Rossettos, J. N., 1996, "Analysis of Adhesively Bonded Joints with Gaps Subjected to Bending," *International Journal of Solids and Structures*, **33**(18), pp. 2681–2693.
- [57] Lang, T. P., and Mallick, P. K., 1999, "The Effect of Recessing on the Stresses in Adhesively Bonded Single-Lap Joints," *International Journal of Adhesion and Adhesives*, **19**(4), pp. 257–271.
- [58] Hart-Smith, L. J., 1973, "Adhesive-Bonded Double-Lap Joints.[Analytical Solutions for Static Load Carrying Capacity]."
- [59] Berry, N. G., and d'Almeida, J. R. M., 2002, "The Influence of Circular Centered Defects on the Performance of Carbon–Epoxy Single Lap Joints," *Polymer testing*, **21**(4), pp. 373–379.
- [60] Pereira, A. B., and de Moraes, A. B., 2003, "Strength of Adhesively Bonded Stainless Steel Joints," *International Journal of Adhesion and Adhesives*, **23**(4), pp. 315–322.
- [61] de Moura, M. F. S. F., Daniaud, R., and Magalhães, A. G., 2006, "Simulation of Mechanical Behaviour of Composite Bonded Joints Containing Strip Defects," *International Journal of Adhesion and Adhesives*, **26**(6), pp. 464–473.
- [62] You, M., Yan, Z.-M., Zheng, X.-L., Yu, H.-Z., and Li, Z., 2007, "A Numerical and Experimental Study of Gap Length on Adhesively Bonded Aluminum Double-Lap Joint," *International Journal of Adhesion and Adhesives*, **27**(8), pp. 696–702.

- [63] Engerer, J. D., and Sancaktar, E., 2011, "The Effects of Partial Bonding in Load Carrying Capacity of Single Lap Joints," *International Journal of Adhesion and Adhesives*, **31**(5), pp. 373–379.
- [64] Xu, W., and Wei, Y., 2012, "Strength and Interface Failure Mechanism of Adhesive Joints," *International Journal of Adhesion and Adhesives*, **34**, pp. 80–92.
- [65] Gurson, A. L., 1977, "Continuum Theory of Ductile Rupture by Void Nucleation and Growth: Part I—Yield Criteria and Flow Rules for Porous Ductile Media," *J. Eng. Mater. Technol*, **99**(1), pp. 2–15.
- [66] Sengab, A., and Talreja, R., 2016, "A Numerical Study of Failure of an Adhesive Joint Influenced by a Void in the Adhesive," *Composite Structures*, **156**, pp. 165–170.
- [67] Ribeiro, F. M. F., Campilho, R. D. S. G., Carbas, R. J. C., and da Silva, L. F. M., 2016, "Strength and Damage Growth in Composite Bonded Joints with Defects," *Composites Part B: Engineering*, **100**, pp. 91–100.
- [68] Jeenjitkaew, C., and Guild, F. J., 2017, "The Analysis of Kissing Bonds in Adhesive Joints," *International Journal of Adhesion and Adhesives*, **75**, pp. 101–107.
- [69] Heidarpour, F., Farahani, M., and Ghabezi, P., 2018, "Experimental Investigation of the Effects of Adhesive Defects on the Single Lap Joint Strength," *International Journal of Adhesion and Adhesives*, **80**, pp. 128–132.
- [70] Chu, Y., Sun, L., Zhan, B., Yang, X., Zhang, C., and Huang, W., 2019, "Static and Dynamic Behavior of Unbalanced Bonded Joints with Adhesion Defects in Automotive Structures," *Composite Structures*, **226**, p. 111234.
- [71] da Silva, L. F. M., das Neves, P. J. C., Adams, R. D., and Spelt, J. K., 2009, "Analytical Models of Adhesively Bonded Joints—Part I: Literature Survey," *International Journal of Adhesion and Adhesives*, **29**(3), pp. 319–330.
- [72] Volkersen, O., 1938, "Aircraft Insurance [M]," Berlin, Germany: Oldenbourg R., pp. 41–47.
- [73] Ojalvo, I. U., and Eidinoff, H. L., 1977, "Bond Thickness Effects Upon Stresses in Single Lap Adhesive Joints", 770090, SAE International, Warrendale, PA.
- [74] Allman, D. J., 1977, "A Theory for Elastic Stresses in Adhesive Bonded Lap Joints," *Q J Mechanics Appl Math*, **30**(4), pp. 415–436.
- [75] Chen, D., and Cheng, S., 1983, "An Analysis of Adhesive-Bonded Single-Lap Joints," *J. Appl. Mech*, **50**(1), pp. 109–115.

- [76] Tsai, M. Y., Oplinger, D. W., and Morton, J., 1998, “Improved Theoretical Solutions for Adhesive Lap Joints,” *International Journal of Solids and Structures*, **35**(12), pp. 1163–1185.
- [77] Sousa, C. de, Campilho, R., Marques, E. A. S., Costa, M., and Silva, L. da, 2016, “Overview of Different Strength Prediction Techniques for Single-Lap Bonded Joints:,” *Proceedings of the Institution of Mechanical Engineers, Part L: Journal of Materials: Design and Applications*.
- [78] da Silva, L. F. M., das Neves, P. J. C., Adams, R. D., Wang, A., and Speltz, J. K., 2009, “Analytical Models of Adhesively Bonded Joints—Part II: Comparative Study,” *International Journal of Adhesion and Adhesives*, **29**(3), pp. 331–341.
- [79] Spaggiari, A., Castagnetti, D., and Dragoni, E., 2012, “Experimental Tests on Tubular Bonded Butt Specimens: Effect of Relief Grooves on Tensile Strength of the Adhesive,” *The Journal of Adhesion*, **88**(4–6), pp. 499–512.
- [80] Ribeiro, F. L., Borges, L., and d’Almeida, J. R. M., 2011, “Numerical Stress Analysis of Carbon-Fibre-Reinforced Epoxy Composite Single-Lap Joints,” *International Journal of Adhesion and Adhesives*, **31**(5), pp. 331–337.
- [81] Tsouvalis, N. G., and Karatzas, V. A., 2011, “An Investigation of the Tensile Strength of a Composite-To-Metal Adhesive Joint,” *Appl Compos Mater*, **18**(2), pp. 149–163.
- [82] Ayatollahi, M. R., and Akhavan-Safar, A., 2015, “Failure Load Prediction of Single Lap Adhesive Joints Based on a New Linear Elastic Criterion,” *Theoretical and Applied Fracture Mechanics*, **80**, pp. 210–217.
- [83] Taylor, D., 2008, “The Theory of Critical Distances,” *Engineering Fracture Mechanics*, **75**(7), pp. 1696–1705.
- [84] Razavi, S. M. J., Ayatollahi, M. R., Majidi, H. R., and Berto, F., 2018, “A Strain-Based Criterion for Failure Load Prediction of Steel/CFRP Double Strap Joints,” *Composite Structures*, **206**, pp. 116–123.
- [85] Sheppard, A., Kelly, D., and Tong, L., 1998, “A Damage Zone Model for the Failure Analysis of Adhesively Bonded Joints,” *International Journal of Adhesion and Adhesives*, **18**(6), pp. 385–400.
- [86] Sancaktar, E., and Narayan, K., 1999, “Substrate Volume and Stress Gradient Concepts in Mechanical Adhesion: Analysis of Single Straight Sections,” *Journal of Adhesion Science and Technology*, **13**(2), pp. 237–271.
- [87] McClintock FA., “Ductile Fracture Instability in Shear,” *ApplMech, Trans ASME*, (1958).

- [88] Yamada, S. E., and Sun, C. T., 2016, “Analysis of Laminate Strength and Its Distribution,” *Journal of Composite Materials*.
- [89] Azzi, V. D., and Tsai, S. W., 1965, “Anisotropic Strength of Composites,” *Experimental Mechanics*, **5**(9), pp. 283–288.
- [90] Hoffman, O., 1967, “The Brittle Strength of Orthotropic Materials,” *Journal of Composite Materials*, **1**(2), pp. 200–206.
- [91] Tsai, S. W., 1968, “Strength Theories of Filamentary Structures, in Fundamental Aspects of Fiber Reinforced Plastic Composites,” *Strength Theories of Filamentary Structures Fundamental Aspects of Fiber Reinforced Plastic Composites*, pp. 3–11.
- [92] He, X., 2011, “A Review of Finite Element Analysis of Adhesively Bonded Joints,” *International Journal of Adhesion and Adhesives*, **31**(4), pp. 248–264.
- [93] da Silva, L. F. M., and Campilho, R. D. S. G., 2012, “Advances in Numerical Modelling of Adhesive Joints,” *Advances in Numerical Modeling of Adhesive Joints*, L.F.M. da Silva, and R.D.S.G. Campilho, eds., Springer, Berlin, Heidelberg, pp. 1–93.
- [94] Rice, J. R., 1968, “A Path Independent Integral and the Approximate Analysis of Strain Concentration by Notches and Cracks,” *A Path Independent Integral and the Approximate Analysis of Strain Concentration by Notches and Cracks*, pp. 379–386.
- [95] Rybicki, E. F., and Kanninen, M. F., 1977, “A Finite Element Calculation of Stress Intensity Factors by a Modified Crack Closure Integral,” *Engineering Fracture Mechanics*, **9**(4), pp. 931–938.
- [96] Goh, J. Y., Georgiadis, S., Orifici, A. C., and Wang, C. H., 2013, “Effects of Bondline Flaws on the Damage Tolerance of Composite Scarf Joints,” *Composites Part A: Applied Science and Manufacturing*, **55**, pp. 110–119.
- [97] Cameselle-Molares, A., Sarfaraz, R., Shahverdi, M., Keller, T., and Vassilopoulos, A. P., 2017, “Fracture Mechanics-Based Progressive Damage Modelling of Adhesively Bonded Fibre-Reinforced Polymer Joints,” *Fatigue and Fracture of Engineering Materials and Structures*, **40**(12), pp. 2183–2193.
- [98] Leguillon, D., 2002, “Strength or Toughness? A Criterion for Crack Onset at a Notch,” *European Journal of Mechanics, A/Solids*, **21**(1), pp. 61–72.

- [99] Doitrand, A., and Leguillon, D., 2018, "Comparison between 2D and 3D Applications of the Coupled Criterion to Crack Initiation Prediction in Scarf Adhesive Joints," *International Journal of Adhesion and Adhesives*, **85**, pp. 69–76.
- [100] García, J. A., Chiminelli, A., García, B., Lizaranzu, M., and Jiménez, M. A., 2011, "Characterization and Material Model Definition of Toughened Adhesives for Finite Element Analysis," *International Journal of Adhesion and Adhesives*, **31**(4), pp. 182–192.
- [101] Chousal, J. A. G., and De Moura, M. F. S. F., 2013, "Mixed-Mode I+II Continuum Damage Model Applied to Fracture Characterization of Bonded Joints," *International Journal of Adhesion and Adhesives*, **41**, pp. 92–97.
- [102] Barenblatt, G. I., 1959, "The Formation of Equilibrium Cracks during Brittle Fracture. General Ideas and Hypotheses. Axially-Symmetric Cracks," *Journal of Applied Mathematics and Mechanics*, **23**(3), pp. 622–636.
- [103] Dugdale, D. S., 1960, "Yielding of Steel Sheets Containing Slits," *Journal of the Mechanics and Physics of Solids*, **8**(2), pp. 100–104.
- [104] Campilho, R. D. S. G., Banea, M. D., Pinto, A. M. G., da Silva, L. F. M., and de Jesus, A. M. P., 2011, "Strength Prediction of Single- and Double-Lap Joints by Standard and Extended Finite Element Modelling," *International Journal of Adhesion and Adhesives*, **31**(5), pp. 363–372.
- [105] Dassault Systemes, "ABAQUS Theory Manual (v6.6)".
- [106] Henkel Adhesives, "LOCTITE EA 9309NA AERO.
- [107] D30 Committee, "Test Method for Tensile Properties of Polymer Matrix Composite Materials", ASTM International.
- [108] Callister, D. C., 2018, Rethwisch, D. G., "Materials Science and Engineering: An Introduction, 10th Edition", Wiley Publications.
- [109] D20 Committee, "Test Method for Tensile Properties of Plastics", ASTM International.
- [110] Davies, P., Sohier, L., Cognard, J.-Y., Bourmaud, A., Choqueuse, D., Rinnert, E., and Créac'hacdec, R., 2009, "Influence of Adhesive Bond Line Thickness on Joint Strength," *International Journal of Adhesion and Adhesives*, **29**(7), pp. 724–736.
- [111] Skorupa, A., and Skorupa, M., 2012, "Riveted Lap Joints in Aircraft Fuselage: Design, Analysis and Properties", Springer Netherlands.

- [112] Liu, Y., Lemanski, S., and Zhang, X., 2018, "Parametric Study of Size, Curvature and Free Edge Effects on the Predicted Strength of Bonded Composite Joints," *Composite Structures*, **202**, pp. 364–373.
- [113] Shang, X., Marques, E. A. S., Machado, J. J. M., Carbas, R. J. C., Jiang, D., and da Silva, L. F. M., 2019, "Review on Techniques to Improve the Strength of Adhesive Joints with Composite Adherends," *Composites Part B: Engineering*, **177**, p. 107363.
- [114] Silva, L. F. M. da, Öchsner, A., and Adams, R. D., eds., 2018, "Handbook of Adhesion Technology", Springer International Publishing.
- [115] Pisharody, A. P., Blandford, B., Smith, D. E., and Jack, D. A., 2019, "An Experimental Investigation on the Effect of Adhesive Distribution on Strength of Bonded Joints," *Applied Adhesion Science*, **7**(1), p. 6.
- [116] Fiber Glast, "Epoxy Paste Bonding Adhesive,".
- [117] Kim, M.-H., and Hong, H.-S., 2018, "An Adaptation of Mixed-Mode I + II Continuum Damage Model for Prediction of Fracture Characteristics in Adhesively Bonded Joint," *International Journal of Adhesion and Adhesives*, **80**, pp. 87–103.
- [118] Takeda, N., and Minakuchi, S., 2017, "Optical Fiber Sensor Based Life Cycling Monitoring and Quality Assessment of Carbon Fiber Reinforced Polymer Matrix Composite Structures," 2017 25th Optical Fiber Sensors Conference (OFS), pp. 1–4.
- [119] Chadegani, A., and Batra, R. C., 2011, "Analysis of Adhesive-Bonded Single-Lap Joint with an Interfacial Crack and a Void," *International Journal of Adhesion and Adhesives*, **31**(6), pp. 455–465.
- [120] Feraren, P., and Jensen, H. M., 2004, "Cohesive Zone Modelling of Interface Fracture near Flaws in Adhesive Joints," *Engineering Fracture Mechanics*, **71**(15), pp. 2125–2142.
- [121] Xu, W., and Wei, Y., 2012, "Strength Analysis of Metallic Bonded Joints Containing Defects," *Computational Materials Science*, **53**(1), pp. 444–450.
- [122] You, M., Yan, Z.-M., Zheng, X.-L., Yu, H.-Z., and Li, Z., 2007, "A Numerical and Experimental Study of Gap Length on Adhesively Bonded Aluminum Double-Lap Joint," *International Journal of Adhesion and Adhesives*, **27**(8), pp. 696–702.

- [123] Kaye, R., and Heller, M., 2005, "Through-Thickness Shape Optimisation of Typical Double Lap-Joints Including Effects of Differential Thermal Contraction during Curing," *International Journal of Adhesion and Adhesives*, **25**(3), pp. 227–238.
- [124] Roh, H. S., 2011, "Repairs of Composite Structures."
- [125] Lee, H. K., Pyo, S. H., and Kim, B. R., 2009, "On Joint Strengths, Peel Stresses and Failure Modes in Adhesively Bonded Double-Strap and Supported Single-Lap GFRP Joints," *Composite Structures*, **87**(1), pp. 44–54.
- [126] Ghoddous, B., and Ghoddous, B., 2017, "Theoretical Analysis of Stress Distribution in Bonded Single Strap and Stiffened Joints," *Latin American Journal of Solids and Structures*, **14**(2), pp. 256–276.
- [127] Zou, G. P., Shahin, K., and Taheri, F., 2004, "An Analytical Solution for the Analysis of Symmetric Composite Adhesively Bonded Joints," *Composite Structures*, **65**(3), pp. 499–510.
- [128] Hart-Smith, L., 1985, "Designing to Minimize Peel Stresses in Adhesive-Bonded Joints," *Delamination and Debonding of Materials*", W. Johnson, ed., ASTM International.